Measurement of Irradiated Pyroprocessing Samples via Laser Induced Breakdown Spectroscopy

Fuel Cycle Research and Development

Supathorn Phongikaroon
Virginia Commonwealth University

Dan Vega, Federal POC
Mike Miller, Technical POC

NEUP | Nuclear Energy University Programs

U.S. Department of Energy

NEUP Final Report

(Project 12-3358) Measurement of Irradiated Pyroprocessing Samples via
Laser Induced Breakdown Spectroscopy

Ammon Williams, Keith Bryce, and Supathorn Phongikaroon
Department of Mechanical and Nuclear Engineering
Virginia Commonwealth University, Richmond, VA 23284

October 31, 2016

Abbreviations

CMD	Count Median Diameter
ER	Electrorefiner
GSD	Geometric Standard Deviation
GUI	Graphic User Interface
HEPA	High-Efficiency Particulate Air (filter)
ICCD	Intensified Charge-Coupled Device
ICP-MS	Inductively Coupled Plasma Mass Spectrometry
INL	Idaho National Laboratory
LIBS	Laser Induced Breakdown Spectroscopy
LOD	Limit Of Detection
LV	Latent Variables
NIST	National Institute of Standards & Technology
NPT	National Pipe Taper
Nd:YAG	Neodymium Yttrium Aluminum Garnet (type of laser)
Nu	Nusselt number
PLS	Partial Least Squares
Pr	Prandlt number
PUREX	Plutonium Uranium Redox EXtraction
RE	Reynolds number
RMSECV	Root Mean Squared Error of Cross Validation
RMSEP	Root Mean Square Error of Prediction
SBR	Signal-to-Background Ratio
SMPS	Scanning Mobility Particle Sizer
UNF	Used Nuclear Fuel
%RSD	Relative Standard Deviation (reported in %)

Executive Summary

The primary objective of this research is to develop an applied technology and provide an assessment to remotely measure and analyze the real time or near real time concentrations of used nuclear fuel (UNF) dissolute in electrorefiners. Here, Laser-Induced Breakdown Spectroscopy (LIBS), in UNF pyroprocessing facilities will be investigated. LIBS is an elemental analysis method, which is based on the emission from plasma generated by focusing a laser beam into the medium. This technology has been reported to be applicable in the media of solids, liquids (includes molten metals), and gases for detecting elements of special nuclear materials. The advantages of applying the technology for pyroprocessing facilities are: (i) Rapid real-time elemental analysis—one measurement/laser pulse, or average spectra from multiple laser pulses for greater accuracy in < 2 minutes; (ii) Direct detection of elements and impurities in the system with low detection limits—element specific, ranging from 2-1000 ppm for most elements; and (iii) Near non-destructive elemental analysis method (about 1 μg material). One important challenge to overcome is achieving high-resolution spectral analysis to quantitatively analyze all important fission products and actinides. Another important challenge is related to accessibility of molten salt, which is heated in a heavily insulated, remotely operated furnace in a high radiation environment with an argon atmosphere. The project aims to address these challenges and approaches with four following phases with their highlighted outcomes:

1. Static surface technique providing detailed insights and experience to LIBS in liquid environments—Calibration curves were generated for the static liquid case and R^2

1

values ranged from 0.98 – 0.99 and the best LOD of 403 ppm Ce was obtained using the 418.660 nm peak. This study demonstrated the LIBS capability to measure Ce in a liquid using the static surface approach with minimum loss of materials. However, this technique would be extremely difficult to implement for a molten salt because it is anticipated that the splashed salt, if it formed a film, would also quickly etch the surface of the glass/quartz and thus reduce the signal over time.

2. An aerosol-LIBS system and experimental runs at room temperature to measure concentrations of Ce and Gd using an aqueous media—this main design included a Collison nebulizer to generate the aerosol. Both univariate and multivariate methods using PLS were done to generate calibration models. Overall, the PLS models are more robust and yield better results showing RMSECV of 406 ppm for the Ce and 417 pm for Gd. Blind samples were being tested and illustrated consistent prediction among both approaches.

3. The aerosol-LIBS system operated at high temperature to measure Ce in molten LiCl-KCl salt within a glovebox environment—the final design resulted in a stable aerosol generation and plasma formation. The Ce concentration effect was being studied. Results showed a strong linear agreement overall between the univariate and multivariate calibration methods at high operating temperature. The Ce 418.660 nm line had the greatest sensitivity to concentration changes and had the lowest LOD overall of 504 ppm. The PLS model was more robust with a RMSECV of 622 ppm.

4. Samples containing UCl_3-LiCl-KCl were analyzed using the aerosol-LIBS system–the UCl_3 concentrations ranged from 0.3 wt% to 5 wt% and the spectral response in this range was linear. The univariate calibration curves had R^2 ranging between 0.9612 to 0.9981. The best univariate calibration curve was generated from the U II 385.96 nm line and had a LOD of 981 ppm. A PLS modeling was also done and resulted in a RMSECV of 926 ppm for uranium in molten salt detection. The successful completion

of this study demonstrates the feasibility of using an aerosol-LIBS analytical technique to measure pyroprocessing salt.

In addition to these approaches, we also conducted the solid-LIBS experiments to initially testing the system and provide an alternative solution to the current problem discovered in the mock-up facility at the national laboratory. This research study resulted in supporting 1 Ph.D. and 1 M.S. students with 2 publications in the peer-reviewed journals, 2 publications in the conference proceedings, and 9 presentations at both domestic and international conferences (e.g., ANS, ICONE, GLOBAL, and IPRC).

Contents

1

Introduction

Electrochemical separation (also known as 'pyroprocessing technology' and 'electrometallurgical process') of used nuclear fuel (UNF) is a dry reprocessing alternative to traditional aqueous methods such as the PUREX process[1]. In pyroprocessing technology, UNF within a hot cell environment is chopped and loaded into an anode basket. The anode basket is then positioned within an electrorefiner (ER) where the uranium is electrochemically dissolved from the fuel and transported through a molten salt electrolyte and deposited on a cathode. Following electrorefining, the anode with the cladding hulls (metallic waste) and the cathode with the pure uranium metal are removed for processing. As part of the process chemistry during electrorefining, fission products, rare earth elements, and transuranics (including plutonium) accumulate in the molten salt. This buildup of materials can present operational challenges as well as non-proliferation and safeguards concerns[2]. As a result, it is important to have the capacity to monitor the electrolyte composition, particularly the concentrations of U and Pu over time. However, analytical methods to measure the salt have been limited due to a high temperature operating condition (typically, 723 K to 773 K) and high radiation environment that exists within the hot cell environment. As a result, liquid salt samples are usually drawn from the ER for later measurement via inductively coupled plasma mass spectrometry (ICP-MS)[3]. This process of extraction, material transfer, and

later sample preparation is cumbersome and can impose significant delay between sampling and compositional results.

Laser-induced breakdown spectroscopy (LIBS) has been proposed as an alternative analytical approach to ICP-MS since it can be done in-situ, with little to no sample preparation, and compositional information of the sample can be obtained in near real-time[4]. In addition, LIBS can be used to analyze samples in a variety of phases including solids[5], liquids[6–8], gases[9], and aerosols[10, 11]. In LIBS, a pulsed laser is focused onto the surface of a material to vaporize and ionize the sample in the creation of a plasma plume. As the plasma cools, the ionized atoms return to ground states with the emission of characteristic light which can be collected via optics. From this light, a spectrum of the emitted wavelengths can be generated via a spectrometer and detector. From the spectrum, qualitative and quantitative information about the sample composition can be obtained.

All of the LIBS studies[12–15] conducted in a molten LiCl-KCl salt to date have used a static surface approach. Here, the laser light is focused downwards onto the top surface of a static liquid. Whereas this approach is feasible and can yield compositional information of the salt, many potential issues exist. For example, in the formation of the plasma on a liquid sample, a shock wave is created which tends to splash the sample—potentially causing a quenching of the plasma and/or lens damage and degradation. In addition, liquid quenching of the plasma can further reduce signal and the plasma lifetime[11]. Other potential issues are the film formation/dross layer and bubble formation on the top surface of the salt which can lead to homogeneity concerns. These aspects provide a motivation for the development of a new LIBS sampling configuration for molten salt analysis.

The main objective of this work is to apply the LIBS technique to a high temperature salt in order to measure Ce as a surrogate for uranium and actual depleted in molten LiCl-KCl salt. I phase I(a)an electromagnetic pump was explored to pump molten salt for a continuous LIBS sampling approach, the results of this phase are shown in Appendix A. In phase I(b) of this work a static surface approach was explored to provide greater insights and

8

Table 1.1: Time line showing the effort period for each phase of the research project.

Phase	FY 2013	FY 2014	FY 2015	FY 2016
I(a)	✓	✓		
I(b)	✓	✓		
II		✓	✓	
III			✓	✓
IV				✓

experience to LIBS in liquids. In phase II, an aerosol-LIBS system was developed (Patent pending) and tested at room temperature to measure concentrations of Ce and Gd using an aqueous media. Phase III focuses on the aerosol-LIBS system being transitioned to high temperature operation and used to measure Ce in molten LiCl-KCl salt within a glovebox environment. In the final phase of this work (Phase IV), U will be measured in the LiCl-KCl salt via the established aerosol-LIBS system. In addittion to the above research phases, an additional LIBS study was conducted on solid salt samples to develop a statistical database. The results of this study is shown in Appendix B. Table 1.1 shows the time line for the competition of the different phases.

2

Literature Review

2.1 LIBS in Molten LiCl-KCl Salt

Andrew Effenberger[12] was among the first to demonstrate LIBS analysis in a molten LiCl-KCl salt by using a static surface approach. Here, $CrCl_3$, $CoCl_2$, and $MnCl_2$ were studied in the molten salt matrix at 773 K in the concentration range between 0.3 wt% to 2.5 wt%. This work showed that LIBS analysis in the molten salt was feasible and that limits of detection (LODs) down to 0.3 wt% could be achieved. Hanson and co-workers[13, 16] performed an in depth LIBS study of $CeCl_3$ and $MnCl_2$ in LiCl-KCl salts at temperatures ranging from 523 K (solid) to 773 K (liquid) using the static surface configuration. Here, the concentration range studies was between 0.1 wt% Ce to 1 wt% Ce. Results of the study showed that, in general, the molten samples had less self-absorption and lower relative standard deviations than the solid samples.

Weisberg et al.[14] also studied a molten LiCl-KCl salt with additives of $EuCl_3$, and $PrCl_3$ using the static surface approach. The concentration ranges studied were between 0 and 1 wt% for Eu and 0.1 wt% to 1 wt% Pr. In this work, a thin film was observed on the top surface of the salts containing Eu and Pr but not on blank (LiCl-KCl) samples. The composition of the film with respect to the bulk was not reported; however, the presence

of the film influenced the shot-to-shot results since a plasma formed on the liquid surface differed from those formed on the solid film surface. To address this issue, the authors used conditional analysis to eliminate large shot-to-shot fluctuations within the collected spectra, thus effectively grouping shots that fell only on the liquid surface. In addition to the conditional analysis, a partial least squares (PLS) method was used to obtain qualitative and quantitative results. Specifically, the absolute root mean square error of prediction (RMSEP) was reported to be 0.13% within the range studied for both Eu and Pr. More recently, Smith and co-workers[15] from the Argonne National Laboratory have designed a probe that can be used to remotely analyze the static surface of the molten salt within a glovebox environment. Feasibility studies using the probe have been done to measure U, Pu, and Np in the LiCl-KCl salt.

2.2   LIBS in Actinides

Wachters and Cremers[6] were among the first (1987) to use LIBS to study U. In this work, they studied U in a nitric acid solution that was contained in a horizontal vial to prevent lens damage from splashing. Results of their study showed that LIBS was capable of performing quantitative analysis on a heavy element like U in solution. Sarkar and co-workers[17, 18] also studied U in a solution form. However, rather than performing the LIBS analysis directly in the liquid, the authors dried the samples onto a substrate (filter paper[17] or graphite surface[18]) prior to measuring the sample. Sirven et al.[19] used LIBS to determine the graphical origin of yellow cake. Here the yellow cake samples were mixed with grease to form a paste in which the LIBS analysis was done. Results showed that the origins of the yellow cake samples could be determined in all 11 cases studied. Chinni and co-workers[5] were able to measure U in soils using a standoff approach. Results showed that uranium could be detected in trace quantities via standoff LIBS methods. Judge et al.[20] demonstrated the measurement of U and Th in powder form as well as in uranium ore. Authors were able

to identify these elements despite the large matrix effects due to working in an ore sample. Sarkar et al.[21] performed a LIBS study using mixed U and Th oxide fuel pellets. Here, the authors performed an optimization study to determine key LIBS parameters for U and Th in solid oxide fuels. Zheng et al.[22], measured PuO_2 residues using LIBS. Barefield and co-workers[23] studied several mixed oxide fuels including UO_2, PuO_2, AmO_2, and NpO_2. Here, the authors used a very high resolution spectrometer and were able to identify elemental peaks with very little interference. Like Barefield et al., a number of other authors used a high resolution spectrometer to measure the isotope ratios of U and Pu. Smith et al.[24] was able to resolve the isotopic shift between Pu-239 and Pu-240. Doucet and co-workers[25] were able to determine the isotope ratios of U-235 and U-238 along with the ratios between hydrogen and deuterium via LIBS analysis.

2.3   LIBS in Liquids and Aerosols

It should be mentioned that there are several different approaches or techniques to LIBS in liquid samples: they are (1) static surface analysis as described above, (2) subsurface bulk analysis, (3) jet analysis, and (4) aerosol stream analysis. The static surface analysis approach is conceptually the easiest of the different methods; however, with this approach, splashing becomes a significant challenge. Wachter and Cremers[6] used a horizontal glass vial to mitigate some of the effects of splashing. Here, the splashed material would hit the upper curved portion of the vial and roll back down into the bulk of the liquid. St-Onge and co-workers[7] conducted a static surface analysis to measure sodium chloride. The effects of splashing were somewhat mitigated by using a long focal length (400 mm). However, the authors noted that after multiple laser shots the liquid level within the test crucible declined. In addition, the formation of bubbles on the static surface influenced the repeatability of the results. Barreda et al.[8] also performed work using a static surface and noted that the shot-to-shot frequency is low due to the time required for the liquid surface to calm between

shots.

In a subsurface bulk analysis technique, the laser is focused through the liquid to create plasma below the surface of the liquid. Work has been done using this approach to measure compositions of liquid samples using single[26, 27] and double[26, 28] pulse systems. In the double pulse case, the first laser pulse creates a bubble and heats the sample and the second pulse creates the plasma within the bubble which greatly increases signal and repeatability. One of the key challenges of the bulk analysis technique is that a fairly transparent liquid is required in order to transport the laser to the desired plasma location and to collect the incident light from the formed plasma.

Another liquid-LIBS configuration incorporates a liquid jet stream. In this scenario, the laser light is focused onto the surface of the liquid jet to create the plasma. Cheung and Yeung[28] were among the first to explore this method and found that low LOD could be achieved. Kumar et al.[29] and Feng et al.[30] studied the effect of the jet thickness and overall optimization of the system and found that the processes is highly repeatable. Yaroshchyk and co-workers[31] compared a liquid jet system to a static surface system and found that the LOD for the jet case were in general 4 times lower. This observation in part, is due to a continuous flow—thus reducing the splashing effect. In addition, the shot-to-shot frequency is not limited by surface perturbations. The disadvantages to this system are material clogging in the jet and the large throughput to maintain the jet.

One potential method is to use a LIBS-aerosol measurement technique[10]. In this approach, the laser is focused within an aerosol gas stream to create the LIBS plasma. This technique is often used for online monitoring of environmental air samples for toxic metals[32–36]. In these cases, the aerosol concentration within the gas stream is low, leading to high shot-to-shot variation as a result of low probability of particle interaction with the plasma. Diwakar and co-workers[35] have shown that the plasma-particle interaction can be defined by Poisson modeling statistics. As a result, this supports the conditional analysis technique for excluding shots below a certain threshold.

In many cases, the aerosol is generated from a liquid sample via an aerosol generator. Here, the aerosol concentration within the gas stream can be sufficiently high as to reduce the probability of null shots; however, significant shot-to-shot variation is still observed. Huang and co-workers[36, 37] observed that the shot-to-shot variation could be large due to fluctuations in the number of aerosol particles consumed per plasma volume. Poulain and Alexander[38] as well as Schechter[39] observed the large shot-to-shot variation in liquid aerosols and concluded that the variation can be attributed to (1) the number of particles within the plasma volume, (2) the location and size of the particles within the plasma, and (3) liquid droplet interference with the incoming laser light. As a result, Schechter[39], developed a basic algorithm to perform conditional analysis on the collected spectra to reduce variation prior to ensemble averaging. Using the above conditional analysis scheme, Schechter was able to significantly improve the sensitivity of the system.

Despite challenges with particle-plasma interactions and interference, LIBS analysis from liquid aerosols has been shown to perform well. Kumar et al.[40] used a Meinhard nebulizer to generate an aerosol and found that the aerosol approach yielded better results than a liquid jet method. They concluded that this in part was due to better utilization of the laser energy to ionize the sample in the aerosol stream, whereas much of the laser energy was used to first vaporize the sample in the liquid jet case. Martin and Cheng[41] measured chromium in water and reported LOD for Na down to 400 ng/dscm. Cahoon and Almirall[11] measured the concentrations of Sr, Ba, Mg, and Ca in water using both an aerosol and micro-droplet approach. Here, both methods resulted in ultralow detection limits with %RSD on the order of 1%. Alvarez-Trujillo and co-workers[42] performed stand-off LIBS in a liquid aerosol and determined that they could detect Na down to 55 ppm in water at 10 meters away.

2.4 Summary of Literature Findings

LIBS has been conducted in molten LiCl-KCl salts at high temperature. However, all of these molten salt LIBS studies were conducted using a static surface configuration which appears to be the least favorable from an analysis standpoint. However, the static surface approach is the easiest to implement and therefore will be tested in phase I of this project in order to gain understanding, insight, and experience. Of the other potential liquid analysis techniques, the bulk analysis technique is not a favorable option due to the transparency requirement. Between the jet and aerosol configurations, the aerosol approach appears to be capable of greater signal intensity and sensitivity due to increased laser energy utilization. As a result, the liquid jet configuration will not be considered further in this work. In measuring molten salts in the ER, the aerosol sampling approach offers several additional advantages over the current static approach. Using an aerosol method, the liquid sample can be drawn continuously from the bulk of the salt, thus reducing variation due to non-homogeneity. In addition, since splashing, bubble formation, and surface perturbations are not an issue with the aerosol approach, the frequency of the sampling system is less limited. Lastly, the laser energy is better utilized to ionize the sample. Due to these advantages, it has been proposed to use this approach to measure molten salt. To date, the high temperature aerosol generation of molten salts has never been reported.

3

Static Surface LIBS Testing (Phase I(b))

In the initial phase of the project, several preliminary experiments were done using a static surface configuration in order to gain valuable experience with LIBS in liquids. The static surface approach was used due to its simplicity. In order to mitigate the splashing issue and to eliminate material loss, a horizontal vial approach (similar to the setup used by Wachters and Cremers[6]) was used to study the static surface technique with $CeCl_3$ as a surrogate material.

3.1   Materials and Methods

Samples used in the static surface tests were made using LiCl (99.99%), KCl (99.999%), and $CeCl_3$ (99.99%) mixed into nano-pure water. The LiCl and KCl salts were purchased from Rare Earth Products and the $CeCl_3$ was purchased from Alfa Aesar. The LiCl and KCl salts were mixed into the nano-pure water at the eutectic ratio (44 wt% LiCl, 56 wt% KCl) to form a solution of 20% LiCl-KCl salt by mass. From this base solution, nine standards were prepared with concentrations of Ce ranging from 100 parts per million (ppm) to 10,000 ppm (see Table 3.1). Each standard contained 9 mL of solution and was placed in a glass vial

Table 3.1: Calibration standards showing different Ce concentrations with respect to wt% of CeCl$_3$.

Standard number	Ce concentration (ppm)	wt% CeCl$_3$
1	10,000	1.7587
2	8,000	1.4072
3	6,000	1.0554
4	4,000	0.7035
5	3,000	0.5270
6	1,000	0.1757
7	500	0.0879
8	200	0.0352
9	100	0.0176

that was 25 mm in diameter and oriented on its side so that the depth of solution was 12 mm.

A CFR200 Nd:YAG laser from Big Sky Laser, Inc. was used as the laser source in this study. In this setup, the laser (frequency doubled to 532 nm) was fired downward, through a 2" pierced elliptical mirror (polished aluminum) and focused onto the surface of the solution contained in the horizontal vial via a 2" quartz lens with a focal length of 60 mm (see Figure 3.1 and Figure 3.2). Light from the formed plasma was then collected and collimated via the 2" quartz focusing lens. The collimated light was then reflected 90° using the elliptical mirror and through an additional 2" quartz lens with a 100 mm focal length. The light, through this lens, was focused onto a fiber optic cable with a 50 μm core from Andor Technologies. The optical signal was then delivered to an iStar ICCD camera and Mechelle 5000 spectrometer ($\lambda/\Delta\lambda$ of 4,000) from Andor Technologies, and the spectra were collected using the Andor Solis software.

In these experiments, a delay time of 1.5 μs and a gate width of 2 μs were used. The laser energy was approximately 100 mJ. For each sample, ten repetitions were done, each containing 200 laser shots. As a result, 2,000 shots were collected per sample. In this case, the Andor Solis software was set to accumulate the 200 shots yielding a single spectrum per repetition. For the bulk of the experiments, a shot to shot frequency of 2 Hz was used; however, for several of the experiments, a 1 Hz cycle time was used. The ICCD gain was set
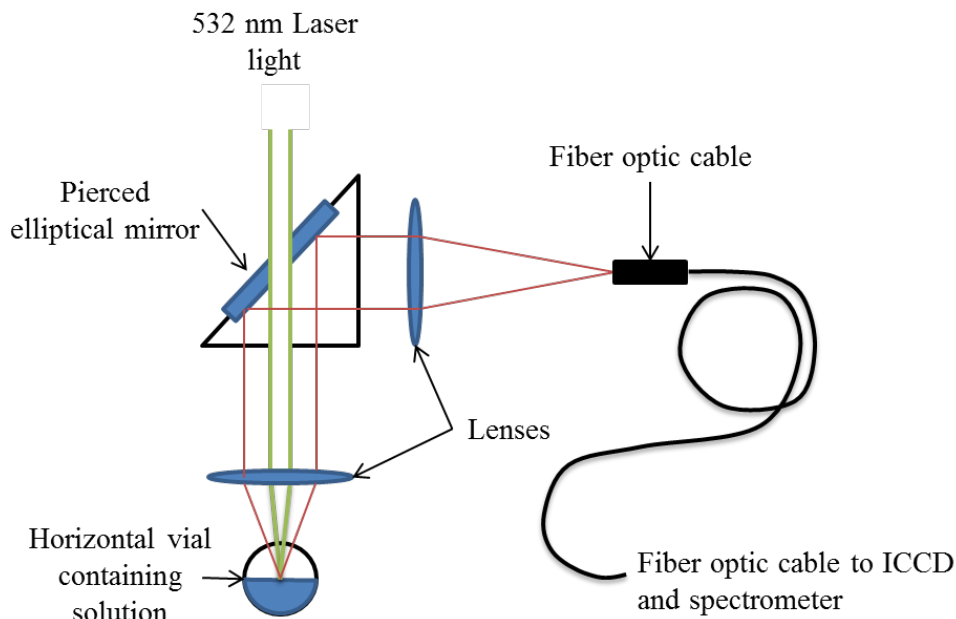
17

Figure 3.1: Representation of the static liquid experimental setup.

at 3000 and the temperature was set at -25°C.

3.2 Results and Discussion

The feasibility of using the horizontal vial method was explored as a means to reduce the splashing effect of the material. Here, tests were done using several different vials of the same material (soda-lime-silica glass). The vials containing the sample were stored upright until just prior to LIBS testing. When some of the vials were oriented horizontally, a thin liquid film remained in the region in previous contact with the fluid for a few seconds. In these vials, splashing from the plasma was easily reabsorbed into the film layer. However, for the vials where the film was not maintained, splashing from the plasma formed a droplet on the surface of the glass which distorted and/or obstructed the laser light after only a few shots. A photo showing a typical vial with the different splash regions is illustrated in Figure 3.3. It is clear that the film is required in order to provide the ability to take multiple shots of the sample without some other mechanism for removing the droplet formation. Therefore,
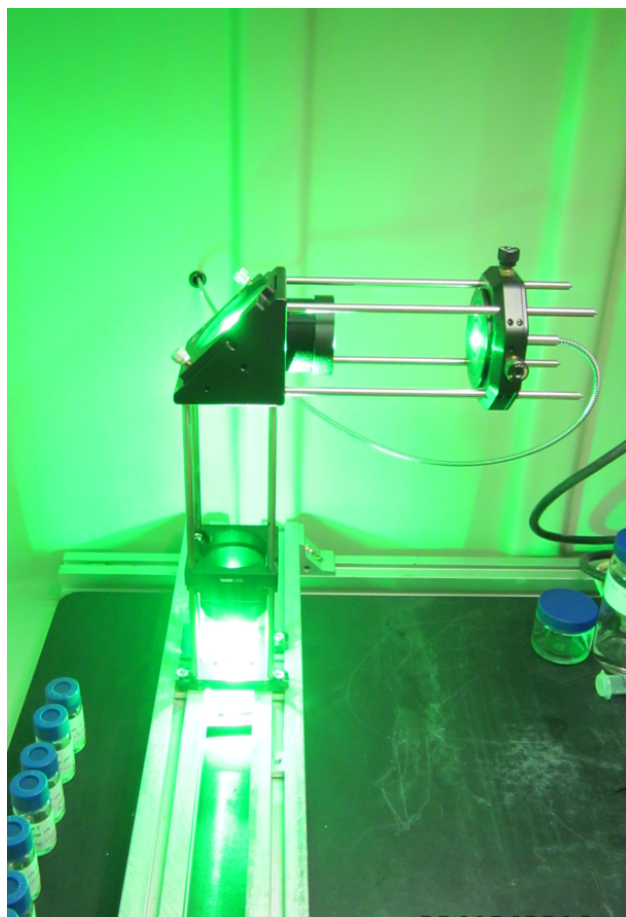
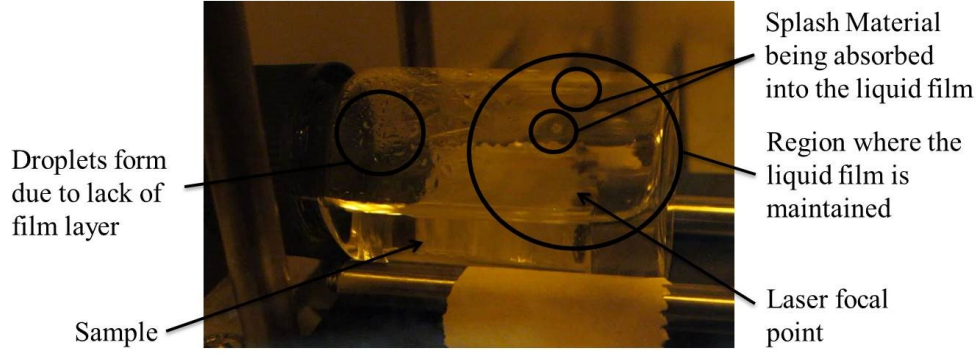Figure 3.2: Experimental setup with the Nd:YAG laser light at 532 nm.

Figure 3.3: Photo of a test vial containing the various splashing and film regions.

only vials that demonstrated the film layer were used in the analysis.

A typical spectrum for static surface analysis is shown in Figure 3.4. The major elements (Li, K, hydrogen (H), and oxygen (O)) can be clearly seen. There are numerous Ce lines that fall between 350 nm and 500 nm which could be used in the LIBS analysis. Peaks were selected that had low interferences and a signal-to-background ratio (SBR) equal to or greater than 2.5. Five peaks were identified[43] that met the criteria; they are the 413.765 nm, 418.660 nm, 428.999 nm, 446.021 nm, and the 457.228 nm lines. These lines are shown in Figure 3.5. The 413.765 nm and 418.660 nm lines are the strongest Ce lines observed in the spectrum. Figure 3.6 shows the intensity variation in the region of interest for the 9 samples used. As the Ce concentration decreases, the intensity of the Ce peaks decreases as well.

The relative standard deviation (%RSD) was calculated between the ten repetitions taken for each sampling concentration. The shot frequency and the number of shots taken per acquisition were varied for the 4,000 ppm Ce standard. The average %RSD between 400 nm and 460 nm was compared for each to identify effects of the parameter. The average %RSD for experiments operating at 2 Hz and 200 shots was 18.5% with lows and highs ranging from 15% to 28%, respectively (see Figure 3.7). Under these conditions, fluctuations in the %RSD's typically ranged between ±5%,; however, spikes to higher levels were occasionally observed. At 1 Hz and 200 shots the average %RSD was calculated to be 14.6% with lows
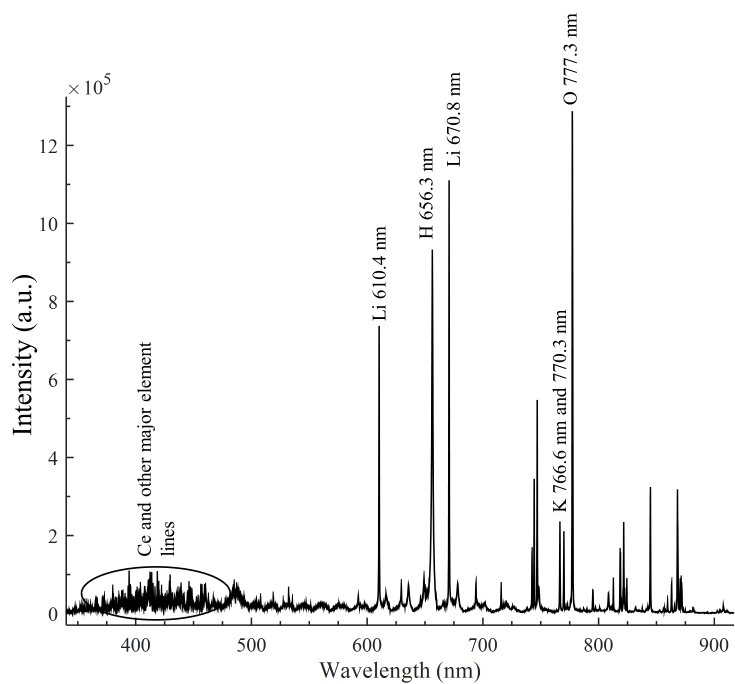
Figure 3.4: A typical spectrum for the static surface experiments. The spectrum was generated from the 10,000 ppm Ce standard.
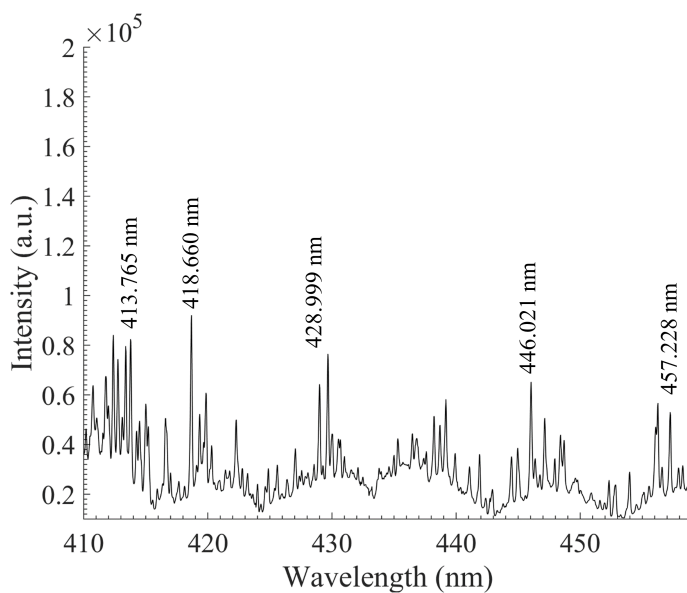

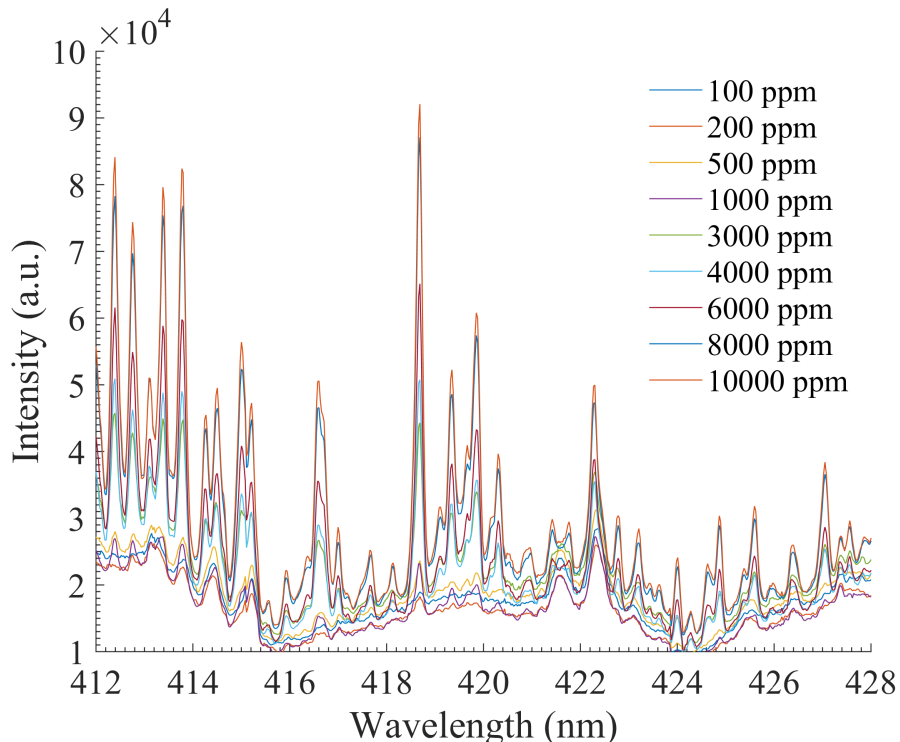Figure 3.5: Region of interest showing the diversity of Ce peaks.

21

Figure 3.6: Showing the variation of the spectral intensity as a function of the concentration.

and highs ranging from 12% to 18%, respectively. The %RSD for the 2 Hz case at 500 shots was calculated to be 14.4% with lows and highs ranging from 11% to 18%, respectively. From these experiments, the slower (1 Hz) shot-to-shot frequency was better—as would be expected due to the surface perturbations created by the laser shockwave. In this system, there would be a lower limit on the shot-to-shot frequency in order to maintain the liquid film on the top surface of the vial; however, the lower limits were not explored in this study. The larger number of laser shots also yielded a better %RSD as expected. It is anticipated that combining the lower shot-to-shot frequency with more shots would further improve the repeatability of the LIBS analysis. Due to application constraints not discussed here, the acquisition parameters of 2 Hz frequency and 200 shots were used in the remainder of the static study.

Spectra were collected for the nine standards as previously outlined in Table 3.1. Once the spectra had been generated, the area under the peak of interest was calculated using
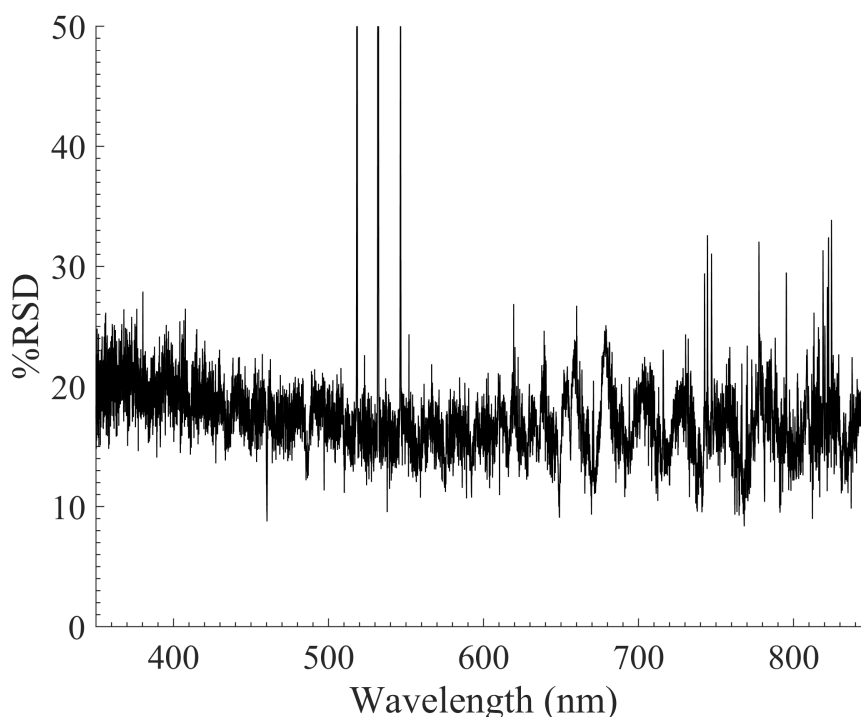
Figure 3.7: The %RSD between the 10 spectra for the 4000 ppm sample at 2 Hz and with 200 shots accumulated.

a program written in the commercial software MATLAB. Here, a graphical user interface (GUI) was used to select the peak range and the area under the curve was calculated using a numerical integration technique. This process was done for each repetition of the sample. An average of the peak areas for the line of interest was then calculated for each standard, yielding a single point on the calibration curve. Figure 3.8 shows the calibration curves for the different Ce peaks selected. For all of the selected peaks, the regression lines fit the data well with R^2 values ranging from 0.98 to 0.99. The peak areas for the 10,000 ppm standard were lower than the rest of the linear trend. This was not specific to the Ce lines only; in general, the spectra generated from this standard are slightly lower. A normalization of the curves with a Li peak does create a more linear trend but also introduces larger errors due to the large standard deviation of the Li peak. The linear regression equation for the calibration curves is of the form:

$$y = b_1 x + b_0 \tag{3.1}$$

23

Table 3.2: Linear fit coefficients, goodness of fit, and the limits of detection (LOD) for the different calibration curves

Line (nm)	R^2	b_1	b_0	LOD (ppm)
413.765	0.991	0.7848	795.80	967
418.660	0.985	1.2377	407.22	403
428.999	0.986	0.6373	176.53	608
446.021	0.991	0.7404	554.58	816
457.228	0.991	0.5952	124.57	442

where b_1 is the slope of the line and b_0 is the y-intercept. The calibration curves were fit using MATLAB. The coefficients to the linear fit and the R^2 for all of the calibration curves are shown in Table 3.2.

From the regression lines and standard deviation of the lowest point on the calibration curve, the LOD can be calculated using the following formula:

$$LOD = \frac{3\sigma}{b_1} \tag{3.2}$$

where σ is the standard deviation. The LOD for the different lines were calculated and the results are shown in Table 3.2. All of the detection limits are larger than the two to three lowest standards; this is a result of relatively large standard deviations in the peak area at lower Ce concentrations. In other words, with the current setup (laser, spectrometer, configuration, and acquisition parameters), the variations in the spectrum are larger than the peaks themselves. The 418.660 nm peak provided the best LOD of 403 ppm and the 413.765 nm peak provided the worst LOD at 967 ppm. Based on the calibration curves and the LOD, the 418.660 nm line is recommended for use in this system.
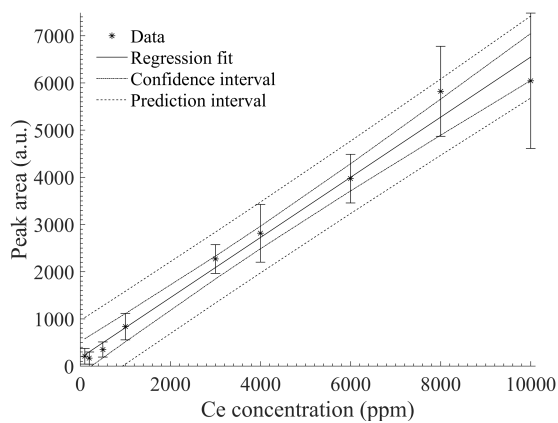
3.3 Conclusion

The detection of Ce was demonstrated via LIBS in a static liquid configuration. The %RSD for the static liquid configuration averaged around 18.5%. This relatively high value is a result of the splashing effects on the vial surfaces used and fluctuations in laser energy.
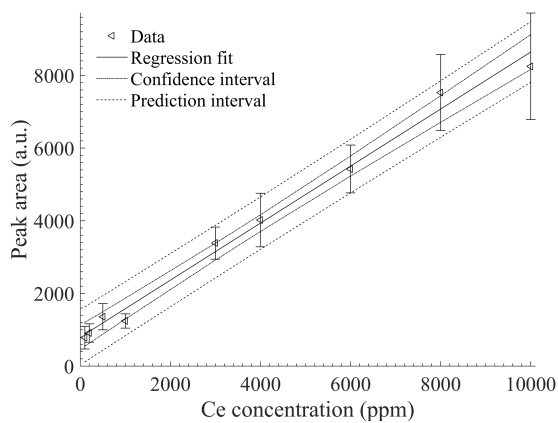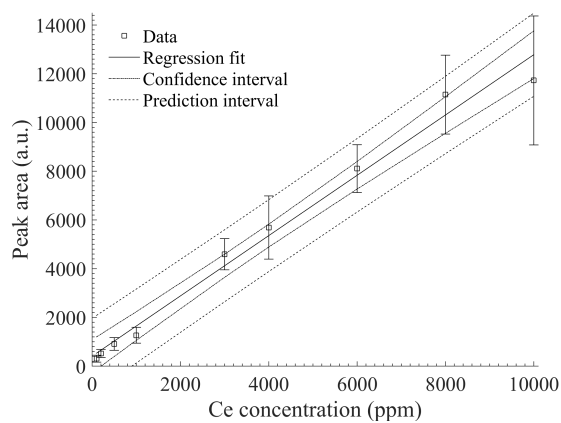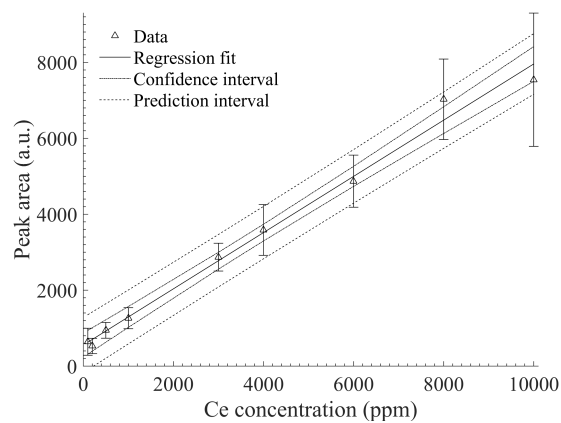
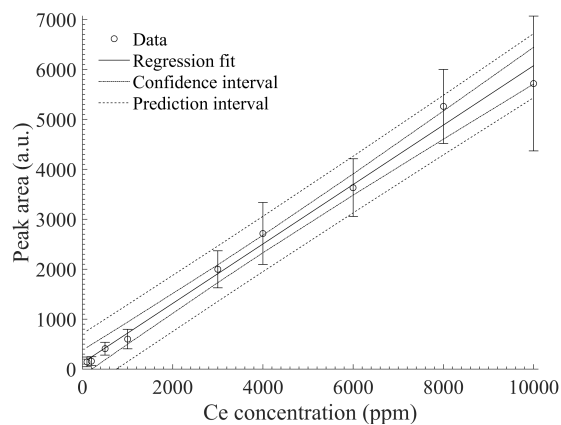Figure 3.8: Calibration curves for the Static liquid setup. (a) Curve from Ce 413.765 nm peak, (b) curve from the Ce 418.660 nm peak, (c) curve from the 428.999 nm peak, (d) curve from the 446.021 nm peak, and (e) curve from the 457.028 nm peak.

Calibration curves were generated for the static liquid case and R^2 values ranged from 0.98 to 0.99. Of the different Ce lines explored, the 418.660 nm peak had the best LOD of 403 ppm.

This study has demonstrated the LIBS capability to measure Ce in a liquid using the static surface approach without loss of material. The %RSDs were high as stated above, more shots and a slower repetition rate could improve this. However, this technique would be extremely difficult to implement for a molten salt because it is anticipated that the splashed salt, if it formed a film, would also quickly etch the surface of the glass/quartz and thus reduce the signal over time.

4

Aerosol System Design and Aqueous Testing (Phase II)

In this phase of the work, a new LIBS system was established in order to explore liquid aerosols in preparation for studying molten salts using an aerosol approach. The overall design concept and specifics of the design will be addressed. In addition, initial testing of the designed system was done using an aqueous sample in order to gain insight into aerosol-LIBS detection and to work out challenges in the design and assess the system overall.

4.1   Early Experimental Design

4.1.1   Aerosol Generation

Typically, aerosol generation is done using a Meinhard nebulizer or some form of ultrasonic nebulization. These methods will not work for the given application due to (1) the extreme operating temperature and (2) potential clogging of the system as salt flows through the tip aperture. However, one atomizer, called the Collison nebulizer (manufactured by BGI Inc.), has been identified as a possible means of generating a molten salt aerosol. The Collision nebulizer is made entirely out of stainless steel, and therefore can handle the high
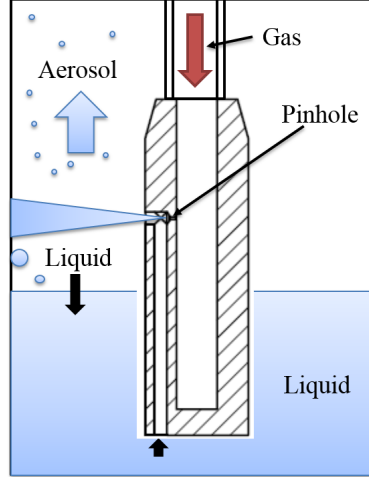
Figure 4.1: Illustration of how the Collision nebulizer works.

temperatures. In addition, the Collison nebulizer has reduced likelihood of clogging since the gas is passed through the nozzle aperture rather than the fluid. The fluid is drawn up into the gas stream as a result of a vacuum created by the compressed gas flow through the nozzle (see Figure 4.1). As the gas and fluid mix in the gas stream, and also as the fluid impacts the nebulizer wall, an aerosol is generated that is typically on the order of 2 microns (for a compressed air and water system). One key parameter influencing the aerosol generation of a fluid is the viscosity. K. R. May[44] investigated the performance of the Collison nebulizer with fluids ranging from 1 mPa·s (water) to 500 mPa·s (silicone mixture). Results from this study indicated that at higher viscosities an aerosol could be generated; however, higher input pressures were required and the overall aerosol concentration (number density) was reduced. Molten salt at 500°C has a viscosity of 146 mPa·s which is well within the range studied. As a result, it is expected that the molten salt can be formed into an aerosol via the Collison nebulizer.

4.1.2 Basic Design Concept

An illustration of a molten salt-LIBS configuration using a Collison nebulizer is shown in Figure 4.2. In the first step of the process, cold argon gas must be heated up to 500°C before
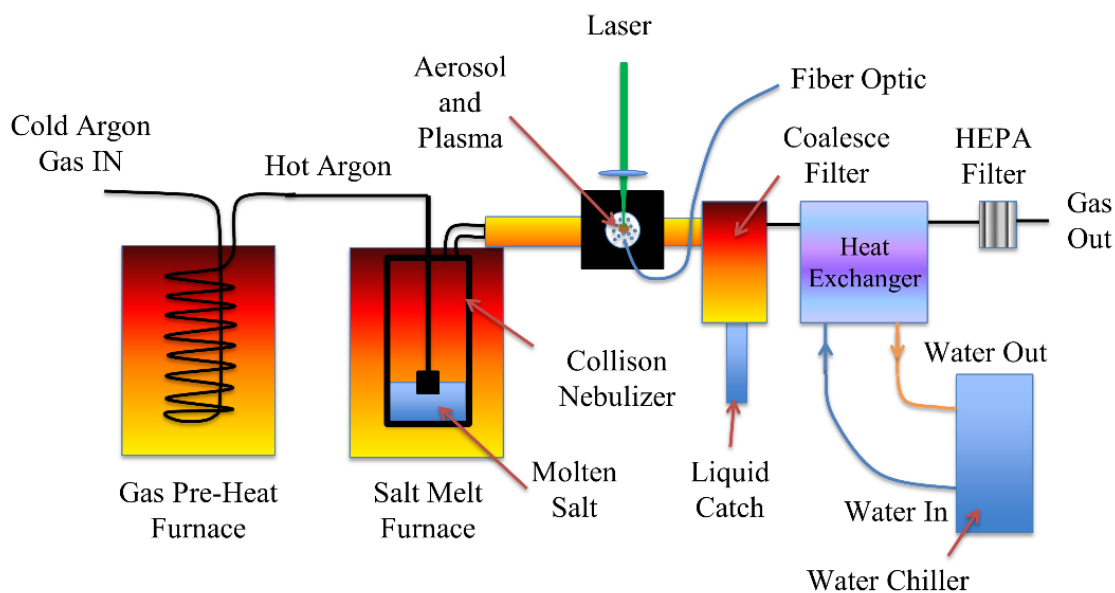
Figure 4.2: Illustration of the proposed aerosol-LIBS setup.

entering the Collison nebulizer to prevent salt freezing on mixing. Next the gas enters the Collison nebulizer where the molten salt aerosol is generated. The flow of argon and molten salt droplets then passes into a sampling chamber with quartz or sapphire sight windows. Through the windows, laser light is focused into the aerosol stream to create plasma. Optics and a fiber optic cable are positioned just outside the window at 90° from the incident laser to collect the spectral light generated as the plasma cools. The aerosol stream then passes into a coalesce filter which removes the aerosol from the gas stream. The hot gas then passes through a heat exchanger to cool it down to ambient temperatures before being passed through a HEPA filter and vented into the exhaust system. The following sections will discuss each aspect of this concept in detail.

4.1.3 Carrier Gas Heating

To prevent freezing of the salt during aerosol generation, it is crucial that the input gas be at an operating temperature near 500°C, or at least greater than 350°C prior to entering the nebulizer. A simple heat exchanger system was made to fit inside a 1350 W Kerr Lab jewelers furnace with an inside cavity with dimensions of 3.2 in. in diameter and 6 in. deep. Several calculations were done to determine the required operating parameters of this configuration in order to heat the gas stream at the assumed maximum gas flow rate of 20 L/min (based on Collision nebulizer specifications). The first step was to determine if the available furnace was sufficient to heat the gas. The amount of energy was found using:

$$Q_{in} = \dot{m} C_P (\Delta T) \tag{4.1}$$

where Q_{in} is the required heat input, $\dot{m}$ is the mass flow rate, C_P is the heat capacity and ΔT is the temperature difference between the inlet and outlet gases. For argon, in the temperature and pressure range of interest, C_P is 0.52 kJ/kg K[45]. The mass flow rate was determined to be 4.28×10^{-3} kg/s using the density of argon at 300 K (12.8 kg/m^3)[45]. As a result, Q_{in} was calculated to be 1057 W. The available furnace can operate up to 1350 W; therefore, the furnace is sufficient for this application.

An important parameter to be determined is the diameter of the tubing used for the coils of the gas heating heat exchanger. At smaller diameters, the heat transfer within the tubing itself is enhanced as well as an increased length of the tubing that can fit inside the furnace cavity. However, the smaller the tube diameter, the larger the pressure drop will be. Three tubing sizes available are 0.125 in., 0.25 in., and 0.375 in. diameters. Based on the tubing diameter, the length of the coil, pressure drop, and heat transfer can be identified. The length of the tubing within the furnace cavity can be calculated by assuming the tubing is coiled like a spring at a diameter of 2.5 in. by 6 inches long (safe inside dimension of the cavity). Using this, the lengths are found to be 9.5 m, 4.75 m, and 3.2 m for the 0.125 in.,

0.25 in., and 0.375 in. cases, respectively. The pressure drop between these systems was determined using:

$$\Delta P = f \frac{L}{D} \frac{\rho \nu^2}{2} \tag{4.2}$$

where f is the friction factor, L is the tubing length, D is the inside diameter, ρ is the density, and ν is the fluid velocity. The only parameter that is unknown for these cases is the friction factor, which is a function of the surface roughness and the Reynolds (Re) number. The Re number was calculated to be 1.96×10^5, 5.98×10^4, and 3.5×10^4 for the 0.125 in., 0.25 in., and .0375 in. cases, respectively at the max assumed flow rate of 20 L/min. Assuming a surface roughness of 0.000015 and using the Moody chart, the friction coefficients were calculated. The resulting pressure drop was 8.4 kpsi for the 0.125 in. diameter tubing which is too high to be of practical use. The pressure drop for the 0.25 in. case was 11.5 psi and the pressure drop for the 0.375 in. case was 0.5 psi. Both the 0.25 in. and 0.375 in. diameter cases yield pressure drops that are sufficiently small to be applied to this application. However, since the coils are to be made by hand, the 0.25 in. diameter was selected due to difficulty in bending the 0.375 diameter tubing.

In the gas heating design configuration, heat must be transferred from the furnace to the coils and from the coils to the gas. Several assumptions can be made to simplify the calculations. First, it is assumed that the primary heat transfer mode between the furnace walls and the coils will be radiation. This is a valid assumption since there will be little physical contact between the furnace wall and the coils. The effects of convection in the furnace cavity were ignored due to size constraints of the cavity. The second assumption is that heat transfer through the tubing walls will be fast. This is practical since the tubing wall is thin and the thermal conductivity of the stainless steel wall is high.

The amount of energy required to heat the gas phase has been calculated using Eqn. 4.1. Applying an energy balance between the required energy to heat the fluid and the energy gained from the furnace walls via thermal radiation, the operating temperature of the furnace

can be determined. The heat transfer from the furnace walls to the coils is:

$$Q_{in} = \sigma A(T_{wall}^4 - T_{surface}^4) \tag{4.3}$$

were σ is the Boltzmann constant, A is the surface area of the coil, T_{wall} is the temperature of the furnace wall, and $T_{surface}$ is the temperature of the coil. Setting Eqn. 4.1 equal to Eqn. 4.3 provides an energy balance for the system. Using the average temperature between the inlet and outlet gas as the coil temperature, the wall temperature can be obtained. The calculation yields an operating temperature of 620°C which is well within the operating range of the Kerr Lab furnace.

To verify that heat applied to the coils can be transferred into the gas via convection in the tubing, the heat transfer coefficient (h) was calculated. Here, a Nusselt (Nu) correlation can be used to identify h. The correlations are as follows:

$$Nu = \frac{(f/8)(Re - 1000)Pr}{1 + 12.7(f/8)^{1/2}(Pr^{2/3} - 1)} \tag{4.4}$$

$$h = \frac{Nuk}{D} \tag{4.5}$$

where Pr is the Prandlt number and k is the thermal conductivity of the fluid. In this case the Nu number was calculated to be 115 and h was calculated to be 756 W/m^2 K. It is difficult to calculate the actual heat transfer in this case, since neither the coil surface temperature, nor the heat flux is constant. However, since h is large it is assumed that heat transfer into the fluid will not be the limiting factor. Indeed, the rate of heat transfer will depend on thermal radiation from the furnace.

The stainless steel heat exchanger designed above was made using the 0.25 in. tubing and is shown in Figure 4.3. The final dimensions for the heat exchanger was 2.75 in. in diameter and 5.5 in. long. The total length of tubing is 4.3 m.

Figure 4.3: Picture of the heating coil manufactured in-house.

4.1.4 Collison Nebulizer and Seals

The Collison nebulizer purchased from BGI, Inc. is shown in Figure 4.4. Basic components of the nebulizer are the jar, lid, tip, and inlet. The nebulizer can be purchased with 1, 3, 6, or 24 jet ports. In general, as the number of jets increase, the concentration (number density) of the aerosol increases. The amount of material used per jet configuration ranges from 1.5 ml/h to 66 ml/h in a water system. Since experiments need to be conducted to verify particle size and concentration, the 3 jet system was selected as a starting point since it is in the middle of the lower range. For the water system, the 3-jet system uses approximately 4.5 ml/h to 14.1 ml/h of sample depending on the input pressure of the gas. As the input pressure increases, the amount of material consumed also increases. For a water and air system, the recommended pressure range is between 20 psi and 100 psi. The pressure drop in the gas flow across the jets is substantial and will drop to the minimal pressure required to push the gas stream through the remainder of the system. As such, pressure measurements will be made at the inlet and outlet of the nebulizer to verify the actual pressure conditions
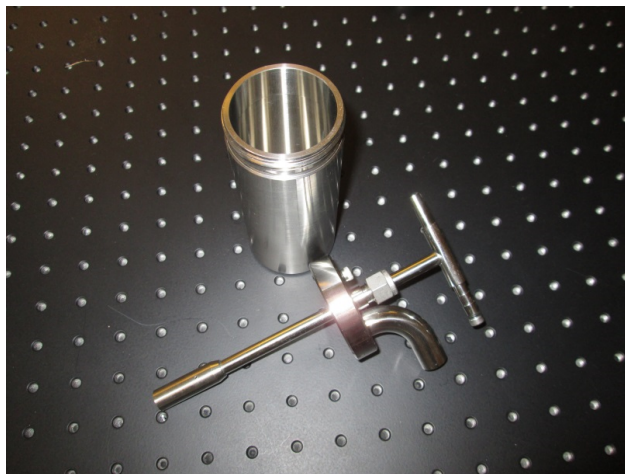
Figure 4.4: Picture of the Collison nebulizer.

of the aerosol generation.

The Collison nebulizer is constructed completely of stainless steel and therefore, should withstand the high temperature and corrosive environment proposed in this study. However, the unit has several Teflon and rubber seals that need to be modified in order for the unit to function at high temperature. Three seals needed addressed, one between the gas line in and the lid, another between the lid and the canister, and lastly, between the gas line in and the jet head. The seal between the gas line and lid was easily fixed by replacing the Teflon ferrules in the Swagelok fitting with stainless steel ferrules. The seal between the gas line and jet head was also easily address by using a high temperature thread sealant called Deacon 770-L which is stable up to 950°F (510°C). The last seal is the most challenging due the large (2.25 in) diameter of the unit. In the original design of the product, the manufactures had used a simple rubber o-ring. A high temperature alternative to rubber o-rings is using a ceramic fiber braid or wick material that can be compressed to form a seal. In this aqueous phase of the work, the simple rubber o-ring was used.

4.1.5 Sampling Chamber and Sight Glass

Once the aerosol has been generated in the Collison nebulizer it is transported in the carrier gas from the nebulizer into a sampling chamber. The sampling chamber design consisted of
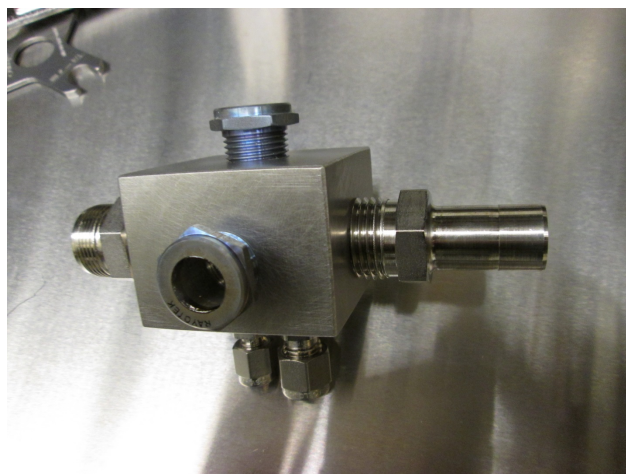
Figure 4.5: Picture of the sampling chamber complete with inlet and outlet ports, sight windows, and temperature and pressure system ports.

a solid stainless steel cube with seven different ports that had been drilled into it leaving a central cavity for the plasma formation. The sampling chamber along with connection ports is shown Figure 4.5. Two 1/2 NPT ports were used to deliver and remove the aerosol stream from the chamber. Three other ports were used to fit 3/8 NPT sight glass windows from Rayotek. Through these windows the laser light was focused and the return spectra collected. The remaining two ports were for the insertion of a thermocouple and for collecting pressure measurements within the chamber during operation. This sampling chamber was designed such that the plasma formation would be within the aerosol stream itself.

Selection of materials for the optical ports was limited due to the high temperature and corrosive environment. For the molten salt application, only two materials were possible candidates, quartz and sapphire. The optical properties for both are very good and both are capable of the high temperature required. The quartz has a tendency to etch in the molten salt environment over time, but the sapphire will not etch due to excellent chemical resistance. The cost of sapphire is significantly greater, and as a result, the quartz windows were selected for initial testing at high temperature and plain glass windows were selected for the aqueous testing during phase II of the project.

Figure 4.6: Photo of the coalescing filter housing and filter element.

4.1.6 Aerosol Removal from the Gas Stream

Once the aerosol stream leaves the sampling chamber, the liquid droplets must be removed before cooling the gas stream to prevent salt freezing in the cooling lines. Several methods were explored to remove the aerosol including mixing/freezing, filtering, and condensing. However, at length, a coalescing filter was selected from United Filtration Systems, Inc. This coalescing filter is shown below in Figure 4.6. The filter itself is designed with three layers of stainless steel mesh that is designed to collect and coalesce liquid droplets down to the 1 micron size. The unit is equipped with high temperature seals which allow for use up to 540°C operation. The collected liquid drains to a 1/4 NPT port at the bottom of the unit. A Swagelok sample bottle will be used to collect the liquid for further validation via ICP-MS. The pressure drop across the coalescing filter is unknown and will be measured.

4.1.7 Gas Cooling and Cleaning

Following the coalescing filter, the gas stream at 500°C must be cooled to room temperature prior to passing through a HEPA filter and being released into the exhaust system. The heat removal system must be capable of removing at least 1057 W of energy. The easiest method would be to use a heat exchanger with water as the cooling fluid. Most heat exchangers
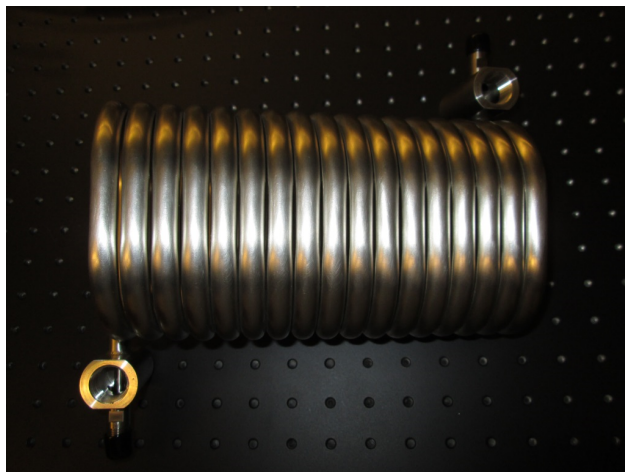
Figure 4.7: Photo of the tube in tube heat exchanger.

designs for this scale are not designed to operate at temperatures up to 500°C, nor are they designed to operate with such a large temperature differential. However, one style of heat exchanger called a tube in tube heat exchanger fits the application nicely. A tube in tube heat exchanger is two concentric tubes coiled around such that their walls do not touch. The advantage of this system is that it is easily sealed at high temperature. In addition, since the tubes are not touching, significantly more thermal stress (larger temperature difference) can be handled. A tube in tube heat exchanger was identified and purchased from Exergy miniature heat exchangers. The heat exchanger is shown in Figure 4.7.

The heat exchanger performance was calculated (for the assumed maximum conditions, 20 L/min) and results were provided by Exergy. The pressure drop on the argon side of the heat exchanger is 12.2 psi and on the water side 0.62 psi. The water input temperature was 23°C and the exit temperature was 35°C at a flow rate of 1.24 L/min. Due to the high temperature of the argon gas, some boiling in the heat exchanger may occur, however, because flow rates are high, boiling should not present a problem.

To pump and cool the water used in the gas cooling system, an Isotemp II water circulator/chiller was used. The Isotemp II has a cooling capacity of 1000W at 20°C, which is lower than the required amount. However, at 35°C the heat removal is increased to approximately 1400 W. As a result, the chiller was set to circulate water at a higher temperature to ensure

Figure 4.8: Picture of the aerosol system assembly.

energy removal. Once the gas stream was cooled, it was passed through a HEPA filter before being dumped into the lab exhaust system.

4.1.8 Assembly and Laser Mounting

The entire system was installed on the inside of an inert atmosphere glovebox. However, the glovebox was not sealed yet in order to better test the system using aqueous fluids and to allow for easy assess durning the initial shakedown period. Figures 4.8 and 4.9 show all of the different components as they are assembled into the whole aerosol-LIBS system.

As a result of working in the glovebox, a method to mount the Q-smart 450 Nd:YAG laser to the glovebox was developed as shown in Figure 4.10. Here, a 12 mm x 600 mm x 900 mm optical breadboard was mounted to the side of the glovebox using 8 right angle pieces. The laser was then mounted vertically and mirrors were used to reflect the laser beam through a quartz window installed in the glovebox. As a result of this setup, the laser light was easily transported into the glovebox. Blackout materials were installed around the
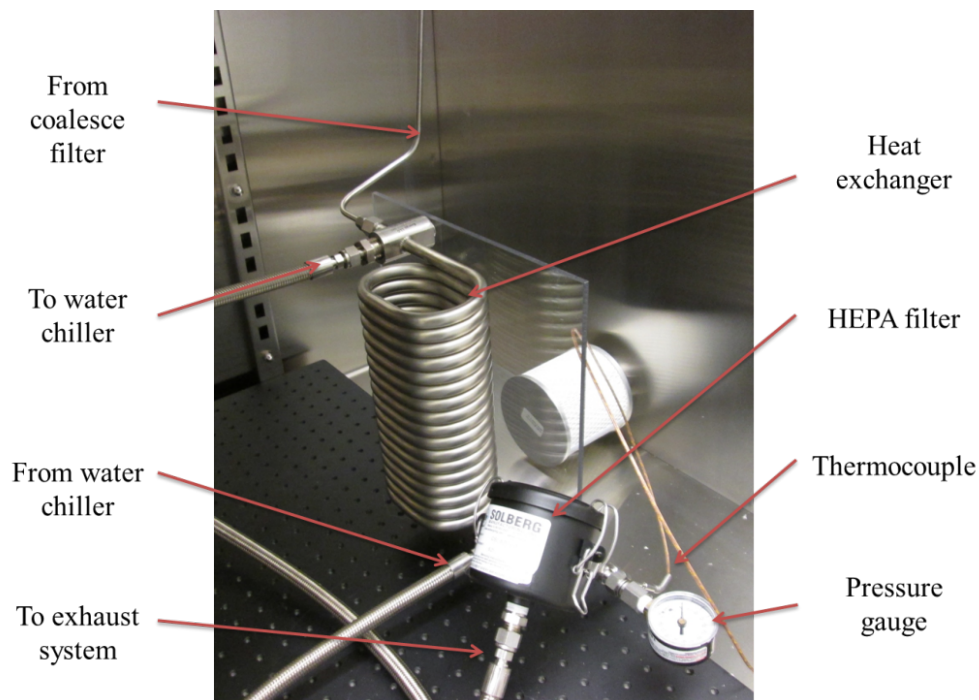
Figure 4.9: Picture of the installed heat exchanger system.

glovebox in order to adhere to laser safety standards.

4.2 Initial Testing using Aqueous Media

4.2.1 Materials and Methods

Before operating at high temperature, room temperature testing was done in order to gain experience with the aerosol-LIBS system prior to working with molten salts. Here, DI water was used as the working fluid with additives of rare-earth elements (Ce, Nd, and Gd). All the salts were purchased from Alfa Aesar. Concentrations of Ce and Gd ranged from 100 ppm to 10,000 ppm and the Nd concentration was set at 1,000 ppm for all samples. Table 4.1 shows the concentrations of the samples that were made. Here, each element was tested with low (100 ppm), medium (6,000 ppm for Gd and 3,000 ppm for Ce), and high (10,000 ppm) concentrations of another element and vice versa in order to see matrix effects if any. Samples were prepared and run using the aerosol-LIBS system and then verified using ICP-MS.

Figure 4.10: Picture of the Q-smart laser mounted to the glovebox and optics used to direct the beam through the window and into the glovebox.

Table 4.1: Prepared samples showing the concentrations for Ce and Gd. The Nd concentration was set at 1,000 ppm for each sample.

| Standard	ppm Gd	ppm Ce	Standard	ppm Gd	ppm Ce
1	100	100	19	100	100
2	100	500	20	500	100
3	100	1,000	21	1,000	100
4	100	3,000	22	3,000	100
5	100	6,000	23	6,000	100
6	100	10,000	24	10,000	100
7	6,000	100	25	100	3,000
8	6,000	500	26	500	3,000
9	6,000	1,000	27	1,000	3,000
10	6,000	3,000	28	3,000	3,000
11	6,000	6,000	29	6,000	3,000
12	6,000	10,000	30	10,000	3,000
13	10,000	100	31	100	10,000
14	10,000	500	32	500	10,000
15	10,000	1,000	33	1,000	10,000
16	10,000	3,000	34	3,000	10,000
17	10,000	6,000	35	6,000	10,000
18	10,000	10,000	36	10,000	10,000
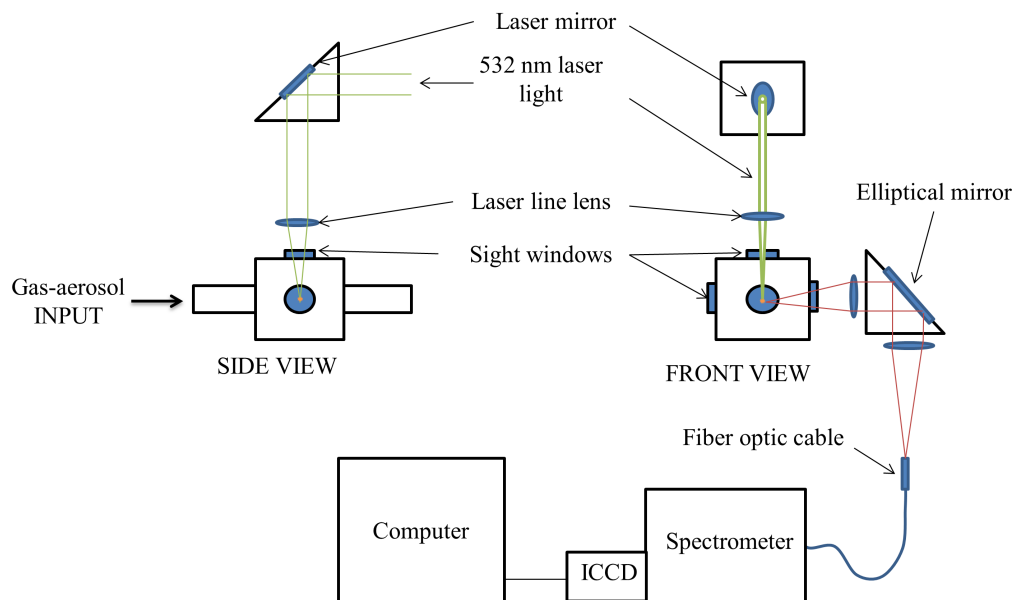
Figure 4.11: Representation of the aerosol system experimental setup and optics.

The salt solutions were loaded into a 3-jet Collison nebulizer and argon gas was used as the mixing gas to create the aerosol. The aerosol stream passed through a 12.7 mm diameter by 75 mm tube to a sampling chamber that was fitted with 3/8 NPT glass sight windows from Rayotek, Inc. as shown in Figures 4.5 and 4.11. The laser light was focused into the sampling chamber using a plano-convex lens with a 50 mm focal length to create the plasma. Light from the plasma was collected using a 25 mm diameter plano-convex lens with a 75 mm focal length. Light was directed at 90° using a dielectric elliptical mirror and then through a 25 mm diameter plano-convex lens with a 100 mm focal length. The latter lens focused the plasma light into a 2 m fiber optic cable with a 50 μm core purchased from Ocean Optics. This fiber optic cable carried the light signal to the spectrometer and detector.

The argon gas flow rate was measured using a Key Instruments 1G08 R3 flow meter. The aerosol droplets generated in the Collison nebulizer were characterized using a scanning mobility particle sizer (SMPS). The SMPS system used a TSI 3080 electrostatic classifier, a TSI condenser particle counter, and model 3081 DMA. The aqueous droplets dried very quickly in the ultra-pure argon and the SMPS system was not able to directly measure the wet diameter. As a result, a drying column was used to first dry the aerosol and a dry particle

diameter was obtained. From the dry diameter, the wet diameter could be calculated from knowledge of the material volume fractions (concentrations).

For each sample run, ten repetitions were collected, each consisting of 200 laser shots. In this case, the Andor Solis software was operated in kinetic mode so a spectrum for each laser shot was recorded. The 200 laser shots were then averaged to provide a single spectrum representing that particular repetition. The ten average spectra generated from each sample were then used to create a single point on a calibration curve. Calibration curves were generated for the low, medium, and high cases and a comparison was made between different emission lines for each case.

4.2.2 Results and Discussion

To better understand the operating conditions of the aerosol-LIBS system, initial optimizations were done. First, the nebulizer flow rate was explored to find the optimal flow rate from a LIBS signal perspective. It was observed that the light intensity increased as the gas flow rate decreased. This may be a result of a decreasing number of droplets within the stream which interfere with the incoming laser light. It was determined that the ideal carrier gas pressure was 10 psig prior to the nebulizer; this corresponded to a flow rate of approximately 1.9 liters per minute (lpm). At this flow rate and pressure, approximately 5 ml of solution was used per hour.

Next, the optimal gate delay and gate width were optimized by running a series of experiments while varying these parameters. As the gate delay increased, the signal decreased but the background or continuum noise decreased at a faster rate. As a result, an optimal gate delay was found to be 6 μs with a gate width of 20 μs. The laser power was also varied to determine the optimal energy. At different laser energies, the plasma changed position and shape within the aerosol-gas stream. With higher energies, the plasma became more elongated which created challenges in capturing the light. As a result, a laser energy of 55 mJ was selected to provide good plasma shape and signal. Other laser parameters were the
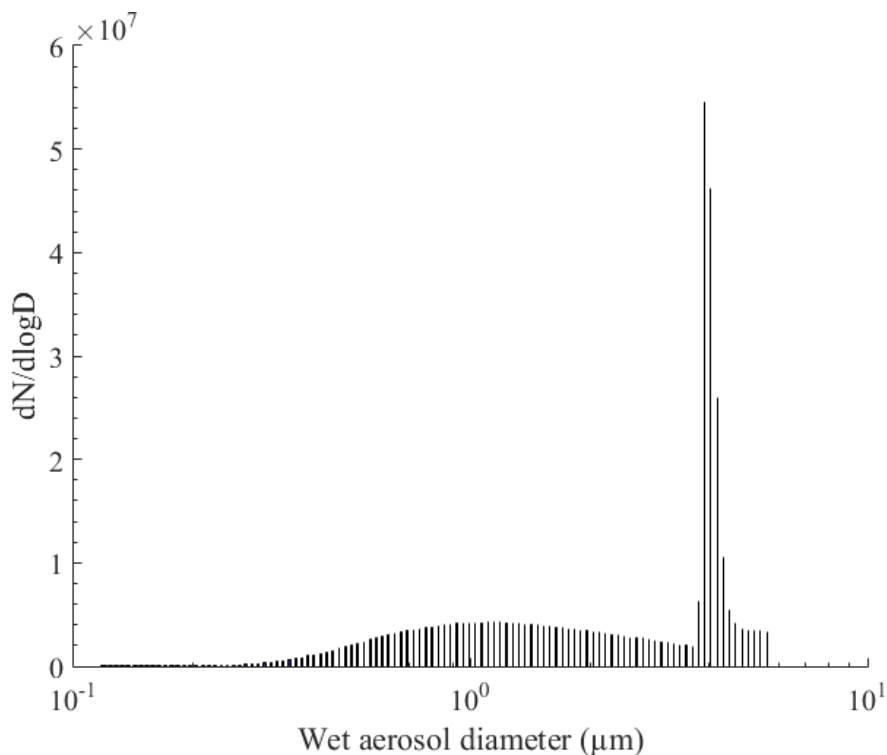
Figure 4.12: A typical size distribution plot for the aerosol generated in this work. The specific plot was generated from sample 18 (10,000 ppm Gd, 10,000 ppm Ce).

gain and exposure time; these values were set at 3000, and 0.003 sec, respectively.

Figure 4.12 shows a representative wet particle size distribution obtained at 10 psi and 22 °C for sample 18 (10,000 ppm Gd and 10,000 ppm Ce). The observed distribution is bimodal with a total aerosol number density (N) of approximately 5.8×10^6 particles/cm^3 of gas. The intersection between the two log-normal distributions was used as a separation point and each size distribution was analyzed separately. As a result, the count median diameter (CMD) and geometric standard deviation (GSD) for each could be approximated. The first distribution had a CMD of 1.4 μm and a GSD of 1.2 and the second distribution had a CMD of 4.2 μm and a GSD of 1.0. The bimodal distribution observed may be a result of agglomeration of aerosol droplets within the drying column and tubing prior to the SMPS measurement.

A representative spectrum collected for the aerosol stream configuration is shown in Figure 4.13. In the lower wavelength range, there are numerous peaks from Ce, Gd, Nd,
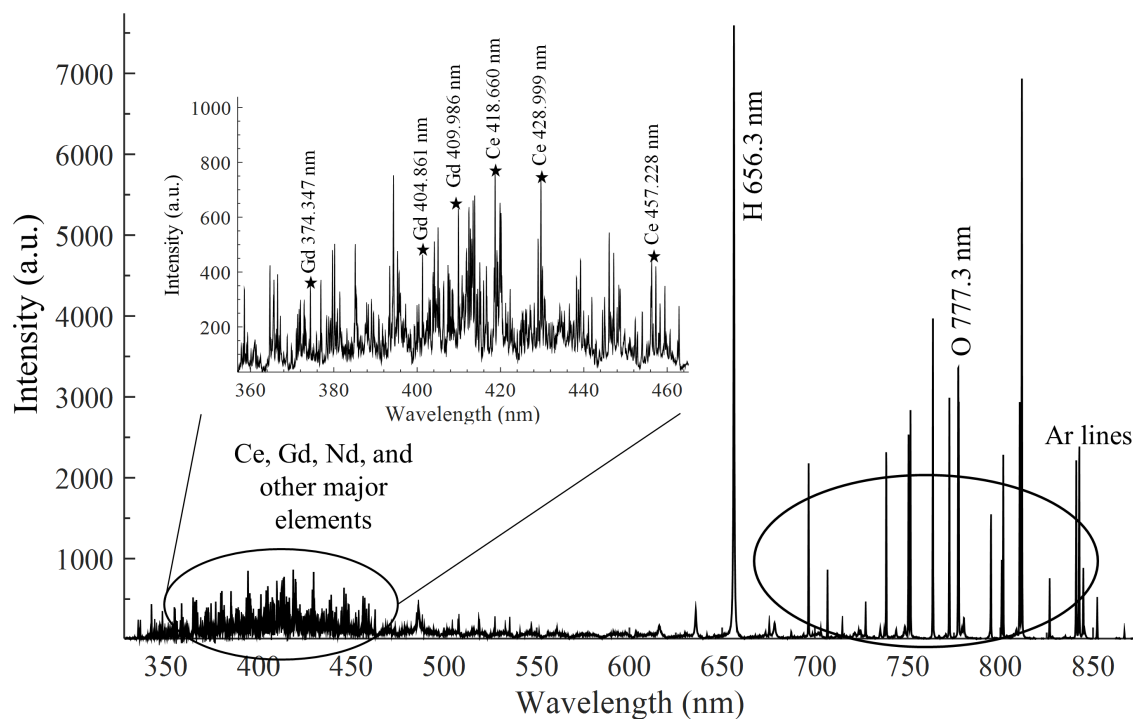
Figure 4.13: A typical spectrum showing the major element peaks and a close up of the spectral region with the minor element peaks. The spectrum was generated from for sample 18 (10,000 ppm Gd, 10,000 ppm Ce).

and Ar in the sample. In the upper range, all of the lines are from Ar with the exception of the H and O peaks shown. The Ce and Gd lines that had a SBR greater than 2.5 with low interference from other peaks were selected for analysis. This proved to be somewhat of a challenge because the rare earth elements Ce, Gd, and Nd have such a high density of lines in the lower range. In addition, due to the nature of the aerosol, strong Ar lines were also observed that added to interference. However, several lines were found[43] that met the criteria; they are the Ce 418.660 nm, Ce 428.999 nm, Ce 457.228 nm lines for Ce and the Gd 374.347 nm, Gd 404.986 nm, and the Gd 409.861 nm lines for Gd. Of the lines selected, the Ce 418.660 nm line may have a slight interference with a Gd 418.425 nm line but was included anyway due to its intensity. The Nd in the sample was not analyzed at this time since the concentration was constant throughout all the standards and peak intensities were too weak to be used as an internal standard.

An example of the variation between the different repetitions is shown in Figure 4.14 for

sample 4 (100 ppm Gd and 3,000 ppm Ce). In this example, the %RSD is around 5.5% as shown in Figure4.15 between 355 nm and 460 nm. In general, the %RSD's from the 36 samples ranged between 6% and 9% with an average around 7.5%. The best %RSD was 4.4% from sample 11 and the worst was 22% from sample 15. There were several potential factors that contributed to the variation in the spectra: (1) fluctuations in laser energy, (2) interaction of the droplets with the laser light, and (3) condensation at the bottom of the sampling chamber which can splash upwards onto the windows. The Nd:YAG laser used will vary around 5-10% and the best way to mitigate or reduce the error here is by using a sufficient number of shots per repetition. The extent of the droplet interactions is currently unknown; however, as a result of these interactions, the location of the plasma formation within the sampling chamber varied slightly from shot to shot. The effect of splashing or condensation on the windows was very noticeable when such instances occurred. In the duration of the 36 samples run, two such instances occurred in which the signal was drastically lower. In these cases, the system was dried and the experiments re-run. An additional source of variation that existed between samples is the position of the sampling chamber with respect to the incoming laser light, this is a result of small shifts in the system over time as a result of using only a single mounting point for the entire assembly.

The original intent was to use the Nd in the sample as an internal standard, however, the 1,000 ppm amount resulted in a spectral intensity too weak to be of an use in that capacity. Since Nd was too low, the other elements contained in the spectra were Ar, H, and O. The Ar gas is not actually part of the sample itself but is the carrier gas. As a result, if there were any variation with the gas flow, aerosol generation, or number of particles hit in the plasma, normalization with Ar will not help. Between the H and O, the O line has multiple Ar lines in close proximity. The H 656.3 nm line isolated and is the strongest line in the spectra, as a result, this line is the best normalization candidate available. The spectral region between 655 nm and 657 nm (width of the H line) was averaged and then the entire spectra was divided by this value. Each individual spectra was normalized in this way.
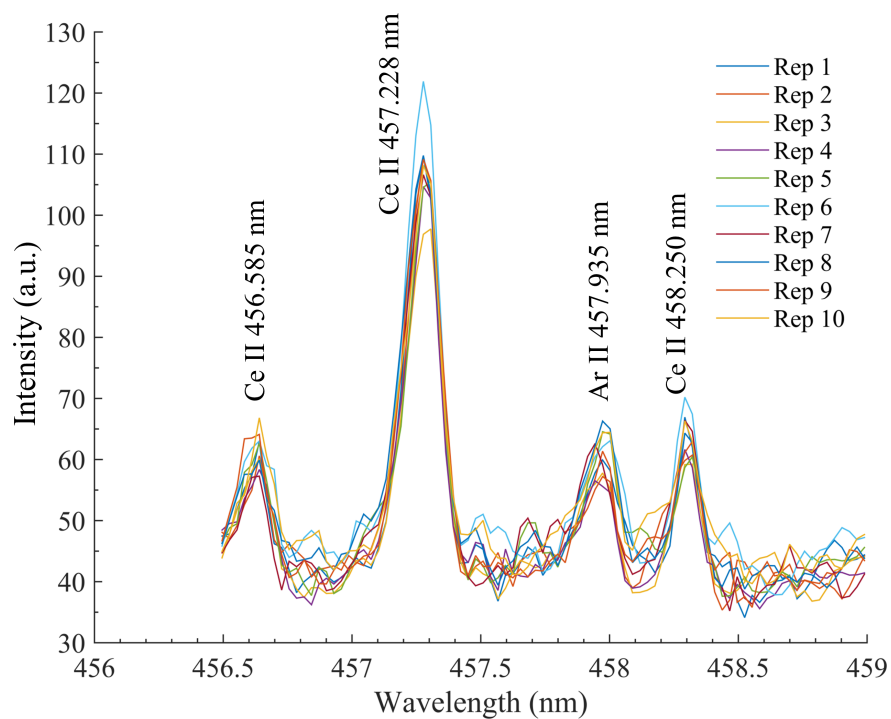
Figure 4.14: Difference between the 10 repetitions taken for sample 4 (100 ppm Gd and 3000 ppm Ce.)
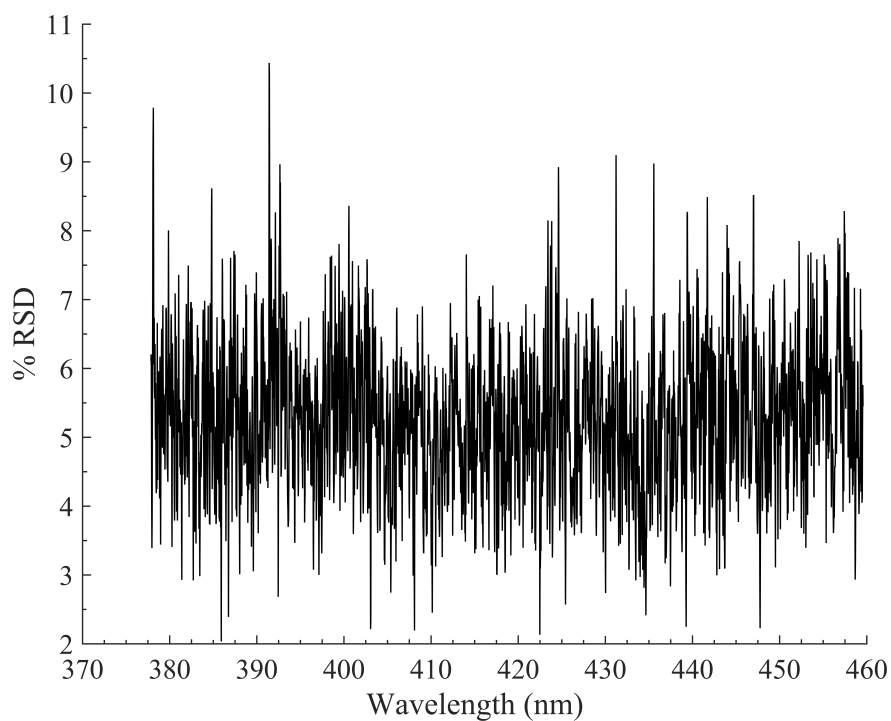

Figure 4.15: Typical plot of the %RSD's between the 10 repetitions taken for each sample. The specific %RSD shown is from sample 4.

The effects of the Low, Mid, and High concentrations of Ce and Gd in the spectra are shown in Figure 4.16. In Figure 4.16(a), it can be seen that the Gd 418.425 nm line interferes with the Ce line and the measurable area under the curve, without a deconvolution method, is significantly reduced as the Gd concentration increases. The Ce 428.999 nm and Ce 457.228 nm lines do not show a specific Gd interference line, however, The high density of Gd lines in the spectra contributes to the background in these regions. As a result, the intensities of the lines change slightly as an effect of the Gd concentration. This same background contribution is observed for the Gd lines with respect to the Ce concentration. In addition, the Gd 409.861 nm line has a Ce line interference that effects the peak area. These results show that there are some concentration effects on all of the peaks selected simply as a result of the background contribution.

Univariate Calibration Curves

A program written in MATLAB was used to determine the peak area and intensities of the Ce/Gd peaks of interest. In this program, the user can select the starting and ending point of the desired peak using a GUI. The program uses the trapezoid method to calculate the area under the curve, and then subtracts off the background area. The maximum between the start and end points was defined as the intensity of the line. The GUI was used to determine the area and intensity of all 10 repetitions for every sample. The peak areas for each sample were averaged to get a single point on the calibration curve. Error bars for the data point is the standard deviation between the 10 peaks.

Figure 4.17 shows calibrations curves for Ce lines generated using the peak areas and peak intensities. Table 4.2 shows the regression coefficients, R^2 values and LOD for the various lines. As expected, the Ce 418.660 nm line shows significant variation with respect to the peak area as a result of the Gd 418.425 nm line. The Ce 418.660 nm calibration curves generated using the peak intensity does not show a major dependence on the Gd concentration. However, there is a minor dependence as a result of the Gd background
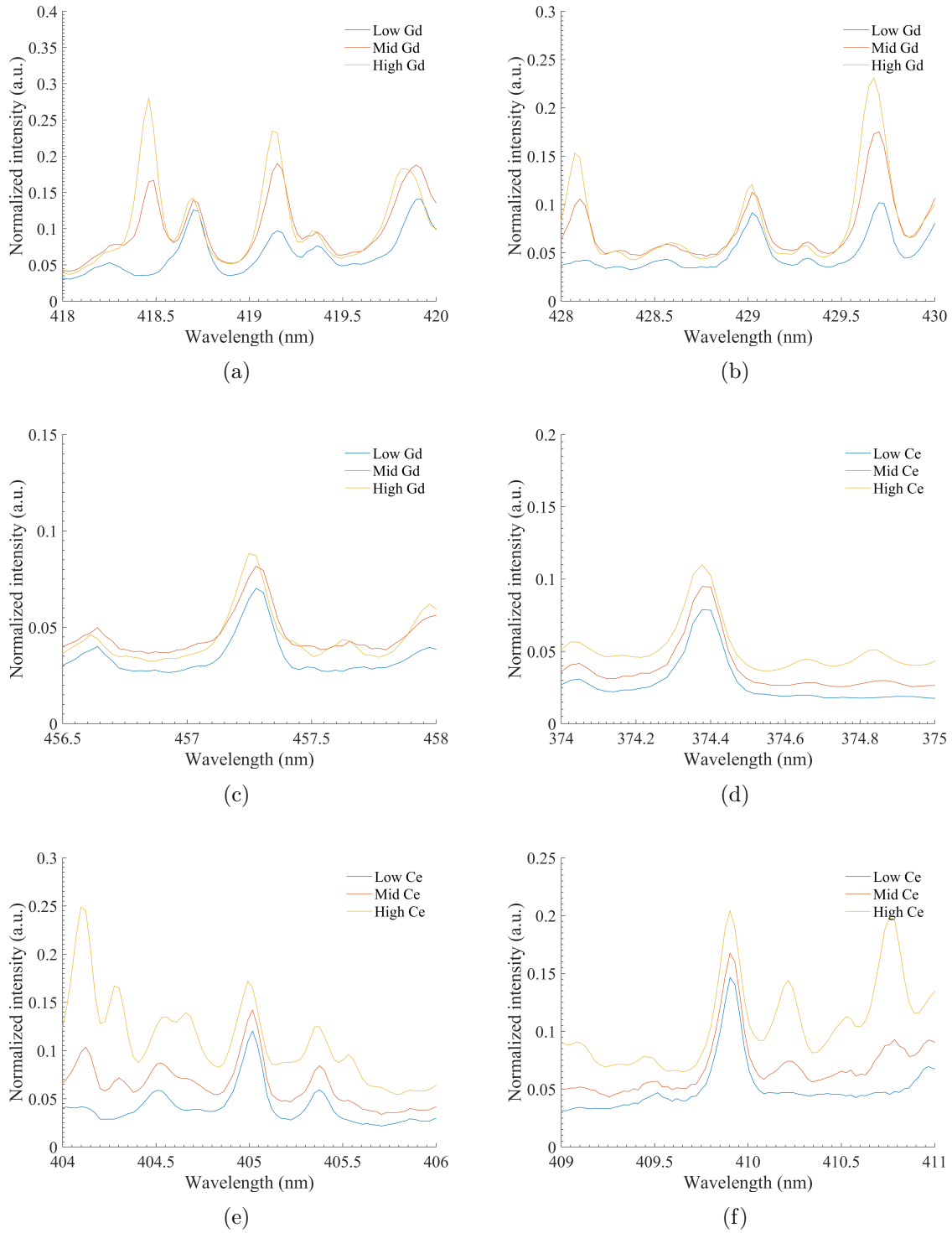
47

Figure 4.16: The variation of the Ce and Gd spectral lines as a function of the Low, Mid, and High cases explored. (a) The 418.660 nm line at 3,000 ppm Ce (b) 428.999 nm line at 3,000 ppm Ce (c) 457.228 nm line at 3,000 ppm Ce (d) Gd 374.347 nm line at 3,000 ppm Gd (e) Gd 404.986 nm line at 3,000 ppm Gd (f) Gd 409.861 nm line at 3,000 ppm Gd.

contribution. For example, on closer examination of the y-intercept(b_0), it is clear that as the Gd concentration increases, b_0 also increases. Despite this increase, the regression confidence intervals between the three cases are very similar. The Ce 428.999 nm and Ce 457.228 nm peaks areas show less dependence on the Gd concentration than the Ce 418.660 nm peak, however, slight variations in the slope exist. The curves generated using the peak intensities are more effected by the Gd background contribution. Overall, the Ce 418.660 nm curve generated with the peak intensities has the least variation between the Low, Mid, and High cases, has the some of the lowest LOD and is therefore recommended for use. Due to the relatively low variation between Low, Mid, and High Gd cases for the recommended 418.660 nm peak, a combined calibration curve was generated using all 36 samples and is shown in Figure 4.19(a). The R^2 for this curve is 0.992 and the LOD is 189 ppm.

Figure 4.18 shows the Gd calibrations curves using both the area and intensity approaches. Table 4.3 shows the regression coefficients, R^2 values and LOD for the various peaks. The Gd curves are similar to the Ce curves in that the Ce background contributes to a change in the y-intercepts for those generated using intensities and slope dependence for the curves generated using areas. Overall the Gd 409.861 nm curve generated using area appears to have the least variation and relatively good LOD. As in the Ce case, a calibration curve using the recommended peak has been generated using all 36 samples. This calibration curve is shown in Figure 4.19(b). The R^2 is 0.994 and the LOD is 316 ppm.

To validate the calibration curves for Ce and Gd, two unknown samples were run with Ce and Gd concentrations within the ranges studied. Table 4.4 shows the values for unknown samples 1 and 2 generated from the combined calibration curves. When comparing the predicted and actual values for the concentration, the predicted values are nearly all within the estimated error of the measurements. Interestingly, the calibration curves over estimate the concentration for both Ce and Gd, though the Gd concentration is nearly exactly estimated. The predicted values for unknown sample 2 are under estimated by approximately 15%. Overall, the validations of the univariate calibration curves generated for the aque-
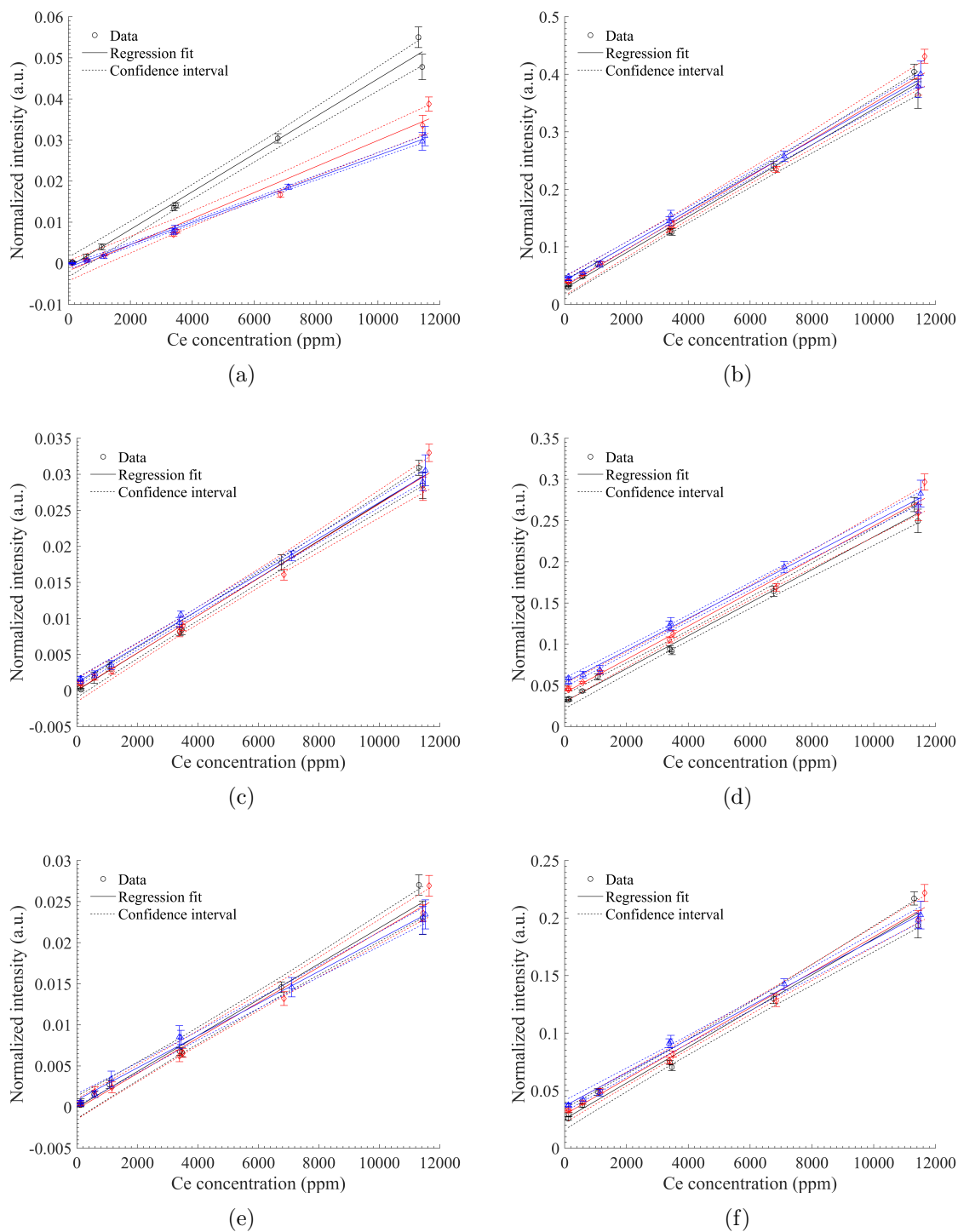
Figure 4.17: Comparison between Ce calibration curves using peak area and intensities. The black, red, and blue data set sets represent the Low, Mid, and High cases, respectively. (a) The 418.660 nm using area (b) 418.660 nm line using intensity (c) 428.999 nm line using area (d) Ce 428.999 nm line using intensity (e) Ce 457.228 nm line using area (f) Ce 457.228 nm line using intensity.

Table 4.2: Tabulation of the R^2, b_1, b_0, and LOD for the Ce calibration curves.

| 418.660 nm (Area)	b_1	b_0	R^2	LOD
Low Gd	4.582e-06	-9.33e-04	0.990	129
Mid Gd	3.172e-06	-0.0018	0.980	115
High Gd	2.714e-06	-9.00e-04	0.998	179
418.660 nm (Intensity)	b_1	b_0	R^2	LOD
Low Gd	3.120e-05	0.0277	0.992	163
Mid Gd	3.182e-05	0.0316	0.991	168
High Gd	3.045e-05	0.0412	0.998	183
428.999 nm (Area)	b_1	b_0	R^2	LOD
Low Gd	2.600e-06	-6.526e-06	0.995	369
Mid Gd	2.585e-06	4.945e-05	0.987	196
High Gd	2.497e-06	0.0011	0.998	370
428.999 nm (Intensity)	b_1	b_0	R^2	LOD
Low Gd	2.000e-05	0.030	0.994	164
Mid Gd	2.026e-05	0.041	0.989	211
High Gd	1.948e-05	0.053	0.997	441
457.228 nm (Area)	b_1	b_0	R^2	LOD
low Gd	2.183e-06	-4.304e-05	0.987	283
Mid Gd	2.157e-06	-2.395e-04	0.989	332
High Gd	1.957e-06	8.543e-04	0.995	325
457.228 nm (Intensity)	b_1	b_0	R^2	LOD
low Gd	1.566e-05	0.0252	0.988	284
Mid Gd	1.544e-05	0.0292	0.993	223
High Gd	1.446e-05	0.0366	0.996	245
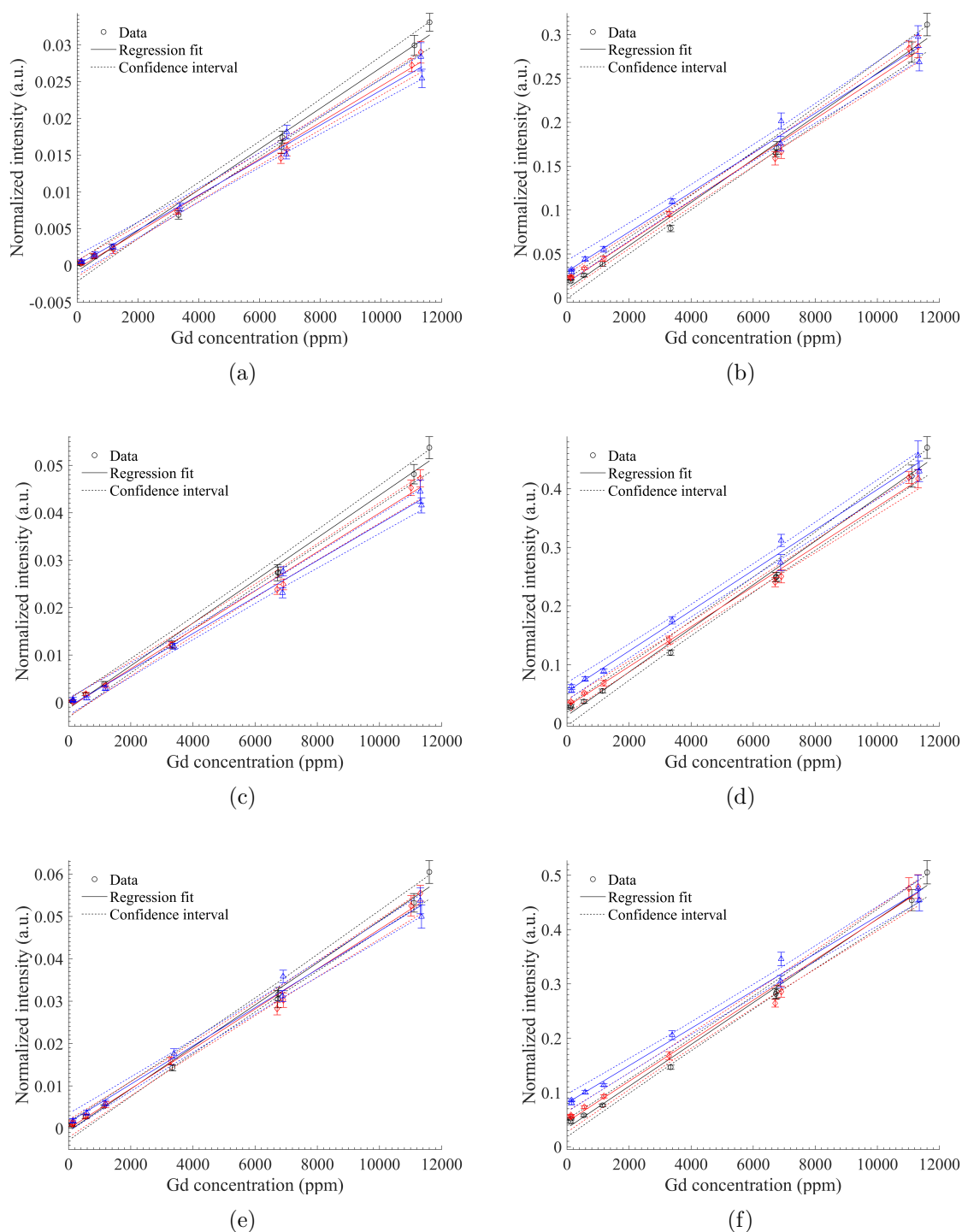
Figure 4.18: Comparison between Gd calibration curves using peak area and intensities. The black, red, and blue data set sets represent the Low, Mid, and High cases, respectively. (a) The 374.347 nm using area (b) 374.347 nm line using intensity (c) 404.986 nm line using area (d) 404.986 nm line using intensity (e) 409.861 nm line using area (f) 409.861 nm line using intensity.
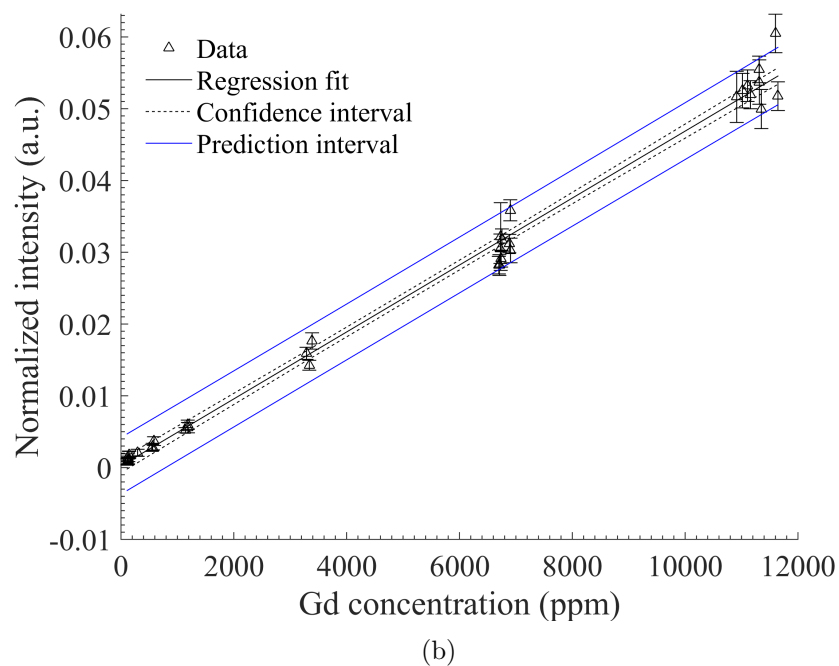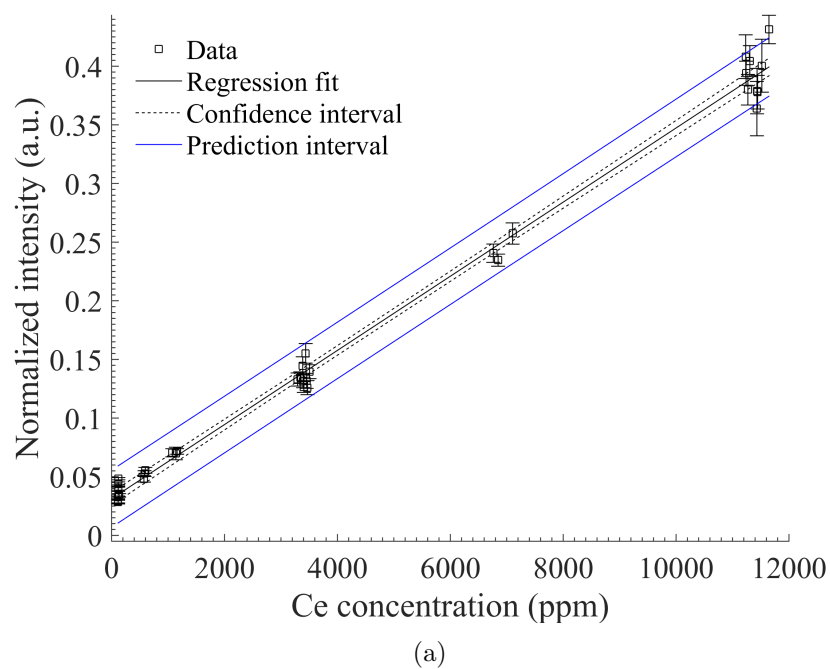
Figure 4.19: (a) The Ce curve generated using all 36 samples from the Ce 418.660 nm peak using intensity. (b) The Gd curve generated using all 36 samples from the Gd 409.861 nm peak using area.

Table 4.3: Tabulation of the R^2, b_1, b_0, and LOD for the Gd calibration curves.

374.347 nm (Area)	b_1	b_0	R^2	LOD
Low Ce	2.768e-06	-7.876e-04	0.992	211
Mid Ce	2.483e-06	-4.444e-04	0.994	307
High Ce	2.373e-06	7.192e-05	0.990	241
374.347 nm (Intensity)	b_1	b_0	R^2	LOD
Low Ce	2.457e-05	0.0104	0.993	134
Mid Ce	2.329e-05	0.0175	0.994	149
High Ce	2.255e-05	0.0300	0.990	181
404.986 nm (Area)	b_1	b_0	R^2	LOD
Low Ce	4.497e-06	-0.0013	0.994	106
Mid Ce	4.105e-06	-0.0011	0.993	147
High Ce	3.848e-06	-8.57e-04	0.993	340
404.986 nm (Intensity)	b_1	b_0	R^2	LOD
Low Ce	3.723e-05	0.0129	0.993	120
Mid Ce	3.411e-05	0.0284	0.986	124
High Ce	3.445e-05	0.0542	0.994	244
409.861 nm (Area)	b_1	b_0	R^2	LOD
Low Ce	4.964e-06	-6.632e-04	0.994	297
Mid Ce	4.706e-06	-8.593e-05	0.994	358
High Ce	4.516e-06	0.0014	0.993	350
409.861 nm (Intensity)	b_1	b_0	R^2	LOD
Low Ce	3.852e-05	0.0343	0.995	161
Mid Ce	3.732e-05	0.0459	0.992	164
High Ce	3.439e-05	0.0806	0.993	243

Table 4.4: Table showing the different values for the unknown sample generated using the combined Ce 418.660 nm peak and the Gd 409.861 nm peak.

Unknown Sample 1	Predicted (LIBS)	Actual (ICP-MS)	% Difference
ppm Ce	1401±501	1252±75	11.24
ppm Gd	10302±848	10203±500	0.96
Unknown Sample 2	Predicted (LIBS)	Actual (ICP-MS)	% Difference
ppm Ce	4548±488	5244±250	-14.22
ppm Gd	5312±832	6219±260	-15.73

ous samples perform well despite small variations as a result of the Low, Mid, and High concentration effects within the samples.

Multivariate Calibration Curves

The commercial package PLS_toolbox by Eigenvector Research was used to generate a partial least squares (PLS) model of the generated spectra. The 10 spectra from each sample were split into two groups (5 repetitions each) then averaged, one group is for calibration and the other for validation. In the PLS modeling, the entire spectra is used resulting a model that is more robust and is less prone to matrix effects. In the first phase of the modeling, the number of latent variables (LV) was selected in order to minimize the root mean squared error of cross validation (RMSECV). Here, the RMSECV is determined using venetian blinds within the calibration set. Figure 4.20 shows the that as the number of LV's increase, the RMSECV decreases rapidly at first and then levels off. The PLS_toolbox software recommended that 3 LV be used for this system since the first three values capture the majority of the system response. However, in order to further decrease the RMSECV, 7 LV were chosen for this model. The RMSECV for this condition is 406 ppm. Figure 4.21 shows the Ce calibration curve generated from 5 repetitions from each of the 36 samples. The calibration curve shows a very strong linear trend.

Next, the spectra that were not used in the calibration set were used to further validate the model. Figure 4.22 shows the predicted vs measured results. In this case, the model appears to predict the concentrations of Ce quite well. Figure 4.23(a) shows the residuals
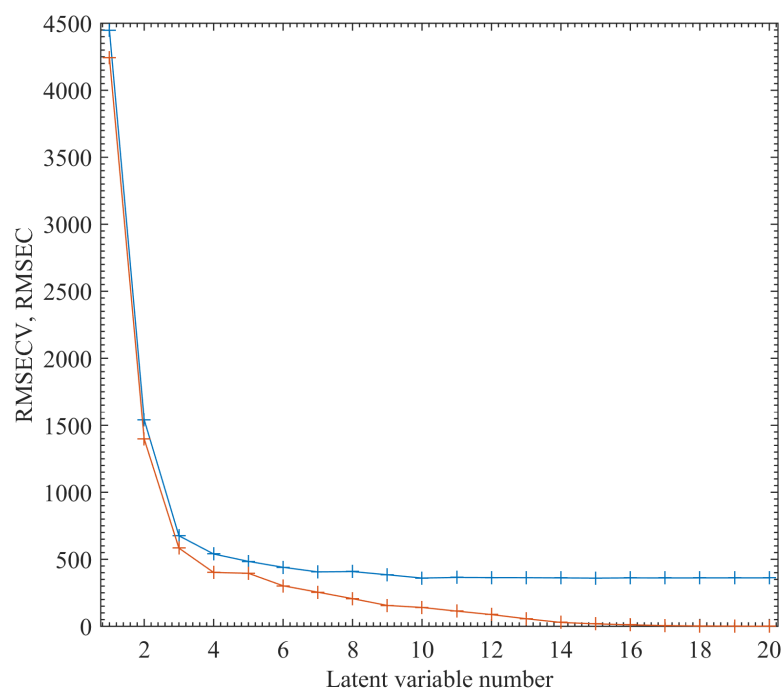
Figure 4.20: The number of latent variables as a function of the root mean squared error of cross validation (RMSECV).
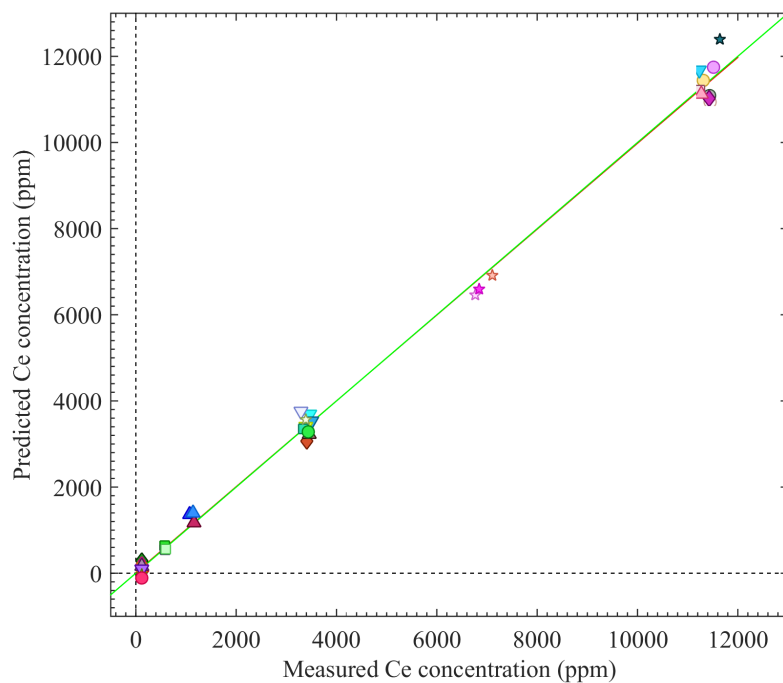

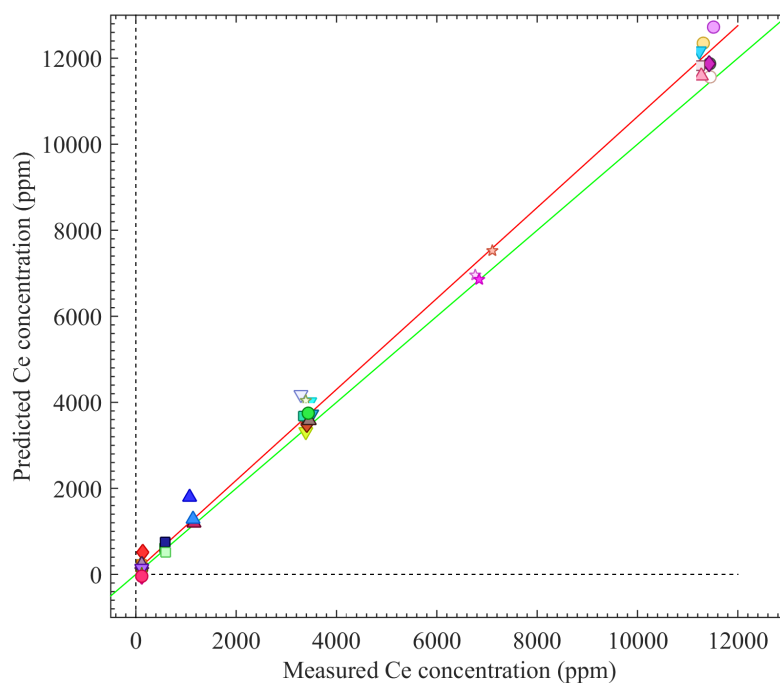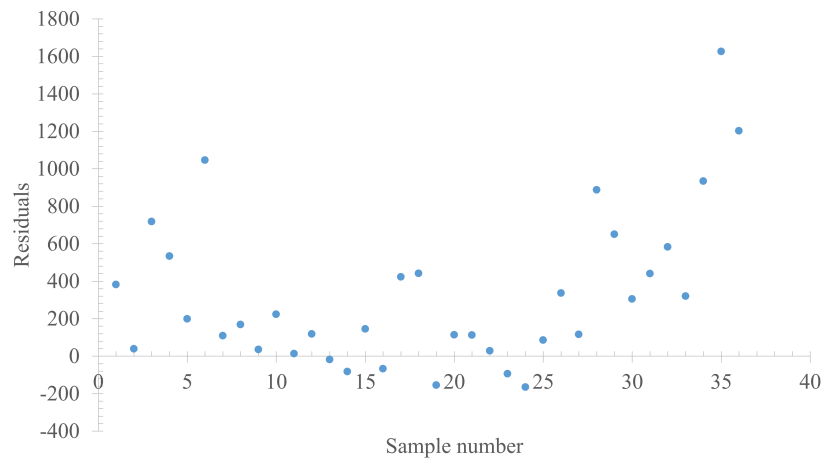Figure 4.21: Calibration curves for Ce generated from the PLS model.

Figure 4.22: The measured vs. predicted results of validation set.

between the measured and predicted results and Figure 4.23(b) shows the % error between the predicted and measured results. The largest % error are generated where the measured values are at the 100 ppm or 500 ppm levels where the residuals are low. Overall, the PLS model appears to perform well and is quite robust.

For Gd, a PLS model was generated as was done for Ce. The number of LV's was left at 8 as before since the trend was almost identical. However, in this case the RMSECV was 417 ppm. Figure 4.24 shows the calibration curve for Gd. Figure 4.25 shows the validation results. As in the Ce PLS modeling, the greatest % errors were for calculated for the 100 ppm and 500 ppm concentrations. Overall, the % error between the predicted and measured values was 10%.

The PLS models for Ce and Gd were applied to the unknown samples as was done with the univariate cases. Table 4.5 shows a comparison between the actual concentrations of the unknown samples and the predicted values based on the PLS model. The Ce concentration for unknown sample 1 shows the greatest variation from the actual value with a % difference

(a)
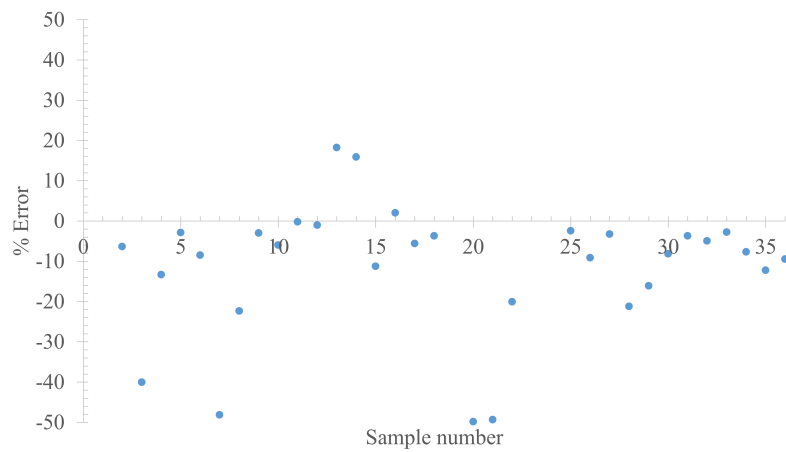
(b)

Figure 4.23: (a) Residuals between the predicted and measured results and (b) the % error for the validation set.
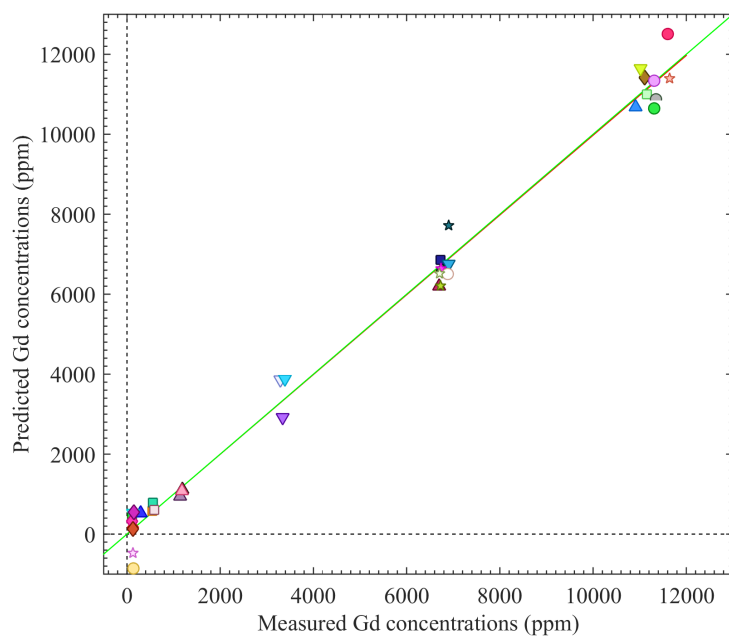
Figure 4.24: Calibration curves generated from the PLS model for Gd.
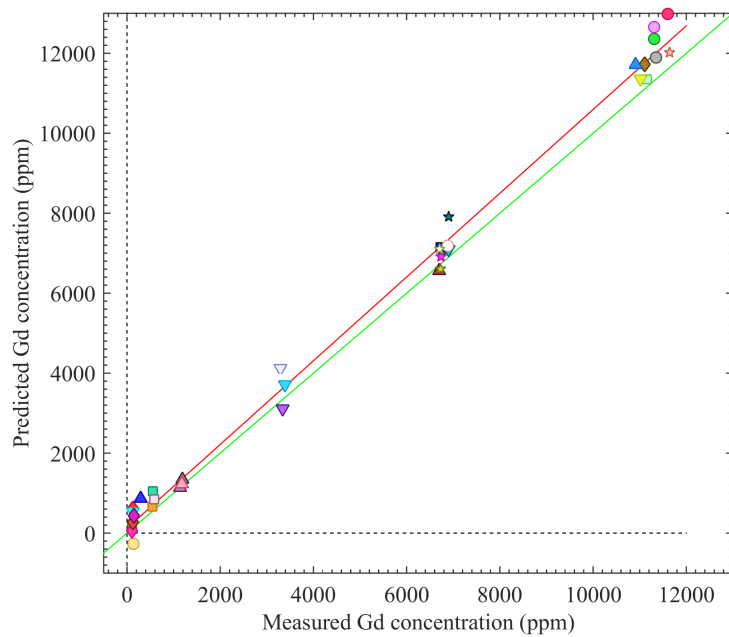

Figure 4.25: Validation generated from the PLS model for Gd.

Table 4.5: Predicted vs actual concentrations for the unknown samples. Predictions were done using the PLS models.

Unknown Sample 1	Predicted (ppm)	ICP-MS (ppm)	% Difference
ppm Ce	1,599 ± 425	1,252 ppm	24.3%
ppm Gd	10,547 ± 438	10,203 ppm	3.3%
Unknown Sample 2	Predicted (ppm)	ICP-MS (ppm)	% Difference
ppm Ce	4,992 ± 440	5,244 ppm	-0.5%
ppm Gd	5,961 ± 450	6,219 ppm	-4.2%

of 24.3%. However, The estimated error for the predicted value does barely fit within the actual concentration range. Despite the large variation for unknown sample 1 Ce concentration, the Gd for both samples and Ce for unknown sample 2 were very closely predicted. Interesting, both the univariate and multivariate models over predicted unknown sample 1 and under predicted unknown sample 2.

4.2.3 Conclusions

A novel molten salt aerosol system has been designed, built, and tested using an aqueous media. The main design incorporates a Collison nebulizer to generate the aerosol. The Collison nebulizer is an ideal candidate for this application due to its all stainless steel construction and reduced likelihood of material clogging. Other components such as the gas pre-heat, sampling chamber, filtration system, and gas cooling were described and key design features were determined.

In the initial design period, the system was tested at room temperature using an aqueous solution containing Ce, Gd, and Nd with concentrations ranging from 100 ppm to 10,000 ppm. The aerosol generated using the Collison nebulizer was bi-modal with a CMD of 1.4 μm and 4.2 μm. The %RSD between the 10 repetitions collected per sample averaged at 7.5%. Variation in the spectra can be contributed to fluctuations in laser energy, particle interaction, and small shifts in the position of the sampling chamber.

Several Ce and Gd lines from the spectra were analyzed to gain insights on the concentration effects between Ce and Gd. It was determined that for the Ce 418.660 nm peak there

was some interference as a result of a close Gd line. However, the peak intensity was not greatly effected. In addition, as a result of the high density of lines for Ce and Gd, even areas with no apparent lines were influenced as a result of an apparent background. The univariate calibration curves for the Ce and Gd lines were presented and the Ce 418.660 nm peak using peak intensity was determined to be the ideal peak for Ce analysis. In this cases, the R^2 is 0.992 and the LOD is 316 ppm. The ideal Gd line is the 409.861 nm line using peak area, in this case, the R^2 was 0.994 with a LOD of 189 ppm. Two unknown samples were analyzed using the above calibration curves and the sample concentrations were identified and compared to results obtained using ICP-MS. The LIBS analysis over predicted sample 1 by up to 11% and under predicted sample 2 by 15%.

In addition to the univariate analysis, a multivariate approach using PLS was done to generate calibration models. For these models, the 10 repetitions per sample were split to create calibration and validation data sets. the repetitions in each of the sets were averaged to provide 36 total sample points, each an average of 5 repetitions. The Ce PLS model used 7 latent variables and had a RMSECV of 406 ppm. The % error between for the validation was approximately 20%. The Gd model also used 7 LV and had a RMSECV of 417 ppm. The % error of calibration was approximately 10%. As in the univariate case, the PLS models were used to analyses the two unknown samples. The models over predicted sample 1 by up to 24% for the Ce case. The reason for this is currently unknown. Sample 2 was under predicted by 4.2% which is an improvement over the univariate case. Overall, the PLS models are more robust and yield better results.

Phase II of this work was completed with the successful testing of the aqueous aerosol-LIBS system. Results show the feasibility of the system and potential areas in the design that can be improved in the next phase of the work–such as the sampling chamber design and the system mounting mechanism.

5

Molten Salt System Design and CeCl$_3$ Testing (Phase III)

5.1 Molten Salt Experimental Design

5.1.1 Initial Design and Shakedown

Initial System Design

In the original aqueous design, the aerosol-gas stream entered directly from the 5/8 inch tubing of the Collison nebulizer into the sampling chamber where the LIBS plasma was formed in its center. As a result of this configuration, multiple particle interactions with the laser light occurred, which consequently, varied with respect to the plasma location and strength. To minimize this effect, a new sampling chamber was designed in which the optical windows were centered at the top of the 5/8 inch aerosol input stream. As a result, the plasma formation could be positioned at the top surface of the stream while still having the plasma centered with respect to the light collection windows. The intent with this design was to reduce the number of particles interacting with the laser, thus reducing the variation in the plasma location. The new sampling chamber also used 3/8 NPT sight glass windows;

however, rather than plain glass windows, a quartz window with a 0.24 inch optical port was used. From the aqueous study, the pressure within the sampling chamber did not change, as a result, in the new sampling chamber design, only one port was added to measure the temperature.

Prior to molten salt experiments, the seals in the nebulizer, sampling chamber, and coalesce filter needed to be changed in order to operate at high temperatures. All of the threaded joints were sealed using Deacon 770-L, which is a high temperature (up to 500°C) thread sealant. As this product was being cured, it would release CO_2 and CO off-gases. In order to prevent contamination within the glovebox, the seals were cured at 200°C in the fume hood prior to installation. The coalesce filter was fitted with flexatalic seals provided by United Filtration Systems, Inc. The main seal between the nebulizer and the jar was made using a graphite impregnated cord that was cut to size and fitted into the o-ring grove. The system was pressure-tested offering a leak free system up to 40 psi, at which point a small leak developed between the jar and the nebulizer.

In Chapter 4, the heating requirements and components for the gas pre-heat and salt melting furnaces were addressed at the maximum assumed gas flow rate of 20 L/min. From the aqueous experiments, it was apparent that these flow rates were not achievable or desirable with the Ar carrier gas. Originally, it was assumed that at a high gas flow rate, the temperature drop in the gas stream from the gas pre-heat to the nebulizer would be small. However, initial testing of the system at the operating temperature and typical flow rates showed that the gas temperature, as measured at the top of the nebulizer, was only 130°C. This temperature was obtained via a 1/8 inch diameter stainless steel sheathed thermocouple that had been inserted into the nebulizer feed line. To ensure the gas would not freeze the salt in the nebulizer, a 0.5 inch by 24 inch heating tape was coiled around the gas tubing leading from the gas heater to the melt furnace. This heating tape was controlled at 500°C. In addition, two cartridge heaters were added, one into the sampling chamber and the other to the coalesce filter. Each cartridge heater (125 W) was operated at 500°C.

Figure 5.1: Initial high temperature aerosol-LIBS configuration with insulation and heating.

The next major modification was to fit the entire system with insulation. This proved to be rather challenging due to several constraints: (1) it needed to be easily removable, or at least allow for the disassembly of components for cleaning, (2) it needed to be relatively dust free, and (3) it needed to be able to withstand the high temperature requirements without being too bulky. Several different configurations were explored. However, in the final design, two rigid disc of insulation lined with a stainless steel mesh were used to top the melt furnace. The stainless steel was placed to provide structural support as well as dust control. The tubing, sampling chamber, and coalesce filter were first wrapped in a half inch thick ceramic blanket before being covered with an insulation repair wrap that solidifies into a hard casing material. This repair wrap supported the insulation structurally and reduced dust formation. The completed setup with all the insulation in place is shown in Figure 5.1.

Just prior to closing off and sealing the glovebox, a 4 m fiber optic cable from Ocean Optics was passed through a port in the wall of the glovebox and sealed using a cord grip and epoxy. Following this, the glovebox was sealed and the inert atmosphere was established prior to operating with molten salts.

64

Shakedown Testing and Optimization

For the initial testing, 41.5 g of salt at 5 wt% $CeCl_3$ in a eutectic LiCl-KCl was used. Optimization was done using a signal-to-background ratio (SBR) which is the peak intensity divided by the background near the peak of interest. This is a fast and simple approach for optimization. For each parameter explored, three different repetitions of 250 shots each were taken and averaged to provide a representative spectrum.

During the first experiment, it was observed that the plasma location shifted slightly as observed before with the aqueous case. In addition, small bright spots, presumably droplets in the laser path were observed. As a result of this observation, it is apparent that the aerosol gas stream was mixing into the entire sampling chamber volume and particle interaction with the laser was distorting the plasma formation as was observed in the aqueous case.

In order to better understand the nebulizer operation, the nebulizer gas pressure was explored at a laser energy of 65±5 mJ. Since there was no pressure measurement at the sampling chamber itself, the differential pressure between the nebulizer and sampling chamber is unknown. However, it was observed that as the gas pressure prior to the nebulizer increases from 10 psi to 60 psi, the flow rate of the aerosol-gas stream increases from 0.63 L/min to 1.5 L/min, respectively. These flow rates were significantly lower than anticipated flow rates in the initial design. The SBR as a function of the pressure is shown in Figure 5.2 for a 3-jet nebulizer for the 418.660 nm, 428.999 nm, and 457.228 nm lines. The LIBS signal decreases significantly with increased pressure. This may be a result of increased particle interference with higher pressures. Below approximately 10 psi, the nebulizer becomes unstable. As a result, a gas operating pressure of 10 to 15 psi was determined to be optimal.

Following this first test, a pressure gauge was placed in the temperature port of the sampling chamber and the pressure drop for the above pressures was recorded to be approximately 1.5 psi to 2 psi across the pressure range studied. Figure 5.3 shows the SBR as a function of the laser energy used while operating at a gas pressure of 10 psi. The results show that the SBR increases linearly up to about 90 mJ where the trend reaches its asymptotic
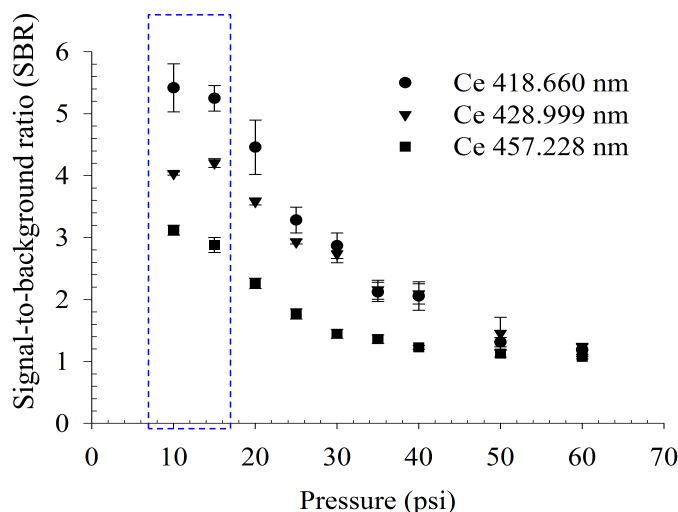
Figure 5.2: The SBR as a function of the argon gas pressure in a 3-jet nebulizer.

value. Laser energies beyond 140 mJ were not studied, but it is anticipated that the SBR plateau would eventually drop off to lower values. Interestingly, the %RSD between the three repetitions dropped with respect to the laser energy from 10% to 4.5% from the 40 mJ case to the 140 mJ case, respectively. This is partially a result of a more stable laser at higher energies. In most cases the goal is to maximize the SBR when optimizing; however, in order to operate at a safer, less energy intensive range for the laser, a different approach was used. In this case, the intersection between the upward slope and the plateau was identified as the optimal value since it provides the lowest laser energy while still achieving high SBR's. As a result, 90 mJ was selected.

Following this first test, salt droplets were observed between the nebulizer lid and the jar, indicating that the seal had failed. Of the 41.5 g of salt added, only 35 g of material were recovered from the nebulizer jar and system components. There are several potential explanations for the missing material, (1) it leaked through the nebulizer seal and was deposited into the furnace, (2) it deposited in the tubing or heat exchanger prior to the HEPA filter, or (3) salt droplets were small enough that they were trapped in the gas stream and passed through the HEPA filter and into the exhaust system. More likely, all three
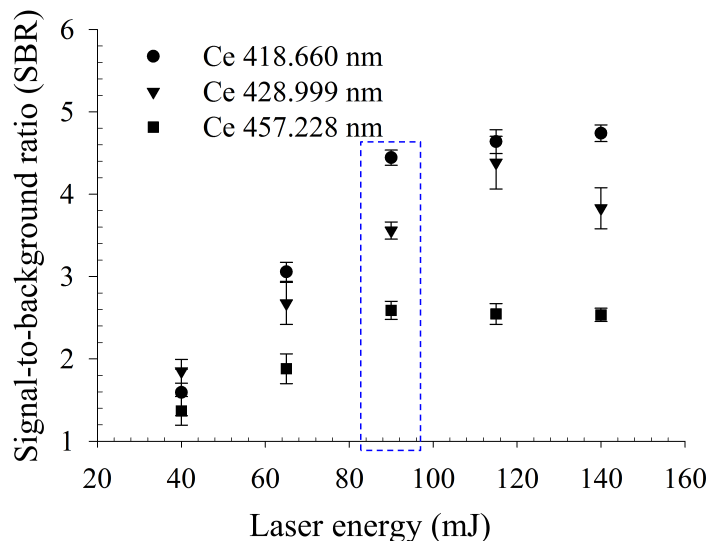
66

Figure 5.3: Optimization of the laser energy.

scenarios played a part in the missing material. In addition to these observations, it was noted that there was only a small gap (0.085 inch) between the bottom of the nebulizer tip and the bottom of the jar, this could decrease the flow of the fluid being drawn into the gas jet.

As a result of the first test done in molten salt, several modifications to the system were done to improve performance. First, a new nebulizer shaft was installed in order to increase the distance between the nebulizer tip and the bottom of the jar. Secondly, a 0.5 μm coalesce filter was used in place of the 1.0 μm filter. The hope in these modifications was to create better flow characteristics in the system and to reduce the amount of missing material per run. To prevent salt leaking around the nebulizer seal, methods were explored to improve the graphite cord placement and it was determined that placing the square cord flat across the o-ring groove provided the best results.

In the next shakedown test at 3 wt% $CeCl_3$, the modifications to the aerosol-LIBS system as well as a 1-jet nebulizer tip were explored as a function of the carrier gas pressure. The geometry of the nebulizer tip is exactly the same but with two fewer jets than the 3-jet case. One effect of fewer jets is that the gas flow rate and salt consumption in the nebulizer jar is
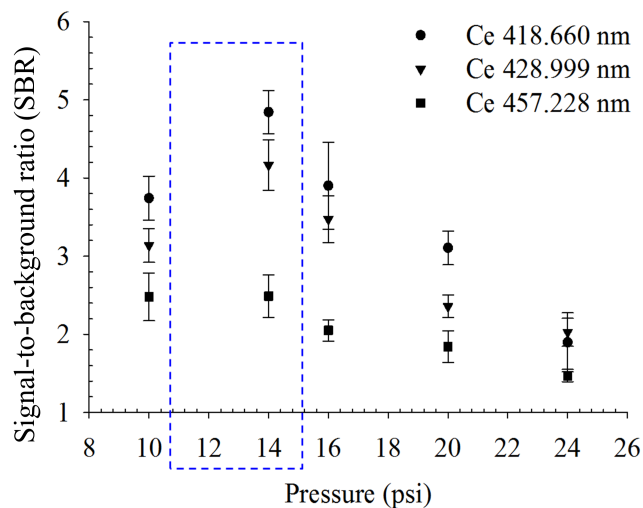
Figure 5.4: SNR as a function of the nebulizer gas pressure for a 1-jet system.

approximately 2/3 less. This allows for a LIBS measurement while consuming less material. Results for this study are shown in Figure 5.4. Here, the SBR has a maximum between 10 and 15 psi. The signal at 10 psi is significantly lower than at 14 psi which is different from the observation made with the 3-jet system. When the 1-jet and 3-jet systems were compared directly as is shown in Figure 5.5, the 1-jet system has a lower signal in general. The exact reason for this is unknown since several modifications to the system were done prior to this test. However, at approximately 15 psi the variation between the two systems is not large. The %RSD's for the different pressures were 13.3%, 6.6%, 30%, 9.3%, and 9.9%, for the 10, 14, 16, 20, and 24 psi pressures, respectively. As a result of increased signal and a reduction on the %RSD's, approximately 14 psi is the optimal pressure for the 1-jet system.

With the addition of the 0.5 μm filter, the pressure drop across the filter increased significantly. For the highest pressure recorded (24 psi), the pressure at the gauge was 30 psi with a 6 psi pressure drop across the filter. The 6 psi pressure in the jar and sampling chamber region increased salt leaking through the nebulizer main seal. However, all but 1 g of the added material was recovered following the experiment.
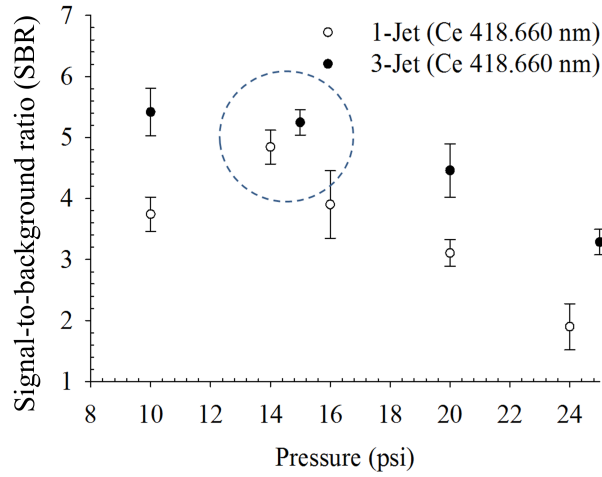
Figure 5.5: Comparison between the 3-jet and 1-jet nebulizer systems as a function of gas pressure.

Near the end of this second experiment, the heat tape used to heat the length of tubing between the gas pre-heat and the nebulizer failed. This is a common problem with heat tape as a result of hot spots due to poor contact between the heating element and the tubing. After this failure, the temperature at the location of the thermocouple located at the gas inlet of the nebulizer dropped to 130°C. As a result, the signal decreased slightly, but the system continued to function well overall. Because the heat tape is prone to failure, and replacing the heat tape within the glovebox is challenging, this heating element was omitted from the system.

Several observations were made about the aerosol-LIBS system following these initial shakedown tests: (1) the quartz windows had developed a thin film or etch that needed to be removed in order to maintain a good optical path, (2) the Deacon 770-L seal material at 500°C continued to off gas and eventually disappeared, thus leading to increased leaking of threaded joints and increased oxide formation and corrosion, (3) the system needed to be more easily disassembled for cleaning between runs, and (4) increased filtration was needed to prevent the loss of material. For these reasons along with the continued particle interaction with the laser, it was deemed necessary to make additional modifications to the aerosol-LIBS
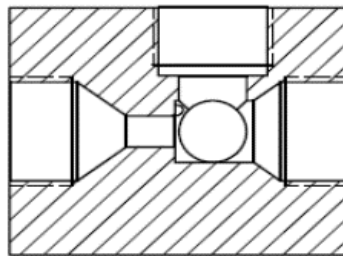
69

Figure 5.6: Cross section of the improved sampling chamber design.
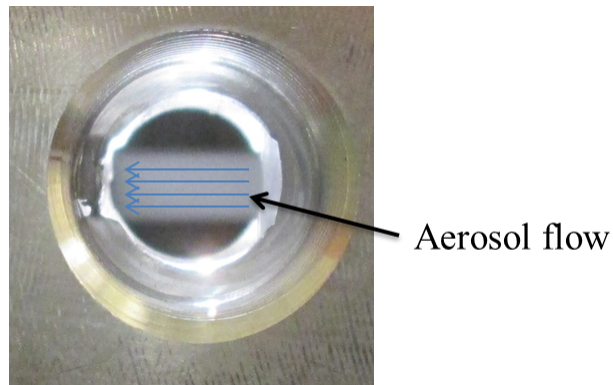
design.

5.1.2 Final System Design

The main modification to the system was made to the sampling chamber. Figure 5.6 shows a cross section of the new design. In this case, the NPT fitting connecting the sampling chamber to the nebulizer and to the coalesce filter were replaced with a welded joint. The aerosol-gas stream passes through a sudden expansion to create a jet which expands after it has passed through the sampling chamber into the exit region. As a result of this flow, significantly fewer particles are expected to fill the sampling chamber volume. The nozzle design was compared with the previous sampling chamber design using an aqueous system with LED lighting. Figure 5.7(a) shows the flow through the old sampling chamber. As a result of the design, the aerosol-gas stream expanded into the chamber and was sheared off at the exit which created eddies. Figure 5.7(b) shows the nozzle design under the same conditions. In this case, the flow was significantly more stable. In these tests, the windows were not in place in order to better visualize the phenomenon, as a result, the actual flow within the chamber is likely different. However, this example illustrates the advantage of the modified design.

Another change to the sampling chamber was in relation to the optical windows. A 1/2 NPT sight glass window from TATE-JONES Inc, was identified that uses a 0.75 inch quartz window insert sandwiched between grafoil seals which are compressed to form a seal by a threaded nut. In order to streamline the sampling chamber and to the eliminate the

Vortex

Main aerosol-gas
stream flow

(a)

Aerosol flow
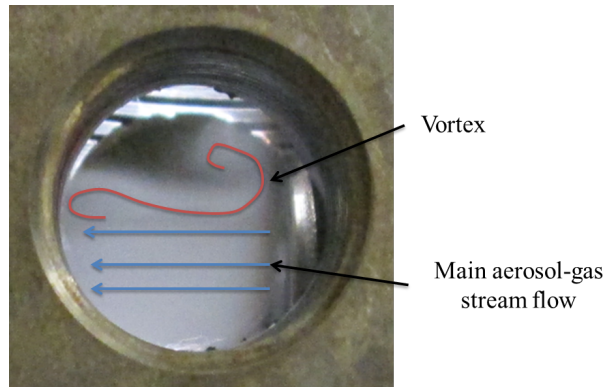
(b)

Figure 5.7: (a) Aqueous test of the old sampling chamber design and (b) the aqueous test done using the sudden expansion.

NPT thread, the same dimensions for the optical pocket housed on the NPT sight window was built into the sampling chamber itself. With this design, grafoil seals and replacement windows could be easily installed into the sampling chamber. This design offered several key advantages: (1) the windows did not extrude out of the chamber and thus insulation was more easily added and removed between experiments without significant dust formation and (2) the windows could easily be replaced/cleaned after every experiment. Here, sapphire windows of the same dimensions were purchased from Meller-Optics and were used in place of the quartz windows.

The modifications to the sampling chamber design itself should reduce particle interaction; however, in addition to those changes, a 3X beam expander was set up using a -25 mm plano-concave lens and a 50 mm plano-convex lens. Expanding out the laser reduces the impact that a single droplet will have on the overall energy as well as decreases the likelihood of a premature breakdown. This should reduce the shift in the plasma location from shot-to-shot.

In order to reduce the leaking of the nebulizer lid and jar, a custom grafoil seal of 1.90 inch inside diameter by 2.11 inch outside diameter by 1/8 inch thick were purchased from Industrial Packing and Seal, Inc. Prior to use, these seals were held at 500°C for 6 hours to out-gas any impurities possibly contained in the material. The threaded joint between the nebulizer shaft and tip was sealed using a fine sliver from the graphite impregnated cord that was approximately 10 inches long. This fine graphite cord was wrapped around the threads prior to attaching the nebulizer tip. In this way, the graphite cord was smashed between the threads and in the o-ring groove, creating a solid seal.

To address the issue of material loss, an additional filter from United Filtration Inc, was purchased and placed in series with the first filter. The first filter in the series was the 1.0 μm filter and acts as a coalesce filter to remove the molten droplets from the gas stream. The second filter was a 0.5 μm filter and was set to capture particles after they had frozen. In addition to this change, the gas cooling heat exchanger which would be needed if operating
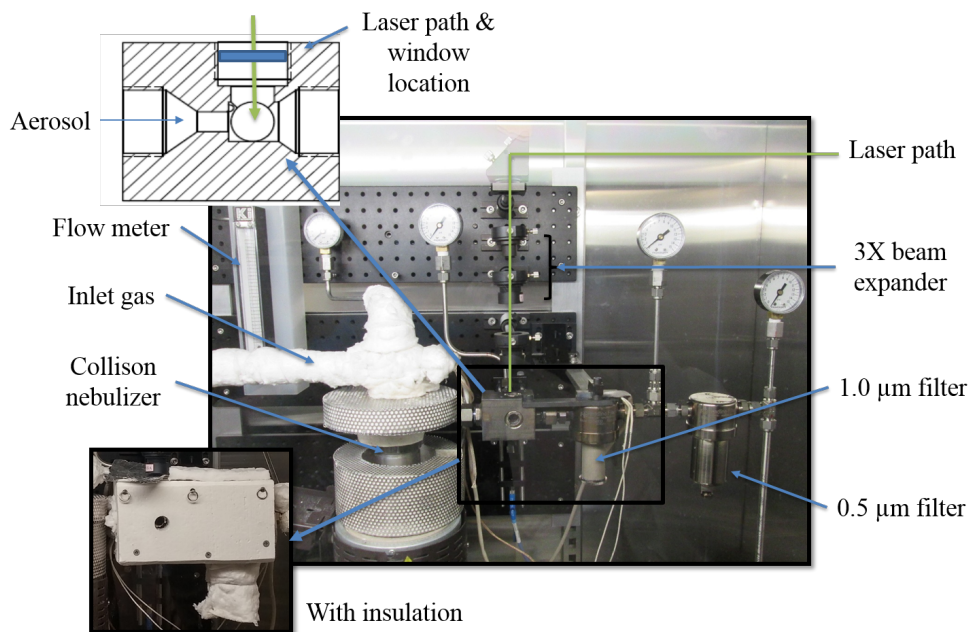
Figure 5.8: Photo of the final molten salt aerosol-LIBS design.

at 20 L/min was removed from the system because the actual flow rates were significantly less (0.3 to 1.5 L/min) and enhanced cooling was unnecessary. In the removal of the heat exchanger, a large quantity of salt was found deposited in the tubing from the previous experiments.

Most of the insulation used in the previous design was maintained. However, in this design, the insulation surrounding the sampling chamber and the 1.0 μm filter was constructed of 1 inch think alumina silicate insulation board that had been constructed to form a box. Placement and removal of the insulation was easily accomplished using 4 inch stainless steel pins. The lid of the box was placed on top of the sampling chamber and the insulation box was slid up around the sampling chamber and held with the pins. To reduce dust formation, stainless steel mesh was placed on the inside surfaces of the box. Small gaps in the insulation box were filled with alumina silicate fibers. Figure 5.8 shows a picture of the final design of the aerosol-LIBS system complete with the insulation box described above.

73

5.2   Molten Salt Cerium Experiments

5.2.1   Material and Methods

Molten salt experiments using $CeCl_3$ as a surrogate material were done in a LiCl-KCl eutectic salt to test the final aerosol-LIBS design. Salt samples were made using $CeCl_3$ (99.99%), LiCl (99.99%), and KCl (99.95%) purchased from Alfa Aesar. The LiCl and KCl salts were mixed at the eutectic ratio (44 wt% LiCl and 56 wt% KCl) and the $CeCl_3$ composition was varied from 0 wt% to 5 wt%. Salts were prepared in the inert atmosphere glovebox by first mixing the LiCl and KCl beads together and allowing them to dry at 300°C for 2 to 12 hours in a stainless steel crucible. Following drying, the furnace was ramped up to 500°C to melt the salt for 1 hour before it was removed and allowed to freeze. The $CeCl_3$ was then added to the top of the frozen LiCl-KCl salt and then remelted for at least 3 hours to ensure a homogeneous mixture. To reduce the amount of salt required overall, only 30 g of total salt per experiment was used. The solid salt ingot was crushed using a pair of wire cutters and the salt chunks were loaded into the sealed nebulizer through the spout.

In these experiments, a Q-smart 450 Nd:YAG laser (Quantel USA, Inc.) was mounted vertically on the outside of the glovebox and the laser light was directed via optics into the glovebox through a quartz window located in the glovebox wall. The laser was operated in the 532 nm wavelength mode. A laser mirror within the glovebox directed the laser light downwards through a 3X beam expander and finally through a 75 mm focal lens into the sampling chamber. The focused laser light created a plasma in the center of the sampling chamber. Light from the plasma was collected via an f = 75 mm lens and then focused (f = 100 mm lens) into a 4 m long fiber optic cable from Ocean Optics, Inc. The fiber optic cable carried the light to a Michelle 5000 spectrometer and iStar ICCD detector (Andor Technologies, Inc.) located outside of the glovebox.

Throughout operation of the aerosol-LIBS system, the pressure drop across the 1.0 μm filter increased initially to approximately 4-5 psi as a steady state condition (typically after

Table 5.1: Operating temperatures of the different components in the Aerosol-LIBS system.

Gas pre-heat furnace	550°C
Gas inlet of the nebulizer	130°C
Salt in the nebulizer	470°C
Sampling chamber	260°C
1.0 μm filter	500°C
0.5 μm filter	60°C

10 minutes). The nebulizer operation was controlled by adjusting the input pressure in order to maintain a 12 psi pressure differential between the nebulizer input and sampling chamber. The operating temperatures of the system are shown Table 5.1. The laser energy used was 50 mJ. This is significantly lower than the 90 mJ shown to be optimal, and the reason for this is due to damage thresholds of the optics used in the 3X beam expander.

In the first set of experiments, the gate delay was studied between 100 ns and 25 μs. For each variation, 3 repetitions were completed, each comprised of 250 laser shots at 2 Hz. The gate width was 300 μs. The 250 spectra from each repetition were averaged to provide a single representative spectrum. Following the optimization test, experiments were conducted to generate calibration curves for $CeCl_3$. In this series of experiments, 300 shots were recorded and averaged over 7 repetitions. A summary of the experiments conducted is shown in Table 5.2. The experiments are named MS#, where MS stands for Molten Salt. The first three experiments were done in the initial testing and shakedown period as described above. In experiment MS7, a new optical port configuration was tested that yielded low intensities and poor %RSD's. As a result, MS7 was not included in this study. Experiment MS13 was also not included because there was significant oxide formation and the spectral results and carrier gas flow were unreliably low even with normalization. Two sets of data were collected for MS14, the first was collected in the first hour of running and the second after 5 hours of running.

Following each experiment, the system was disassembled and all of the salt deposited on the different surfaces was scraped free and recovered. All of the recovered salt mass and system components were weighed for material accountancy. With the addition of the

Table 5.2: Table of the different Molten salt experiments conducted at different wt% of $CeCl_3$.

Experiment number	wt% $CeCl_3$	Date conducted
MS4	3.0	March 25, 2016
MS5	3.0	April 5, 2016
MS6	0	May 10, 2016
MS8	0.1	June 2, 2016
MS9	0.5	June 4, 2016
MS10	1.0	June 7, 2016
MS11	1.0	June 16, 2016
MS12	3.0	June 24, 2016
MS14	5.0	July 1, 2016

second filter, typically all but 0.25 g of material could be accounted for. This amount, is likely contained in the larger stainless steel components as a surface film which is difficult to remove via scraping. The large components could not be weighed with enough precision to account for this salt. The salt recovered in the different locations was reserved for ICP-MS analysis. After the different components were scraped of salt, they were washed in nano pure water and dried in acetone. In addition, the sapphire windows were removed following each experiment and washed with nano-pure water and acetone.

Salt samples reserved for from the various locations within the aerosol-LIBS system were prepared for ICP-MS analysis. Samples were made by weighing out between 0.01 and 0.03 g of salt and dissolving it into 10 mL of 2 % nitric acid for at least 2 hours. Following dissolution, samples were diluted between 500X and 1000X in order to get the Li concentration in the solution to below 500 μg/L. Prepared samples were run using an Agilent 7900 ICP-MS instrument from Agilent Technologies.

5.2.2 Results and Discussions

Experiments were conducted to explore the spectral decay with respect to the gate delay of the spectrometer. In the first experiment, the gate delay was varied from 100 ns to 9 μs. This range was expected to yield the optimal gate delay; however, results indicated that perhaps
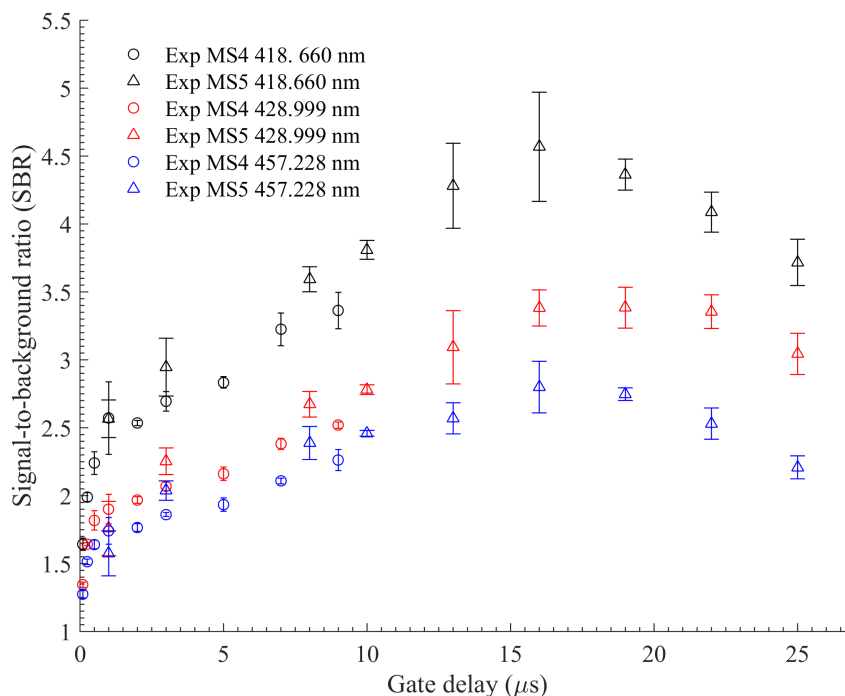
Figure 5.9: Optimization of the gate delay with respect to the SBR.

a larger gate delay was necessary. Consequently, a second experiment was conducted ranging the gate delay from 1 μs to 25 μs. Results from the two gate delay experiments done at 3 wt% CeCl$_3$ are shown in Figure 5.9. As the gate delay increases, the SBR increases until 16 μs and then slowly decreases. As a result, 16 μs was selected as the optimal value.

A representative spectrum obtained from the molten salt aerosol-LIBS system is shown in Figure 5.10. Here, the Li and K peaks can be easily identified along with multiple Ar peaks (not marked in the Figure). Notable cerium peaks are the Ce 418.660 nm, Ce 428.990 nm, and the Ce 457.228 nm lines. These lines were selected using the NIST database due to their intensity and low interference with other lines.

As a result of the modifications made to the aerosol-LIBS design, the plasma location varied less and fewer particle interactions were observed. The repeatability of the system is shown in Figure 5.11. The variation between repetitions is small as observed in Figure 5.11(a) and the %RSD's are on average 4.8% as shown in Figure 5.11(b). This is a slight improvement
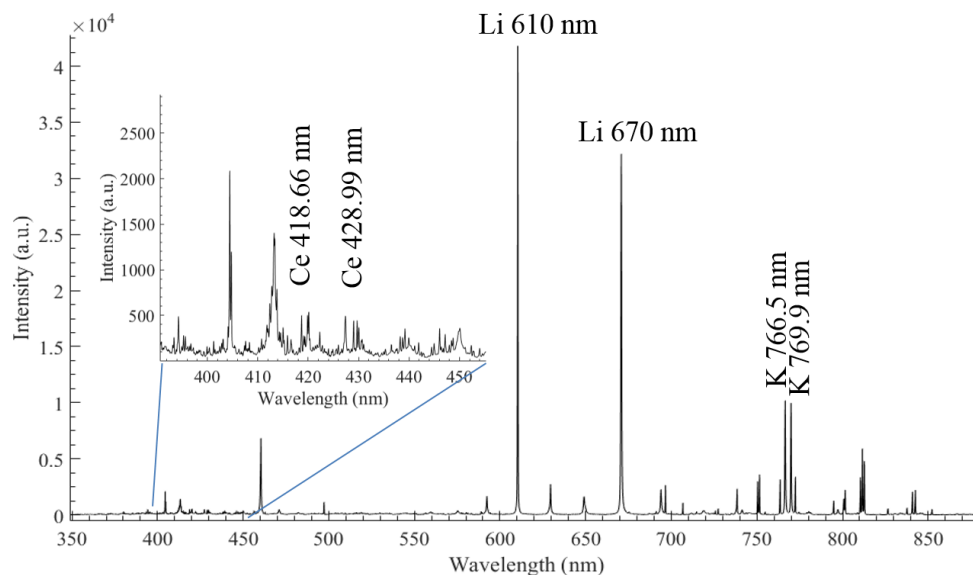
Figure 5.10: A representative spectrum collected in the 3 wt% $CeCl_3$-LiCl-KCl salt at a 16 μs gate delay.

over the previous design. As a result of the new design, it is anticipated that the largest source of variation in the system comes from fluctuations in the laser energy. Indeed, Figure 5.12 shows the laser energy fluctuation with respect to the shot number. There is approximately 10% variation from shot to shot; however, there is also a large sinusoidal oscillation with a period of 150 shots. To reduce variation as a result of the oscillation, two periods or 300 shots were used in this study.

Next, the repeatability of the system over time was explored. Figure 5.13(a) shows the signal response over time. It is clear that the overall intensity of the spectra decreased with time. This is due to degradation of the optical setup as a result of dust, insulation off-gas, and vibrations. The surface films on the optics were removed periodically; however, some loss in signal resulted over time. Figure 5.13(b) shows the %RSD over time between the different experiments. This illustrates that the signal loss was across the entire spectrum. The high %RSD values between 300 and 500 nm make sense due to the change in the Ce concentrations. For this study to have value, a normalization method is needed. For application of the aerosol-LIBS technique to measure molten salts in the electrorefiner, a
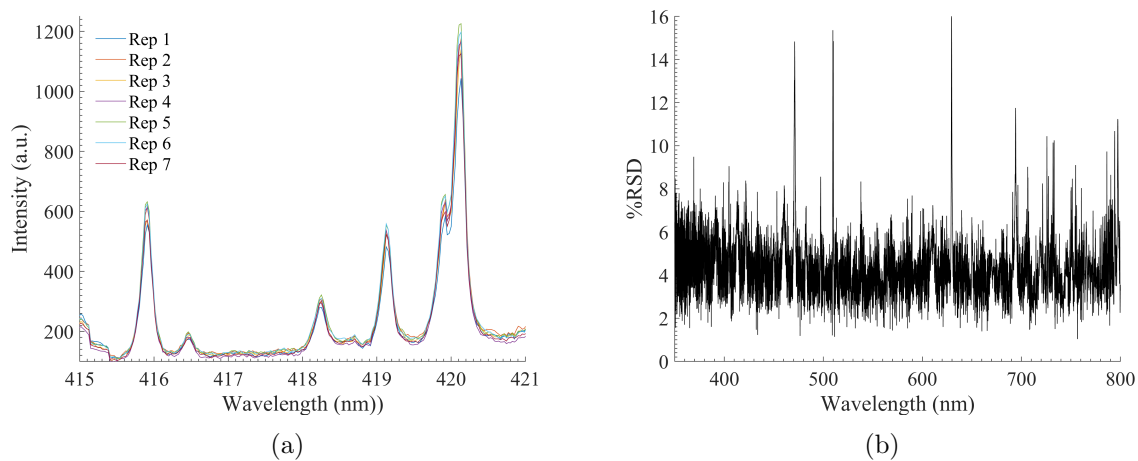
Figure 5.11: (a) Spectra near the 418.660 nm line at 0.1 wt% CeCl$_3$ (b) the %RSD between the 7 repetitions studied with no normalization.
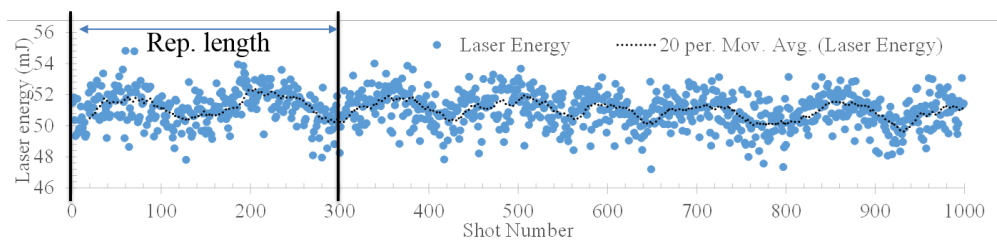

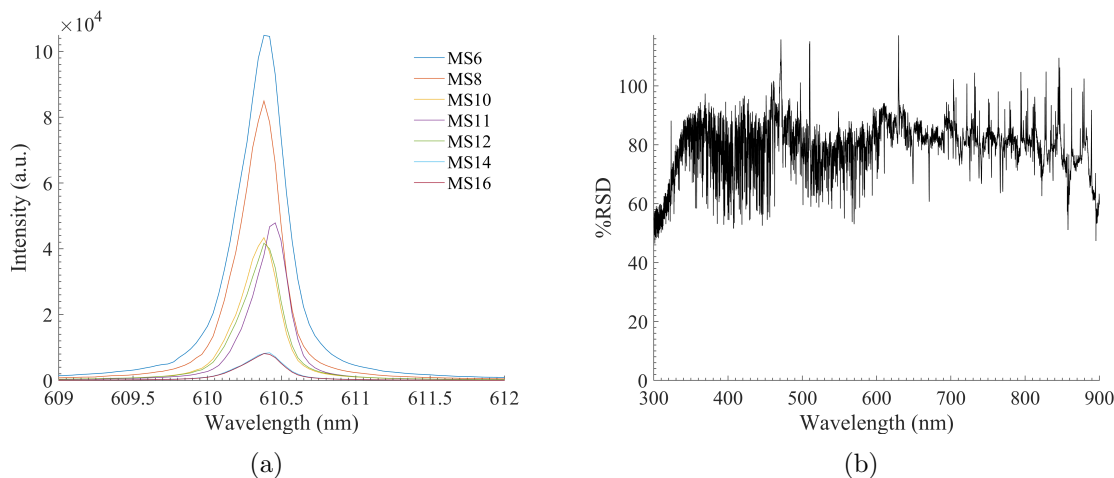Figure 5.12: The laser energy as a function of the shot number.

Figure 5.13: (a) The Li 610.3 nm line for the different experiments run over a period of 3 months and (b) the %RSD between the experiments over time.

method is needed to reduce the degradation effect of the optics. This may require the periodic replacement of optical components or a gas protective layer between the system and the optics.

Elements in the sample that are candidates to use for normalization are Li and K since they are present in large quantity and their concentrations do not change significantly from experiment to experiment. The K peaks at 766.5 and 769.9 nm can be used; however, Hanson et. al[13] reported that the K lines are prone to self absorption. As a result, Li will be used as an internal standard in order to normalize the spectra. In this case, each individual spectra was divided by the averaged intensity from 459 nm to 461 nm. This wavelength range covers the Li 460 nm peak. Figure 5.14 shows the normalized spectra and %RSD's for the experiments. The spectra still had high %RSD's where the majority of the Ce lines were as a result of the varying concentrations; however, the region between 600 nm to 900 nm had significantly reduced %RSD's.

Results from the ICP-MS analysis are shown in Table 5.3. In many instances, little to no material could be obtained for ICP-MS analysis and thus, concentration data at these points was not obtained. The bulk measurement came from the nebulizer jar following
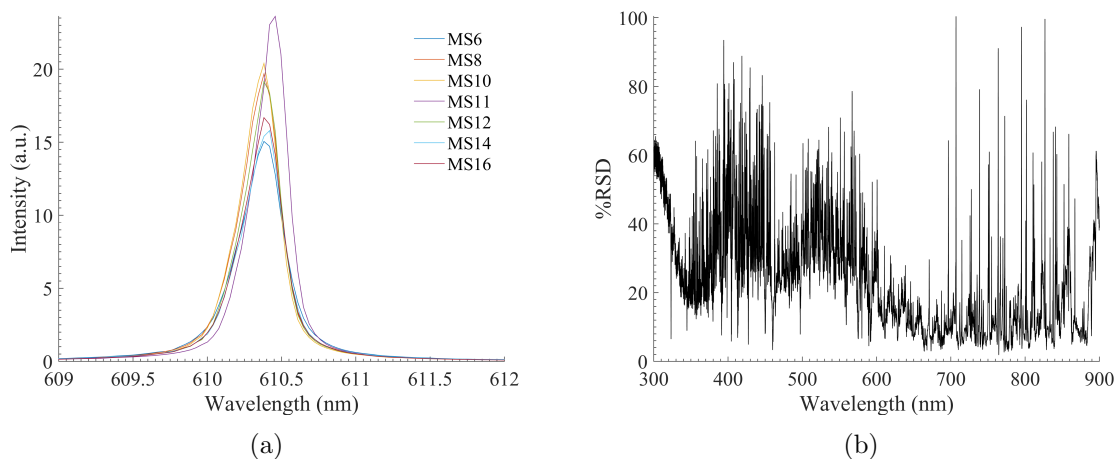
80

Figure 5.14: (a) The normalized Li 610.3 nm line for the different experiments run over a period of 3 months and (b) the %RSD between the normalized experiments over time.

Table 5.3: ICP-MS results from the Ce molten salt experiments, n/a values were not collected or no materials were available from the system for testing.

Experiment #	Bulk (wt% Ce)	Sampling Chamber (wt% Ce)	1.0 μm Filter (wt% Ce)	0.5 μm Filter (wt% Ce)
MS5	1.676	n/a	n/a	n/a
MS6	0.0004	n/a	0.004	n/a
MS8	0.0315	n/a	0.0065	n/a
MS9	0.2245	n/a	0.1195	n/a
MS10	0.500	n/a	0.2625	n/a
MS11	0.450	0.489	n/a	n/a
MS12	1.612	1.484	1.277	n/a
MS14	2.637	2.589	2.330	2.605

the experiment. The sampling chamber and filter measurements were scraped from these respective components. Of the data collected, the general trend is that the concentration of Ce drops slightly throughout the system. In other words, the further the aerosol travels from the nebulizer, the lower the concentration of Ce in the aerosol stream.

Spectra from each experimental repetition were analyzed using the MATLAB GUI that was developed for the aqueous work. In this case, the Ce spectral lines at 418.660 nm, 428.990 nm, and 457.228 nm were used. Figures 5.15, 5.16, and 5.17 show the calibration curves generated from the peak areas. Concentrations shown in the curves were obtained from the
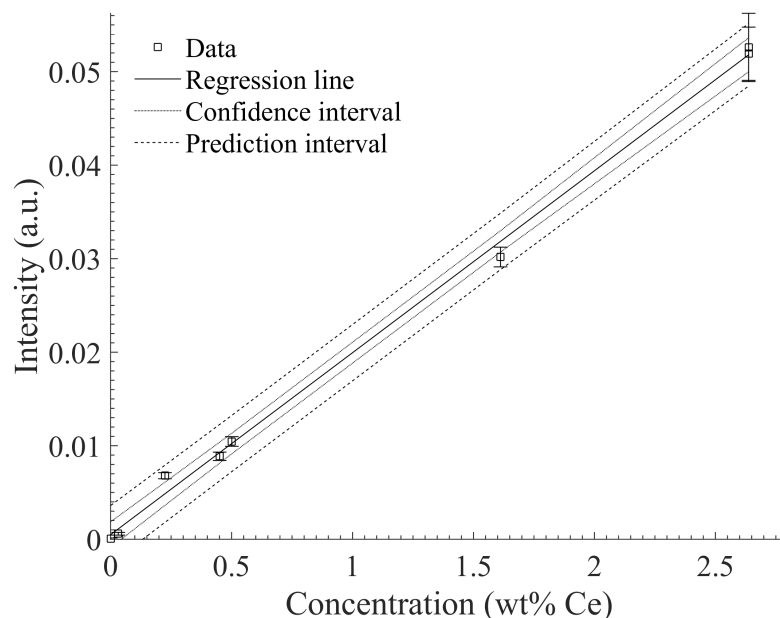
Figure 5.15: Calibration curve calculated from the Ce 418.660 nm line in molten salt.

Table 5.4: Regression curve fits and LOD for the univariate calibration curves for Ce in molten salt.

Peak (nm)	R^2	b_1	b_0	LOD (wt% Ce)	LOD (ppm)
418.660	0.9976	0.0194	0.00049	0.0504	504
428.990	0.9975	0.0133	0.00208	0.1316	1316
457.228	0.9938	0.0099	0.00085	0.1999	1999

ICP-MS bulk measurements. For the Ce 418.660 nm line, all of the experimental data points line up to form a strong linear trend with the exception of MS9 at 0.22 wt% Ce. This point is above the regression line for all three Ce peaks selected. Under closer investigation, MS9 was run at a slightly higher energy range (55-60 mJ), as a result, this point shows a slightly higher intensity response despite normalization. The R^2 values, regression fits, and LOD for the three curves are shown in Table 5.4. The 418.660 nm and 428.999 nm lines have similar R^2 values; however, the slope for the 418.660 nm line is steeper which indicates that this line has a greater sensitivity to the Ce concentration. As a result, the Ce 418.660 nm line has the best LOD down to 504 ppm. The Ce 457.228 has the worst R^2 value as well as the poorest sensitivity–leading to a poor LOD of 1999 ppm.
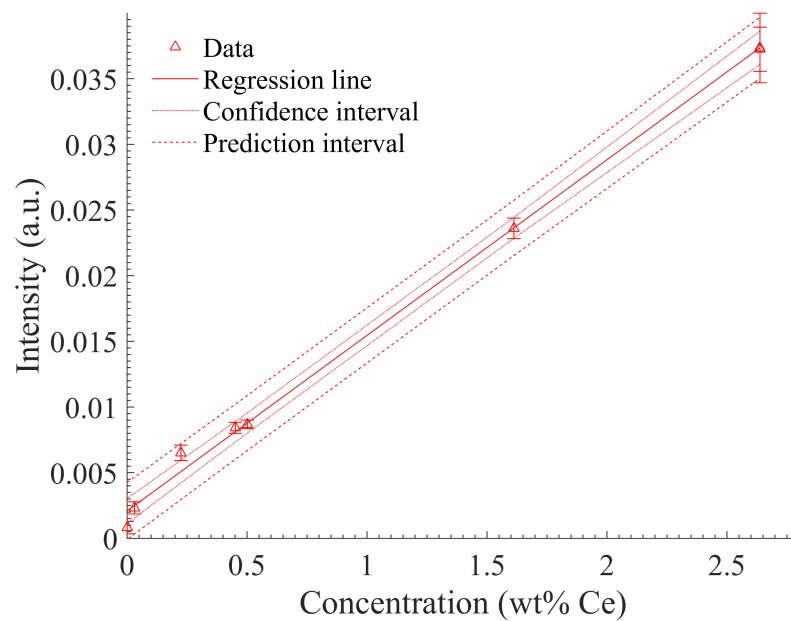
Figure 5.16: Calibration curve calculated from the Ce 428.999 nm line in molten salt.
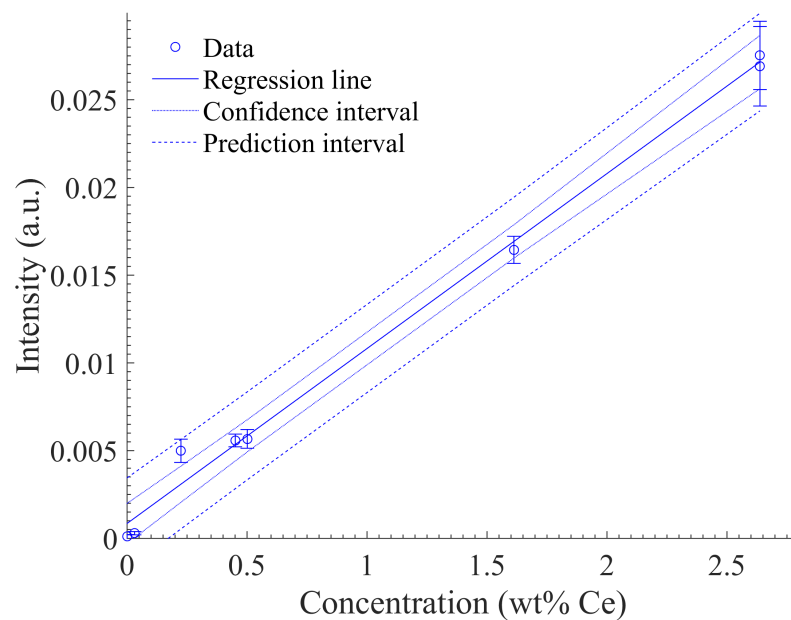

Figure 5.17: Calibration curve calculated from the Ce 457.228 nm line in molten salt.
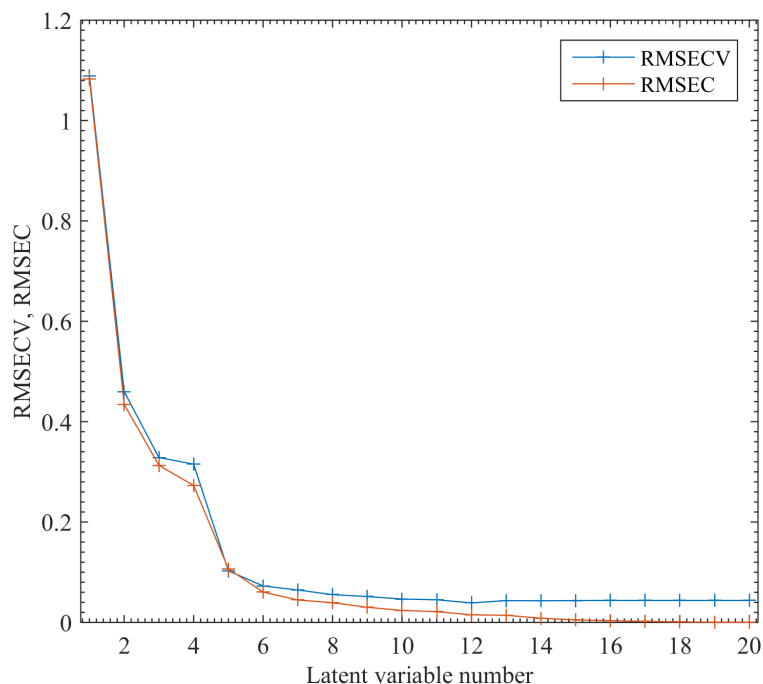
Figure 5.18: PLS model response as a function of the latent variables and the RMSECV.

For all the experimental runs, a multivariate PLS model was generated using the PLS_Toolbox in MATLAB. In the PLS model, the 7 repetitions per experiment were divided into a calibration set (4 repetitions) and validation set (3 repetitions). This resulted in approximately 33 spectra for calibration and 20 for validation. Prior to processing the spectra in the model, each spectra was normalized with respect to the Li 460 nm line. The number of latent variables (LV) were chosen to reduce the RMSECV. Figure 5.18 shows the relationship between the LV's and the RMSECV. The PLS_toolbox suggested 5 LV be used; however, 7 were selected in order to further reduce the RMSECV to 0.0622 wt% or 622 ppm. Figure 5.19 shows the calibration curve generated using the model. Overall the model fits very well with some spread in the data as a result of the deviations between repetitions.

The validation spectra was used to explore the robustness of the model. Figure 5.20 shows the fit of the validation data set with respect to the PLS model. Visually, the PLS model has performed well. When comparing the residuals between the measured and predicted values as shown in Figure 5.21(a), it is apparent that the majority of the results are
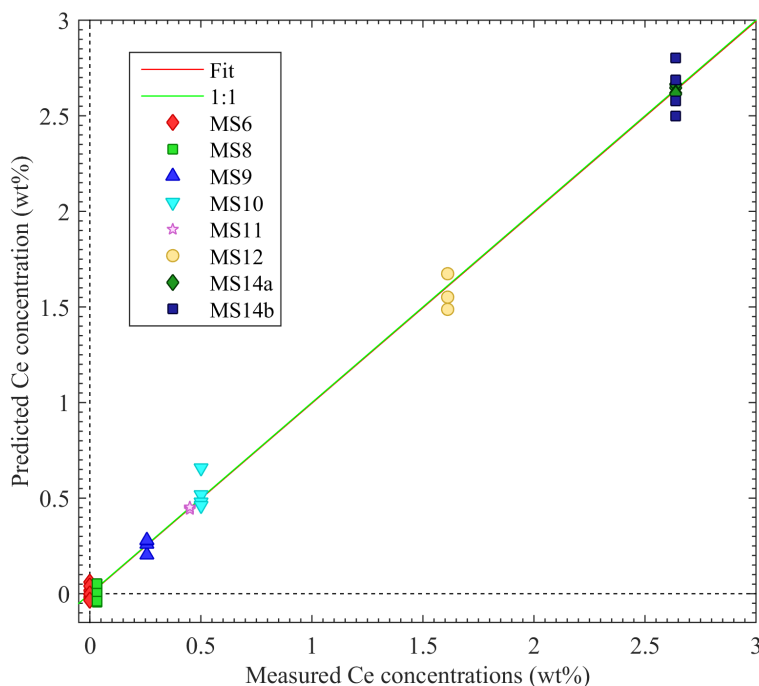
Figure 5.19: PLS model calibration curve for Ce in molten salt.

within approximately 0.1 wt%. Figure 5.21(b) shows the % error between the predicted and measured concentrations. For the 0.1 wt% CeCl$_3$ case (MS8) the % error was high, on the order of 300%. However, for the rest of the data sets, the % error was less than 20%.

Between the univariate and multivariate calibration models, the univariate approach using the 418.660 nm line had the lowest LOD of 504 ppm. The PLS model had a RMSECV of 622 ppm which is not significantly different than the univariate case. However, the PLS model was better at capturing the experimental data, particularly the MS9 experiment where the laser energy was somewhat higher. As a result, the PLS model is more robust in handling data variation and matrix effects.

5.2.3 Conclusions

The aerosol-LIBS system was successfully transitioned to high temperature operation of molten salt within an inert atmosphere glovebox. Initial shakedown testing of the system
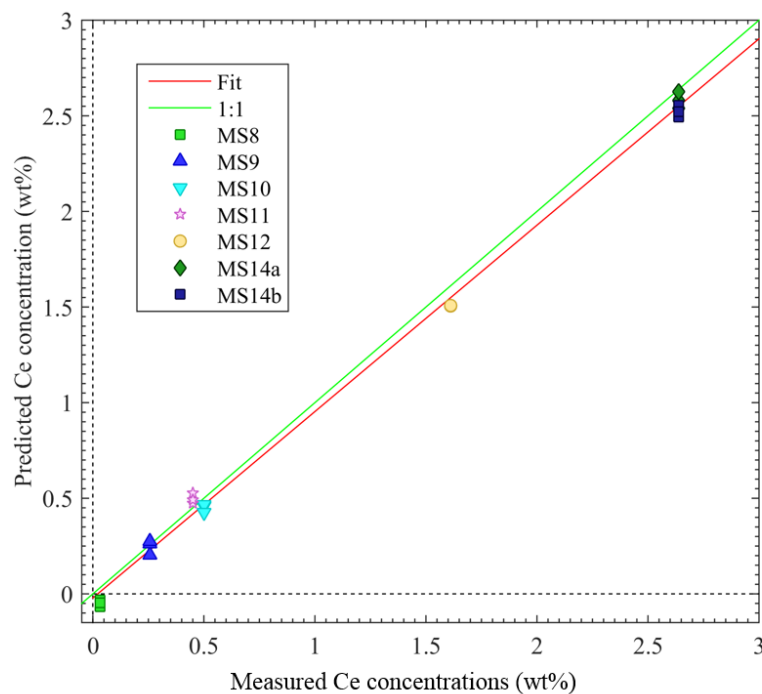
Figure 5.20: Validation curve for the PLS model

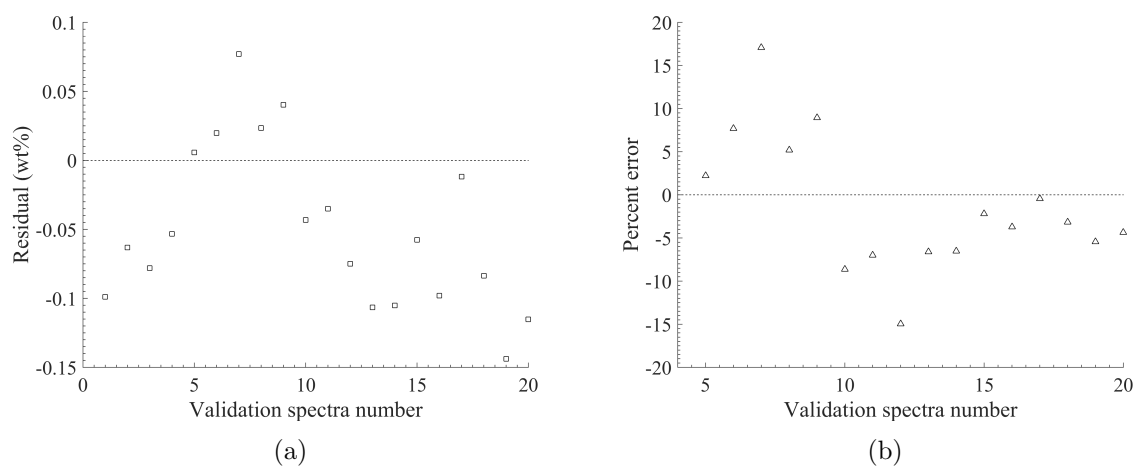(a)   (b)

Figure 5.21: (a) The Residuals between the predicted and measured concentrations for the validation data and (b) the percent error between the predicted and measured data. The first three data point had approximately 300% error and were not shown in the Figure.

yielded several areas where modifications were needed. As a result, significant changes to the design were made. Specifically in the sampling chamber and laser optics. However, during this period, important design and operational criteria were determined. For example, the optimal laser energy was found. In addition, the optimal flow and pressure for a 1-jet and 3-jet nebulizer was also determined.

In the final aerosol-LIBS system design, Ar gas was heated to 550°C prior to being transfered through a length of insulated but un-heated tubing to the nebulizer. The salt was held at 470°C where it was nebulized using a 1-jet system. The sampling chamber had a sudden expansion to direct the aerosol flow and reduce particle interference with the laser light. In addition, the sampling chamber used sapphire windows with grafoil seals. To reduce material loss in the system, a series of two filters were used, the first with a 1.0 μm element and the other with a 0.5 μm element. The laser light at 50 mJ was expanded using a 3X beam expander before being focused into the sampling chamber via a 75 mm lens. This design resulted in a stable aerosol generation and plasma formation.

The Ce concentration effect was studied between the range of 0 to 5 wt% $CeCl_3$. Results showed a strong linear agreement overall between the univariate and multivariate calibration methods. The Ce 418.660 nm line had the greatest sensitivity to concentration changes and had the lowest LOD overall of 504 ppm. The PLS model was more robust with a RMSECV of 622 ppm. Both modeling results have detection limits below the expected Ce concentrations within the electrorefiner. This phase of the project has demonstrated that the molten salt aerosol technique is a viable method for measuring material concentrations within a molten salt despite challenges with degradation of the optics over time.

The successful completion of the surrogate Ce work (Phase III) has yielded an aerosol-LIBS system design that is capable of high temperature operation that is viable over time with normalization. As a result, no major alterations to the system are recommended prior to proceeding to Phase IV and working with UCl_3.

6

Molten UCl₃-LiCl-KCl Salt Aerosol (Phase IV)

6.1 Materials and Methods

The aerosol-LIBS system design and laser equipment were not altered in the transition from Phase III to Phase IV. Please see Section 5 for details of the design, optical configuration, and equipment. However in this phase, procedures and some operating parameters were adjusted as a result of working with depleted uranium. The primary change was related to the disassembly and cleaning phases. Here, the system components could not be removed from the glovebox and washed with nano-pure water to reduce the spread of contamination and to decrease uranium waste. The one exception to this was that the sapphire windows, after being wiped with Chem-wipes in the glovebox, they were transfered out and cleaned with water and acetone between experiments. To prevent significant buildup on the 1.0 μm filter over time, and thus increased pressure drop, this filter was replaced following each experiment. The remainder of the system components were cleaned by scraping followed with dust removal via parafilm.

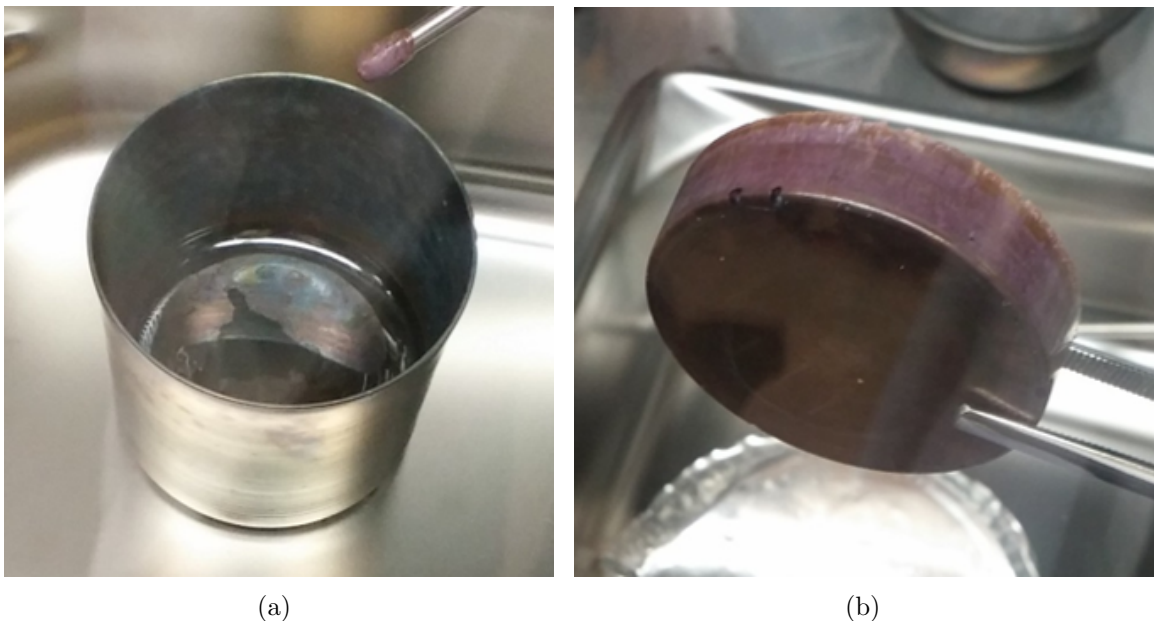Depleted UCl₃ salt (74.4 wt% in LiCl-KCl) was acquired from the Idaho National Labo-

(a)   (b)

Figure 6.1: (a) Molten UCl$_3$-LiCl-KCl at 500°C and (b) the solid salt product after melting.

ratory. Other salts used were LiCl (Alfa Aesar, 99.99%) and KCl (Alfa Aesar, 99.95%). The LiCl-KCl salts were mixed at 44 wt% LiCl and 56 wt% KCl and dried at 250°C for 2-12 hours in a stainless steel crucible. After drying, the salts were melted at 500°C to form a eutectic salt. Following melting, the depleted UCl$_3$ salt was added to form a ternary salt with UCl$_3$ concentrations of 0.3, 1, 2, 3, and 5 wt%. Figure 6.1(a) shows a picture of the prepared salt while still molten. Before the salt solidified, a cold stainless steel rod was inserted into the salt to draw a small sample for ICP-MS analysis. Often a thin oxide layer was observed on the surface of the salt, before collecting the ICP-MS sample, the oxide layer was pushed to the side revealing a pure salt below. Both the stainless steel rod and the oxide formation can be seen in Figure 6.1(a). Figure 6.1(b) shows the solidified salt. Note that the salt has a dark purple color which is characteristic of a UCl$_3$ salt. The solid salt was crushed as before using a pair of wire cutters, the resulting crushed salt is shown in Figure 6.2. This crushed salt was then weighed and then added to the sealed nebulizer through the spout.

Following each experiment, salt samples were taken from 6 different locations throughout the aerosol-LIBS system. These locations are: the nebulizer jar, the nebulizer spout, the

Figure 6.2: Picture of the crushed UCl_3-LiCl-KCl salt prior to being loaded into the nebulizer.

sampling chamber nozzle, the sampling chamber volume cell, the 1.0 μm filter, and the 0.5 μm filter. In some cases, little to no material was recovered in these locations. For the ICP-MS sample preparation, between 0.01 and 0.03 g of material was put in 15 mL test tubes and dissolved in 10 mL of 5% nitric acid for at least 24 hours before they were diluted between 500X and 1250X in order to get the expected concentration of uranium down below the EPA limit of 30 μg/L.

For each of the UCl_3 concentrations studied, 6 repetitions were acquired, each comprised of 300 shots. The laser energy was set at 50±5 mJ and was operated at 2 Hz. The pressure was controlled in order to maintain a 12 psi differential pressure between the nebulizer inlet and the sampling chamber. With this pressure differential, the gas flow rate was constant at 0.31 L/min.

The first 4 uranium experiments (MSU1 through MSU4) were run at 1 wt% UCl_3 in order to optimize the gate delay, assess the observed U peaks, and to explore the effect of gas temperature and pressure. For MSU1 through MSU3 the gas pre-heat furnace was left off and the nebulizer inlet temperature was still 130°C (same as with the pre-heat) due to

Table 6.1: Summary of the UCl$_3$-LiCl-KCl experiments conducted.

Experiment number	wt% UCl$_3$	Date conducted
MSU1	1.0	July 23, 2016
MSU2	1.0	August 17, 2016
MSU3	1.0	August 24, 2016
MSU4	1.0	September 1, 2016
MSU5	1.0	September 30, 2016
MSU6	2.0	October 3, 2016
MSU7	3.0	October 5, 2016
MSU8	5.0	October 7, 2016
MSU9	0.3	October 8, 2016

heating from the melt furnace. It was uncertain that the gas pre-heat had an effect since the nebulizer inlet was the same temperature either way. Experiments MSU4 through MSU9 were operated with the gas pre-heat furnace at 550°C and at a 12 psi pressure differential. Table 6.1 shows a summary of the experiments conducted along with the dates they were run.

6.2 Results and Discussions

6.2.1 Gas Temperature Effect

Following the MSU1 experiment, the salt in the nebulizer jar was purple-brown from oxide formation; however, salt collected everywhere else in the system was pure white suggesting low concentrations of UCl$_3$. This observation was confirmed using ICP-MS as shown in Table 6.2. The UCl$_3$ concentration dropped drastically as the sampling location moves progressively further from the nebulizer. This effect was observed with the CeCl$_3$; however, the effect was not so extreme. As a result, it was thought that because uranium is heavier than cerium, similar sized aerosol droplets with UCl$_3$ are more likely to fall from the slow aerosol gas stream. To test this hypothesis, MSU2 and MSU3 were operated at a higher differential pressure and flow rate.

For MSU2, the pressure differential was maintained at 20 psi. Interestingly, the gas flow

Table 6.2: ICP-MS results from MSU1 with 1 wt% UCl_3.

Location in system	Concentration (wt% UCl_3)	Recovered mass(g)
Nebulizer jar	0.741	27.0625
Nebulizer spout	0.275	0.3487
Nozzle	0.287	0.0497
Sampling Chamber	0.108	0.0131
1.0 μm filter	0.077	0.7003
0.5 μm filter	0.062	1.6268

rate did not noticeably increase. For MSU3, the pressure differential was maintained at 30 psi. In this case, the gas flow rate increased to 0.63 L/min. The concentrations of UCl_3 at the different sampling locations are shown in Figure'6.3(a). The concentration profiles between MSU1 and MSU2 are different but overall the trend is similar. Though the pressures were different between these experiments, the gas flow rates were essentially the same. MSU3 has a less steep concentration gradient overall, indicating that the increased flow rate does mitigate the rate at which the UCl_3 falls from the aerosol gas stream. However, at the 0.5 μm filter, all three experiments have nearly the same low concentration.

Another significant observation between the first three uranium experiments is the overall stability of the aerosol-LIBS system. In the cerium experiments, the aerosol-LIBS system could be left operating for a number of hours (tested up to 14 hours) without significant change in the steady-state pressure and flow rate. During the testing of MSU1, nothing out of the ordinary was noticed with the stability of the system; however, with MSU2 the flow dropped to zero after two hours and with MSU3, the flow dropped to zero after 20 minutes. Presumably the flow was reduced as a result of clogging of the nebulizer tip. This effect was never observed when the gas pre-heat was operating. As a result, experiment MSU4 was run with identical conditions to MSU1 with the exception of the gas-pre-heat being set at 550°C. The MSU4 concentration profile can be seen in Figure 6.3(b). Here, the profile does not drastically drop to low values as was observed with the first three experiments. In fact, the profile is similar to the profile observed in the cerium study. In addition, the amount of
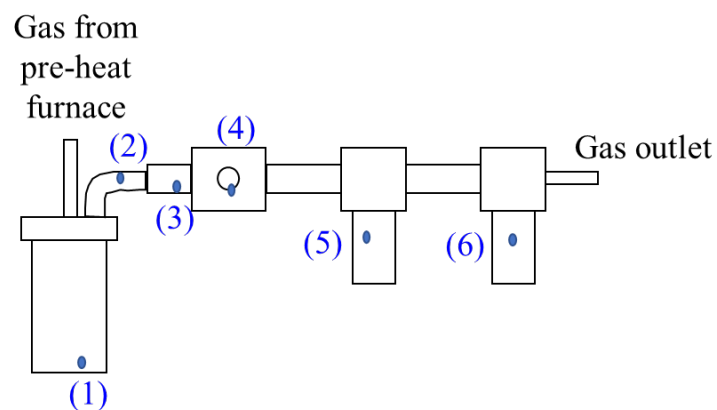
(a)
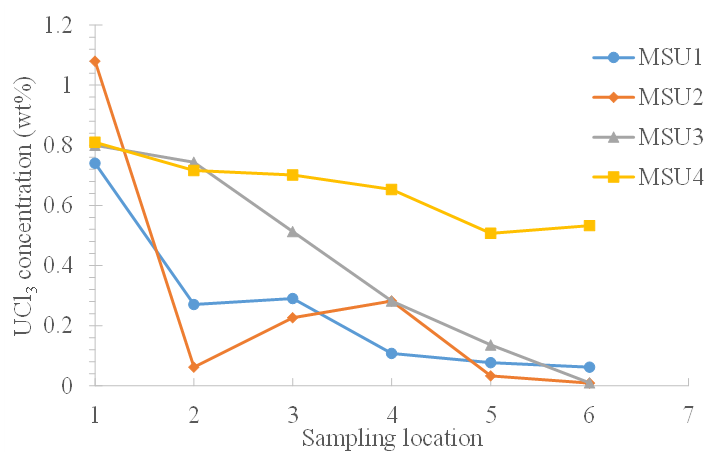
(b)

Figure 6.3: (a) Schematic of the aerosol-LIBS system showing the 6 different salt ssampling locations for ICP-MS and (b) the concentration profiles of the system for the MSU1 through MSU4 experiments.

oxide formation within the nebulizer was significantly reduced in MSU4. The reason for this aspect is unknown.

The actual temperature of the gas at the nebulizer inlet is unknown because the thermocouple in the gas stream is more strongly effected by the temperature of the nebulizer body that it is the gas temperature. Definitely, when the gas pre-heat furnace is operating, the gas temperature is high enough to prevent adverse effects and instabilities in the nebulizer. As a result, the remaining experiments will be done using the gas pre-heat furnace.

6.2.2   LIBS Measurements of UCl₃

The MSU1 through MSU4 were analyses using LIBS. As a result of the more stable operation of MSU4, data sets collected during this experiment were used for peak selection and gate delay optimization. The average spectrum generated from the 6 repetitions was normalized and compared to the normalized average spectrum of pure LiCl-KCl salt (MS6). Both tests were conducted at a 16 μs gate delay. This comparison highlighted differences in the spectra as shown in Figure 6.4. Using this approach, multiple U lines were identified and verified in the literature[5, 20, 23, 43]. Table 6.3 shows the some of the observed lines. The strongest uranium peaks identified were the U II 367.01 nm, U II 385.96 nm, and U I 387.10 nm lines.

During MSU4, the gate delay was varied between 3 μs to 25 μs to determine the optimal value. Figure 6.5 shows the comparison between the different gate delay values. As would be expected, the overall intensity of the spectra decreases with as the gate delay increases. However, it appears that there is a significant background effect at the shorter gate delay values. When the SBR's were calculated for these spectra, the trend was relatively flat. Figure 6.6 shows the intensity decay of several U lines with respect to a region with no U lines. From this comparison, it is apparent that the background is decaying at the same rate as the peaks themselves. This effect was also noted by Chinni et al. [5]. In other words, There are multiple U lines in which the spectrometer currently used (Mechelle 5000) cannot

Table 6.3: Observed U peaks in the UCl$_3$ salt samples.

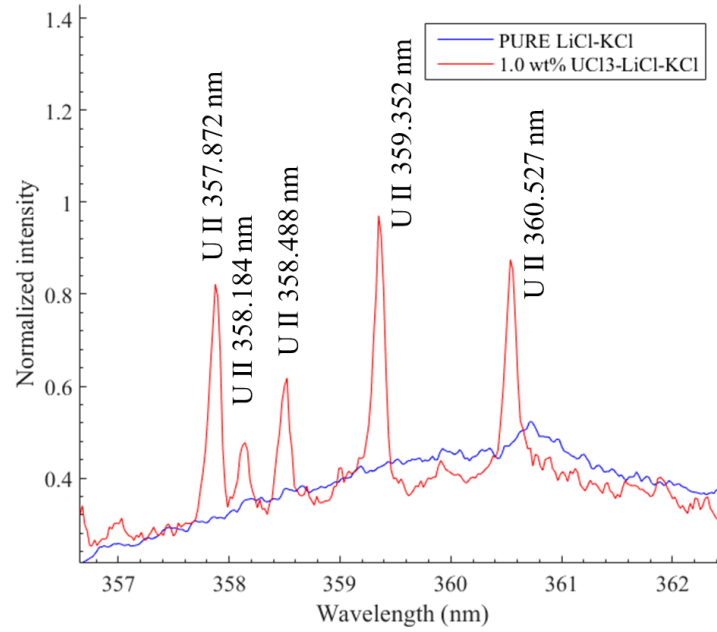| Wavelength (nm)	Ionization State	Wavelength (nm)	Ionization State
357.70	I	394.28	II
358.09	I	400.52	I
358.45	I	401.77	II
359.37	I	406.25	II
360.63	II	409.01	II
365.92	I	417.16	II
367.01	II	435.57	I
374.64	II	436.21	I
381.19	I	437.20	I
381.41	II	439.39	I
385.46	II	457.68	I
385.96	II	502.74	I
386.52	II	562.08	I
387.10	I	607.73	I
387.85	I		

Figure 6.4: Comparison between the MSU4 spectrum and the MS6 spectrum generated using pure LiCl-KCl salt.
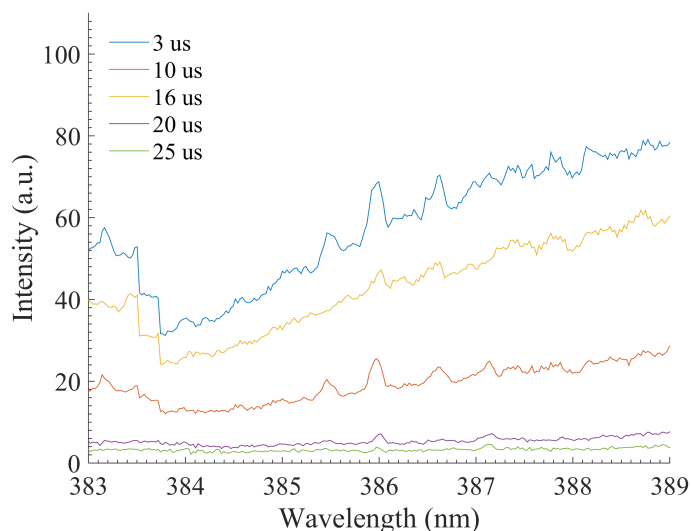
Figure 6.5: Comparison between the spectra as a function of the gate delay.

be resolve and as a result appears like background noise. As a result, the 3 μs gate delay was selected in this work as it has the greatest intensity. The actual optimal gate delay may be at a shorter wavelength than studied here.

Figure 6.7 shows the entire spectra generated for the 1 wt% UCl$_3$ (MSU4) experiment at a 3 μs gate delay. The spectrum in dominated by the Li, K, and Ar lines as observed before with both the aqueous and cerium work. In the close up region of the U lines, a cyclic pattern in the observed background is observed. This is a result of transmission efficiencies of the echelle grating. The 5 different experiments (MSU5 through MSU9) were run with different concentrations of UCl$_3$. The %RSD's between the 6 repetitions typically averaged between 2.5% and 8%. MSU8 (5 wt% UCl$_3$) had the best %RSD and MSU9 (0.3 wt% UCl$_3$) had the worst. Figure 6.8 shows the best and worst %RSD cases.

The differences between the uranium spectra collected were analyzed using the %RSD. Figure 6.9(a) shows the %RSD between MSU5 through MSU9. Here, the %RSD peaks around 25% which is an improvement over the cerium study. However, by normalizing each spectrum with respect to its mean value between 600 nm and 811 nm, the %RSD between the different cases drops to around 12% for the region without U lines as shown in Figure 6.9(b).
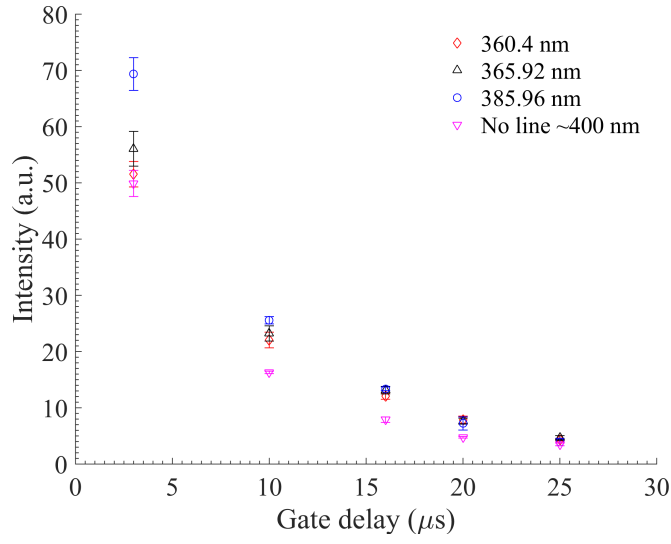
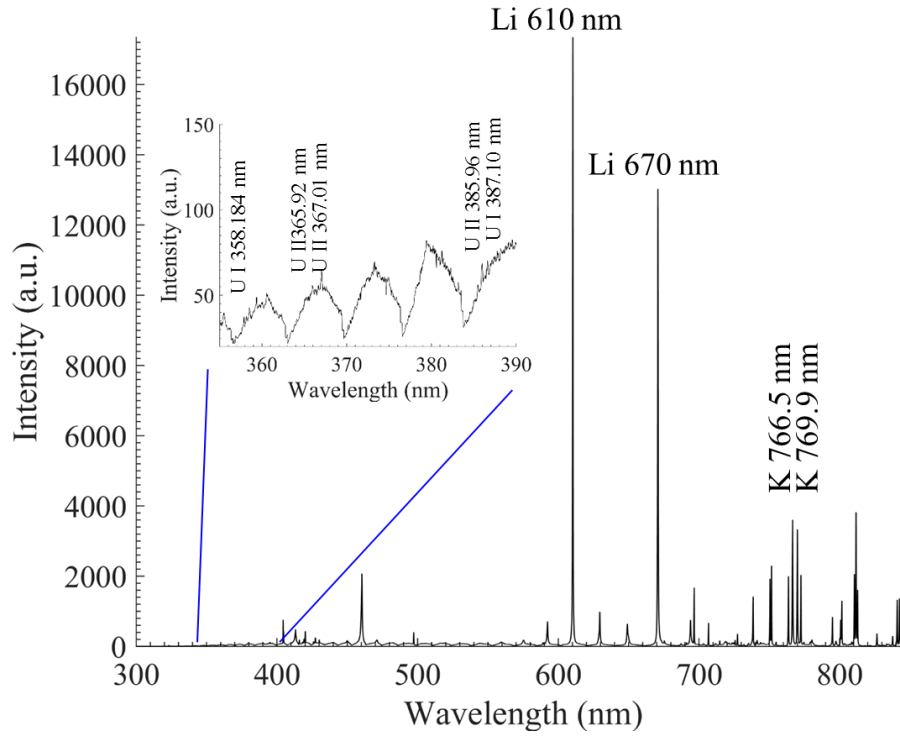Figure 6.6: Comparison between the spectra as a function of the gate delay.

Figure 6.7: Comparison between the spectra as a function of the gate delay.
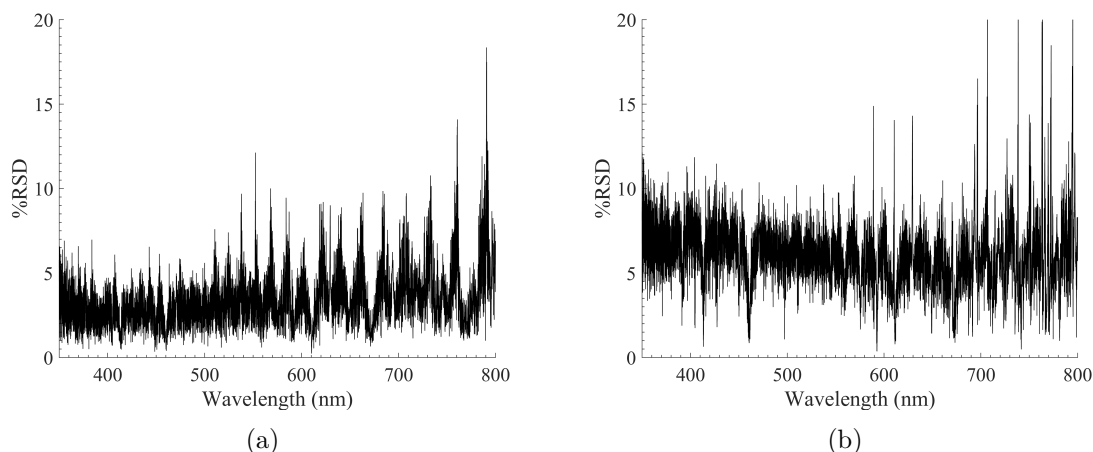
Figure 6.8: (a) %RSD for the 5 wt% UCl$_3$ (MSU8) case and (b) the %RSD for the 0.3 wt% UCl$_3$ (MSU9) case.

Table 6.4: Regression coefficients and LOD for the three different calibration curves generated.

Parameter	367.01 nm	385.96 nm	387.10 nm
b_0	0.0142	0.0169	0.0066
b_1	-5.23e-04	1.46e-04	-4.34e-04
R^2	0.9976	0.9981	0.9612
LOD (wt% U)	0.1115	0.0981	0.1749
LOD (ppm U)	1115	981	1749

The high variation in the region with the majority of the U lines is a result of the varying U concentrations between experiments.

The spectral response with respect to the concentration in the region of the U 385.96 nm line is shown in Figure 6.10. As expected, the, overall intensity of the spectra increases with the U concentration. The MATLAB GUI was used to calculate the area under the spectral line of interest. Univariate calibration curves were generated using the calculated peak areas for the 367.01 nm, 385.96 nm, and the 387.10 nm lines and the resulting curves are shown in Figures 6.11, 6.12, and 6.13, respectively. The U 385.96 line has the steepest slope and is the most sensitive to U concentration changes with the lowest LOD of 981 ppm. As a result, the U 385.96 nm line is recommended for use with the Univariate calibration method.

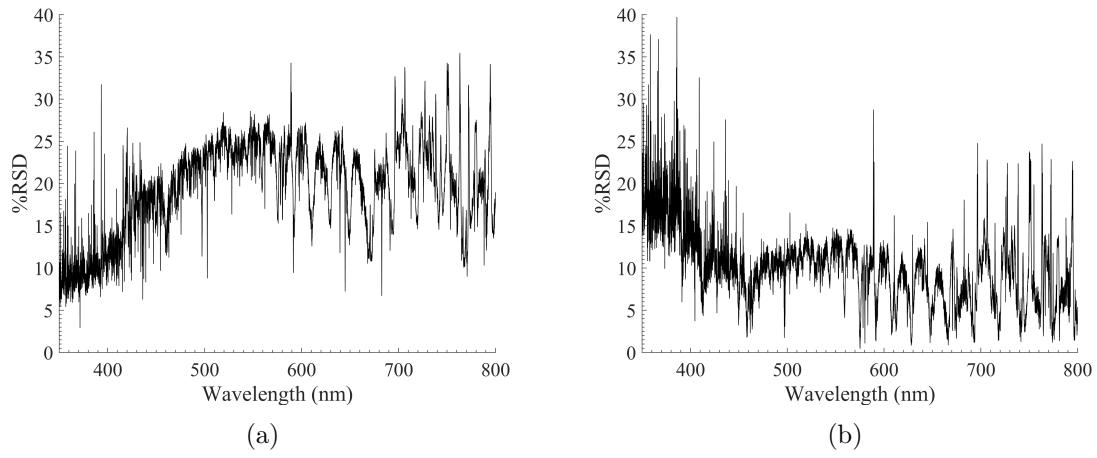The different experiments were also analyzed using the PLS_toolbox in MATLAB. In

Figure 6.9: %RSD for the U spectra over time (MSU5-MSU9) (a) without normalization and (b) with normalization.
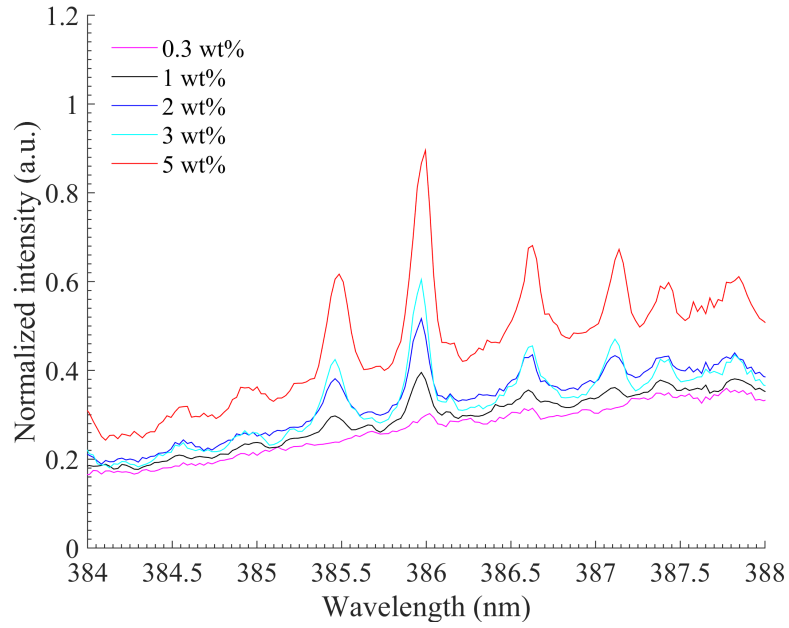

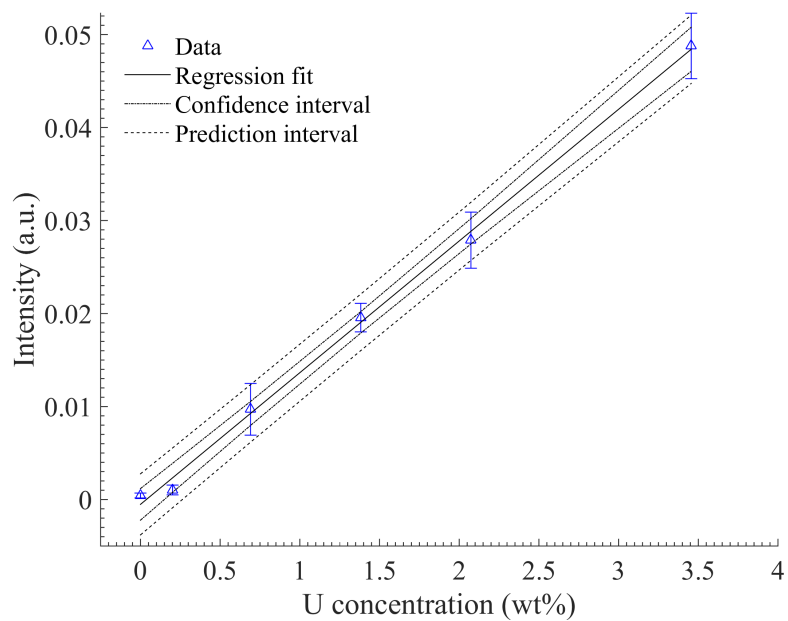Figure 6.10: Comparison between the spectra as a function of the gate delay.

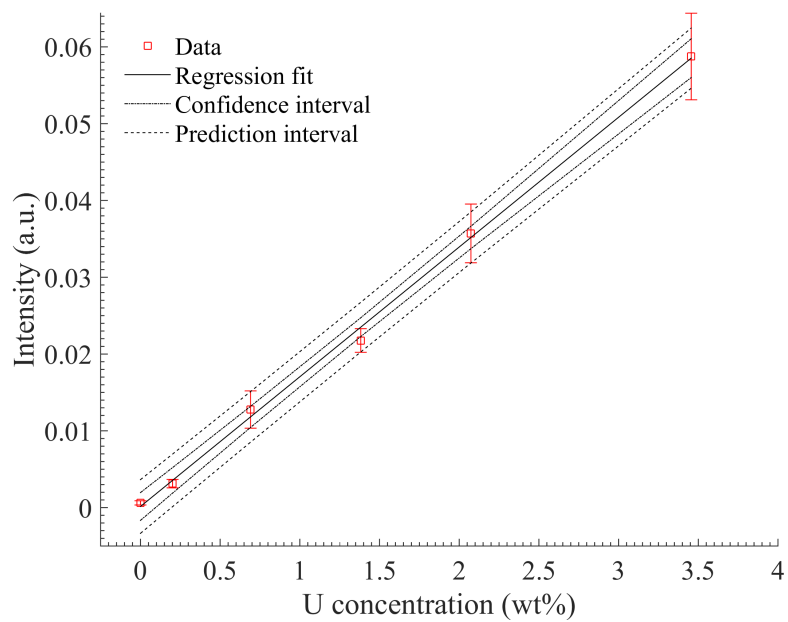Figure 6.11: Univariate calibration curve generated using the U 367.01 nm line.

Figure 6.12: Univariate calibration curve generated using the U 385.96 nm line.
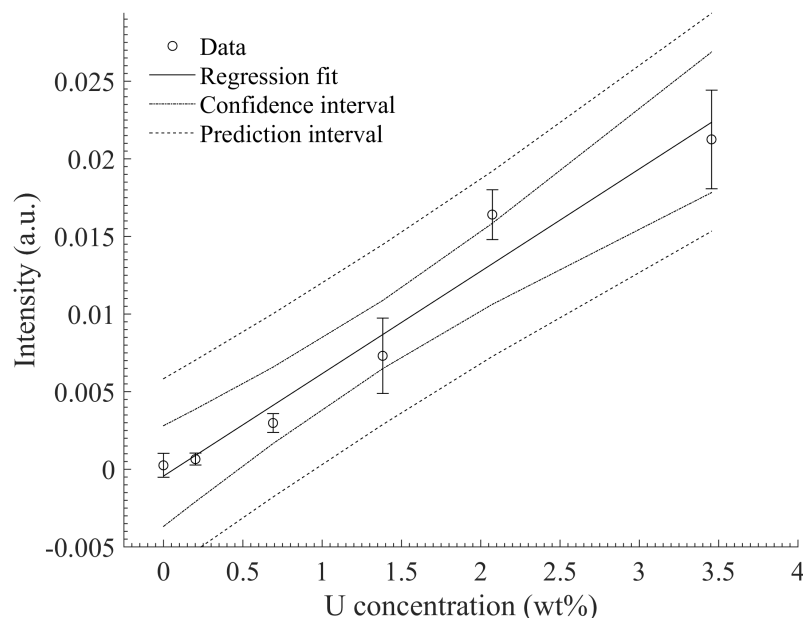
Figure 6.13: Univariate calibration curve generated using the U 387.10 nm line.

this case, each repetition is divided into two data sets, one for calibration and the other for validation. The RMSECV is calculated using venetian blinds. Figure 6.14 shows the LV with respect to the RMSECV for the generated model. In this model, 7 LV numbers were selected which yields a RMSECV of 926 ppm. Figure 6.15 shows the modeled calibration curve. Figure 6.16 shows the validation results generated using the last three repetitions from each experiment. The model fits the data well (% error less than 12%)where the actual concentration is greater than the RMSECV. Below the RMSECV the fit is poor with % error being between -100% and 200%. No blind or unknown samples were run to further test the calibration results.

6.3 Conclusions

With the successful testing of the aerosol-LIBS system using $CeCl_3$ in Phase III, salt samples containing UCl_3 were being analyzed. The system design has not been modified; however, several procedural changes were made and the effect of the gas pre-heat was explored. As
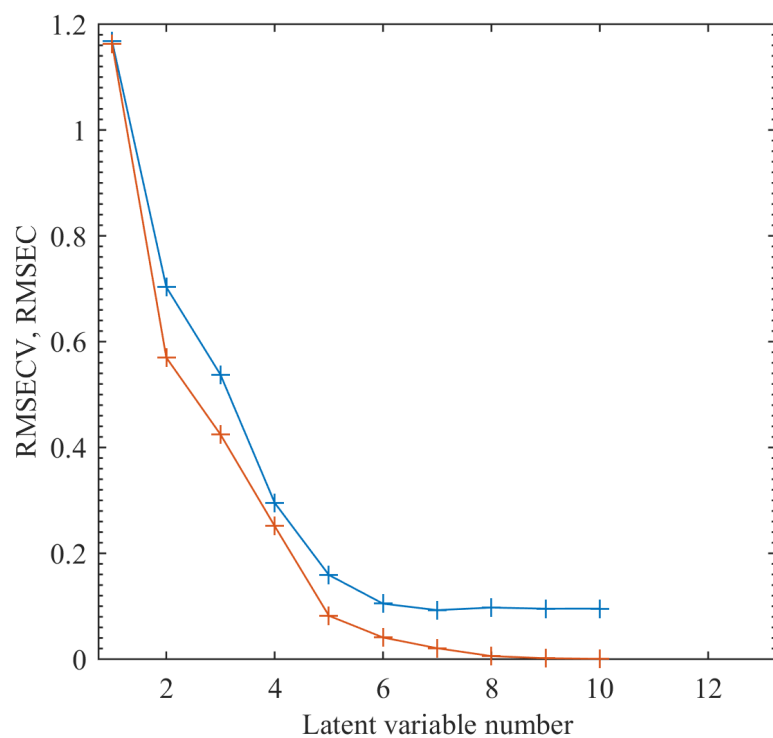
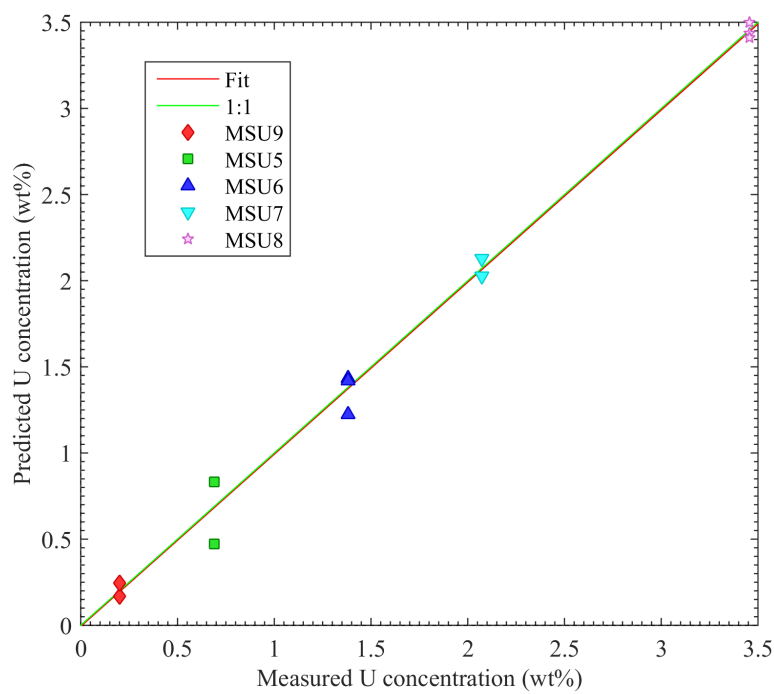Figure 6.14: The RMSECV with respect to the number of LV used in the PLS model.

Figure 6.15: Multivariate calibration curve generated from the first three repetitions from each U experiment.
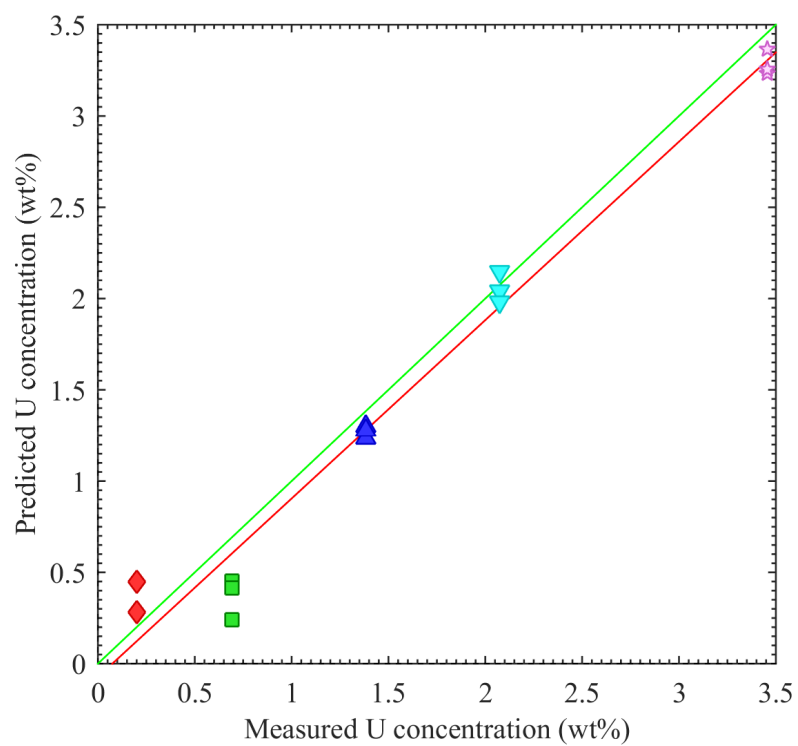
Figure 6.16: Multivariate calibration curve generated from the first three repetitions from each U experiment.

a result of using uranium, components could not be easily removed from the glovebox and washed as was done previously with the cerium experiments. Thus, cleaning was done using extensive scraping and material removal via parafilm. In addition, a new 1.0 μ filters was used in every experiment to prevent changes in the steady-state pressure drop across the system.

The first three uranium experiments were run to explore the effect of the gas pre-heat temperature with respect to the gas pressure and flow rate. Results indicate that without the gas pre-heat at 550°C, the U concentration within the system components decreases as the distance from the nebulizer increased. This effect was controlled by adjusting the gas flow rate. Concentration profiles with the gas pre-heat were similar to those obtained for the cerium cases.

The LOD for U in a molten salt aerosol was determined to be 981 ppm and 926 ppm for the univariate and multivariate cases, respectively. Unknown or blind samples were not run; however validation results show good correlation for data sets above the detection limit. The successful competition of this phase strongly supports the aerosol-LIBS approach as a viable method for measuring the electrorefiner salt used during pyroprocessing of used nuclear fuel.

7

References

1. Laidler, J., Battles, J., Miller, W., Ackerman, J. & Carls, E. Development of Pyroprocessing Technologies. *Progress Nuclear Energy* **31,** 131 (1997).

2. Garcia, H. E., Lineberry, M. J., Aumeier, S. E. & McFarlane, H. F. Proliferation Resistance of Advanced Sustainable Nuclear Fuel Cycles. *Nuclear Plant Journal* **20,** 18–27 (2002).

3. Phongikaroon, S. & Simpson, M. Equilibrium model for ion exchange between multivalent cations and zeolite-A in a molten salt. *AIChE Journal* **52,** 1736–1743 (2006).

4. Pasquini, C., Cortez, J., Silva, L. M. C. & Gonzaga, F. B. Laser Induced Breakdown Spectroscopy. *J. of the Braz. Chem. Soc.* **18,** 463 (2007).

5. Chinni, R. C., Cremers, D., Radziemski, L. J., Bostian, M. & Navarro-Northrup, C. Detection of Uranium using Laser-Induced Breakdown Spectroscopy. *Appl. Spectrosc.* **63,** 1238–1250 (2009).

6. Wachter, J. R. & Cremers, D. A. Determination of Uranium in Solution Using Laser-Induced Breakdown Spectroscopy. *Appl. Spectrosc.* **41,** 1042–1048 (1987).

7. St-Onge, L., Kwong, E., Sabsabi, M. & Vadas, E. B. Rapid analysis of liquid formulations containing sodium chloride using laser-induced breakdown spectroscopy. *Journal of Pharmaceutical and Biomedical Analysis* **36,** 277 (2004).

8. Barreda, F., Trichard, F., Barbier, S., Gilon, N. & Saint-Jalmes, L. Fast quantitative determination of platinum in liquid samples by laser-induced breakdown spectroscopy. *Analytical and Bioanalytical Chemistry* **403,** 2601–2610 (2012).

9. Tambay, R. & Thareja, R. Laser-induced breakdown studies of laboratory air at 0.266, 0.355, 0.532, and 1.06 um. *Journal of Applied Physics* **70,** 2890–2892 (1991).

10. Martin, M. Z., Cheng, M. & Martin, R. C. Aerosol measurement by laser-induced breakdown spectroscopy: A Review. *Aerosol Science and Technology* **31,** 409 (1991).

11. Cahoon, E. M. & Almirall, J. R. Quantitative Analysis of Liquids from Aerosol and Microdrops using Laser Induced Breakdown Spectroscopy. *Analytical Chemistry* **84,** 2239–2244 (2012).

12. Effenberger, A. J. *Methods for measurement of Heterogeneous materials with laser-induced breakdown spectroscopy (LIBS)* ProQuest/UMI. (Publication No. 3369015.) PhD thesis (University of California, San Diego, 2009).

13. Hanson, C., Phongikaroon, S. & Scott, J. R. Temperature effect on laser-induced breakdown spectroscopy spectra of molten and solid salts. *Spectrochimica Acta Part B: Atomic Spectroscopy* **97,** 79–85 (2014).

14. Weisberg, A., Lakis, R., Simpson, M. F., Horowitz, L. & Craparo, J. Measuring Lanthanide Concentrations in Molten Salt Using Laser-Induced Breakdown Spectroscopy (LIBS). *Applied Spectroscopy* **68,** 937–948 (2014).

15. *Application of Laser-Induced Breakdown Spectroscopy to Electrochemical Process Monitoring of Molten Chloride Salts* (Vienna, Austria, 2014).

16. Hanson, C. *LASER-INDUCED BREAKDOWN SPECTROSCOPY - TEMPERATURE EFFECTS ON SPECTRA OF MOLTEN SALTS SYSTEMS* PhD thesis (University of Idaho, Idaho Falls, Idaho, 2013).

17. Sarkar, A., Alamelu, D. & Aggarwal, S. K. Determination of thorium and uranium in solution by laser-induced breakdown spectrometry. *Appl. Opt.* **47,** G58–G64 (2008).

18. Sarkar, A., Alamelu, D. & Aggarwal, S. K. Gallium quantification in solution by LIBS in the presence of bulk uranium. *Optics Laser Technology* **44,** 30 (2012).

19. Sirven, J. *et al.* Towards the determination of the geographical origin of yellow cake samples by laser-induced breakdown spectroscopy and chemometrics. *J. Anal. At. Spectrom.* **24,** 451–459 (2009).

20. Judge, E. J., II, J. E. B., Berg, J. M., Clegg, S. M. & Havrilla, G. J. Laser-induced breakdown spectroscopy measurements of uranium and thorium powders and uranium ore. *Spectroc. Acta Pt. B-Atom. Spectr.* **83-84,** 28–36 (2013).

21. Sarkar, A., Alamelu, D. & Aggarwal, S. K. Laser-induced breakdown spectroscopy for determination of uranium in thorium-uranium mixed oxide fuel materials. *Talanta* **78,** 800 (2009).

22. Zheng, H. *et al.* Analysis of plutonium oxide surrogate residue using laser-induced breakdown spectroscopy. *Spectrochimica Acta Part B: Atomic Spectroscopy* **63,** 968–974 (2008).

23. Barefield, J. E. *et al.* Analysis and Spectral Assignments of Mixed Actinide Oxide Samples Using Laser-Induced Breakdown Spectroscopy (LIBS). *Appl. Spectrosc.* **2013,** 433–440 (67).

24. Smith, C., Martinez, M., Veirs, D. & Cremers, D. Pu-239/Pu-240 isotope ratios determined using high resolution emission spectroscopy in a laser-induced plasma. *Spectroc. Acta Pt. B-Atom. Spectr.* **57,** 929–937 (2002).

25. Doucet, F. R., Lithgow, G., Kosierb, R., Bouchard, P. & Sabsabi, M. Determination of isotope ratios using Laser-Induced Breakdown Spectroscopy in ambient air at atmospheric pressure for nuclear forensics. *J. Anal. At. Spectrom.* **26,** 536–541 (2011).

26. Cremers, D. A., Radziemski, L. J. & Loree, T. R. Spectrochemical Analysis of Liquids Using the Laser Spark. *Appl. Spectrosc.* **38,** 721–729 (1984).

27. Pearman, W., Scaffidi, J. & Angel, S. M. Dual-pulse laser-induced breakdown spectroscopy in bulk aqueous solution with an orthogonal beam geometry. *Appl. Opt.* **42,** 6085–6093 (2003).

28. Cheung, N. H. & Yeung, E. S. Single-shot Elemental Analysis of Liquids based on Laser Vaporization below Breakdown. *Appl. Spectrosc.* **47,** 882–886 (1993).

29. Kumar, A., Fang, F. Y. & Singh, J. P. Double-pulsed laser-induced breakdown spectroscopy with liquid jets of different thicknesses. *Applied Optics* **42,** 6047–6051 (2003).

30. Feng, Y. *et al.* Investigation of laser-induced breakdown spectroscopy of a liquid jet. *Appl. Opt.* **49,** 70–74 (2010).

31. Yaroshchyk, P., Morrison, R. J. & D. Bod and, B. L. C. Quantitative determination of wear metal in engine oils using laser-induced breakdown spectroscopy: A comparison between liquid jets and static liquid. *Spectrochimica Acta Part B: Atomic Spectroscopy* **60,** 986–992 (2005).

32. Fisher, B. T., Johnson, H. A., Buckley, S. G. & Hahn, D. W. Temperol Gating for the Optimization of Laser-Induced Breakdown Spectroscopy Detection and Analysis of Toxic Metals. *Applied Spectroscopy* **55,** 1312–1319 (2001).

33. Carranza, J. E., Fisher, B. T., Yoder, G. D. & Hahn, D. W. On-line Analysis of Ambient Air Aerosols using Laser-Induced Breakdown Spectroscopy. *Spectrochemica Acta Part B: Atomic Spectroscopy* **56,** 851 (2001).

34. Carranza, J. E. & Hahn, D. W. Sampling Statistics and Considerations for Single-Shot Analysis using Laser-Induced Breakdown Spectroscopy. *Spectrochemica Acta Part B: Atomic Spectroscopy* **57,** 779–790 (2002).

35. Diwakar, P. K., Looper, K. H., Matiaske, A. & Hahn, D. W. Laser-Induced Breakdown Spectroscopy for Analysis of micro and nanoparticles. *J. Anal. At. Spectrom.* **27,** 1110–1119 (2012).

36. Huang, J. S., Ke, C. B., Huang, L. S. & Lin, K. C. The correlation between ion production and emission intensity in the laser-induced breakdown spectroscopy of liquid droplets. *Spectrochimica Acta Part B: Atomic Spectroscopy* **57,** 35 (2002).

37. J. Huang C. Ke, K. L. Matrix effect on emission/current correlated analysis in laser-induced breakdown spectroscopy of liquid droplets. *Spectrochimica Acta Part B: Atomic Spectroscopy* **59,** 321 (2004).

38. Poulain, D. E. & Alexander, D. R. Influences on Concentration Measurements of Liquid Aerosols by Laser-Induced Breakdown Spectroscopy. *Applied Spectroscopy* **49,** 569–579 (1995).

39. Schechter, I. Direct Aerosol Analysis by Time Resolved Laser Plasma Spectroscopy – Improvement by single shot Measurements. *Analytical Science and Technology* **8,** 779–786 (1995).

40. Kumar, A., Yueh, F. Y., Miller, T. & Singh, J. P. Detection of trace elements in liquids by laser-induced breakdown spectroscopy with a Meinhard nebulizer. *Appl. Opt.* **42,** 6040–6046 (2003).

41. Martin, M. & Cheng, M. Detection of Chromium Aerosol Using Time-Resolved Laser-Induced Plasma Spectroscopy. *Appl. Spectroscopy* **54,** 1279–1285 (2000).

42. Alvarez-Trujillo, L., Ferrero, A. & Laserna, J. J. Preliminary studies on stand-off Laser-Induced Breakdown Spectroscopy Detection in Aerosols. *J. Anal. At. Spectrom.* **23,** 885–888 (2008).

43. Kramida, A., Ralchenko, Y., J., R. & Team, N. A. *NIST Atomic Spectra Database (version 5.3)* <http://physics.nist.gov/asd> (2015).

44. May, K. R. The Collison nebulizer: Description, performance and application. *J. Aerosol Sci.* **4,** 235 (1973).

45. Stewart, R. B. & Jacobson, R. T. Thermodynamic properties of argon from the triple point to the 1200K with pressures to 1000 MPa. *J. Physical Chem. Ref. Data* **18** (1989).

46. Bucenieks, I. E. High Pressure and High Flowrate Induction Pumps with Permanent Magnets. *Magnetohydrodynamics* **39,** 411–417 (2003).

47. Bucenieks, I. E., Sukhovich, E. P. & Shcerbinin, E. A Centrifugal Pump Based on Rotating Permanent Magnets. *Magnetohydrodynamics* **36,** 157–163 (2000).

48. Bucenieks, I. E. Perspectives of Using Rotating Permanent Magnets in the Design of Electromagnetic Induction Pumps. *Magnetohydrodynamics* **36,** 151–156 (2000).

49. Bucenieks, I. E. & Kravalis, K. Efficiency of EM Induction Pumps with Permanent Magnets. *Magnetohydrodynamics* **47,** 89–96 (2011).

50. *Evaluation of Parameters of Powerful Electromagnetic Induction Pumps on Permanet Magnets for Heavy Liquid Metals* (Rome, Italy, 2007).

51. Bucenieks, I. E., Kravalis, K. & Krishbergs, R. Pressure-Flow Rate Characteristics of Pumps with Permanent Magnets. *Magnetohydrodynamics* **47,** 97–104 (2011).

52. *Magnetic Field Distribution in the Rotor of the Permanent Magnets* (Rigas, Jurmala, 2005).

53. *Proposed Mercury Pump for EES* (Dusseldorf-Neuss, Germany, 2003).

54. *Analysis and Design of Electromagnetic Pump* (Bangalore, India, 2010).

55. Peng, Y. & Zhao, L. Experimental Study on Alternating Magnetic Field Magnetohydrodynamic Pump. *Journal of Hydrodynamics* **20,** 591–595 (2009).

56. Kogawa, H., Haga, K., Wakui, T. & Futakawa, M. Development on Mercury Pump for JSNS. *Nuclear Instruments and Methods in Physics Research A* **600,** 97–99 (2009).

Appendix A

Magnetic Pump (Phase I(a)

Due to the extreme operating conditions and safety constraints of this project, conventional pumping mechanisms are not sufficient. Traditional mechanical pumps (gear, vane, diaphragm) will not work well with this project due to temperature as well as decontamination between experimental samples. Gravity fed flow is a possibility, however, in LIBS multiple shots (50-1000) must be made for every sample. As a result, the time required to acquire the spectral data may be too long for measurement via this method. Another possibility is using electromagnetic (EM) pumps. Two main types of EM pumps exist, they are: conductive and induction type pumps.

In an conductive EM pump, electrodes are used to create a current in the conductive liquid in a channel. Perpendicular to the electric current, a magnetic field is supplied. The combined electric and magnetic fields create a force, called the Lorentz force, that directs the flow down the channel. This type of pump is effective at pumping any electrically conducting fluid. However, this type of pump is not ideal for the current application due to the use of electrodes in the design. In other words, fission product and uranium ions present in the fluid flow could be reduced at the cathode while chlorine gas is oxidized at the anode. Selection of an operating voltage sufficient to drive the fluid without a significant reactions presents a large challenge outside the scope of the current project.

Induction type EM pumps use the idea of a traveling magnetic wave. Typically induction pumps use 3 phase AC current to induce a magnetic field. Due to the nature of 3 phase current and the stator windings, the magnetic field as felt by the ionic liquid is traveling with alternating magnetic poles. This alternating magnetic field creates eddy currents in the ionic liquid. The combined effect of the moving magnetic field and induced eddy currents is the Lorentz force that then pumps the fluid. This style of pump is convenient with working with uranium because the channel is the only portion of the pump exposed. Several high temperature induction EM pumps are commercially available; however, the available sizes are much greater than required by the current application. The high temperature application provides a challenge for insulating the windings in the pump. Also, the nature of the 3 phase windings makes this pump a challenge to custom build a small EM pump for the application. As a result, a more innovative EM pump design is needed.

One such design is an induction EM pump using rotating permanent magnets[46–54]. In this design, permanent magnets of alternating polarity are located on a spindle or rotor as shown in Figure A.1. The fluid is in a channel adjacent to the rotating magnetic field. The alternating traveling magnetic field induces eddy currents, and via the Lorentz force, the fluid is pumped through the channel. The advantage of this EM pump design is that it is relatively easy to build and operate. As a result, an EM pump based on permanent rotating magnets was selected to drive the molten salt in the loop. Several types of permanent magnet pumps have been explored in the literature including the rotor[48, 55, 56], disc[51], and centrifugal[47] designs. The rotor-style EM pump is the most common, however, the efficiency of disc-type design is greater because of the stronger magnetic flux due to magnets on the opposing disc[46]. The disadvantage of disc-type pumps is structural strength at high flow rates. For this application, only low flow rates are required and thus, the disc-type permanent magnet EM pump was selected for the design.
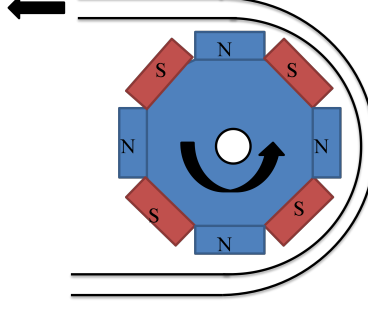
Figure A.1: Schematic representing the rotor style permanent magnet EM pump.

A.1 EM Pump Design Equations

Several design equations have been identified in the literature to provide insight on the design of a permanent magnet EM pump for the current application. To design a pump, it is important to understand the relationship between the pressure and flow generated by the pump. The maximum pressure developed by the pump can be expressed by[46, 48]:

$$P_{max} = 0.5\sigma B^2 V_B l_{ch} sk \tag{A.1}$$

$$V_B = 2\pi Rn \tag{A.2}$$

$$s = 1 - \frac{V_m}{V_B} \tag{A.3}$$

where, σ is the electrical conductivity of the fluid, B is the average magnetic field in the channel, V_B is the velocity of the traveling magnetic field, l_{ch} is the active length of the channel, s is the slip, k is a coefficient accounting for pressure drop due to the transversal end effect, R is the mean radius of the channel, n is the rotation speed, and V_m is the velocity of the liquid in the channel. Eqns. A.1, A.2, and A.3 appear to correlate very well with experimental data[46, 48]. With these equations, the parameters B, R, and l_{ch}, can be adjusted to achieve the desired pressure flow rate relationship for a given n. As the rotation speed n, increases, the amount of pressure generated by the pump increases. Therefore, for a given pump design, varying flow rates can be achieved simply by adjusting the rotation

speed.

Another key aspect of designing a permanent magnet EM pump is selecting the appropriate motor. To do this, it is essential to understand the losses in the pump. The losses due to induced eddy currents in the fluid is given by[46, 48]:

$$W_f = 0.5\sigma(BV_B s)^2 k L_{ch} 2ab \tag{A.4}$$

where, $2a$ is the width of the channel and b is its thickness. Losses are also generated in the channel walls if the wall material is electrically conductive. Under these circumstances the losses are given by:

$$W_w = 0.5\sigma_w(BV_B)^2 k L_{ch} 2a2\delta_w \tag{A.5}$$

where σ_w is the electrical conductivity of the wall material and δ_w is the thickness of the wall. The total energy required to drive the pump is given by:

$$W = W_f + W_w + PQ + W_0 \tag{A.6}$$

where P is the pressure, Q is the flow rate (PQ is the hydraulic energy of flow), and W_0 is the energy required to drive the free rotor without load.

A.2   Pump Design

For the LIBS study on flowing molten salt, it is desired to be capable of pumping the fluid at a flow rate of at least 1 L/min. Using Eqns. A.1, A.2, and A.3, pump parameters have been identified and are shown in Table A.1. At the aforementioned flow rate and selected parameters, with a disc rotation at 4,800 RPM, the maximum pressure generated by the pump in 100 Pa. This is enough to overcome the pressure losses generated by flow through the remaining molten salt loop. Using Eqns. A.4, A.5, and A.6, the required motor size must be greater than 1.0 W. Since the pump magnets are to see very high temperatures,

Table A.1: Physical parameters of the designed EM pump.

Parameter	Value	Unit
R	0.07	m
l_{ch}	0.33	m
$2a$	0.0235	m
b	0.004	m
δ_w	0.001	m

special magnetic materials are required to prevent de-magnetization. A SmCo magnet has been identified from Electron Energy Corporation that can be operated up to 500°C. The size of magnet was selected to be 1.25 in x 0.6 in x 0.4 in. The direction of magnetism is through the 0.4 in dimension. At 500°C the residual induction (Br) of the magnet is 0.68 T. At this strength, the flux in the center of the channel is estimated to be approximately 0.35 T.

Having established the basic dimensions and magnetic parameters, the disc and channel was designed. At the maximum operating RPM of the pump, a significant amount of centrifugal force is present on the magnets. To sufficiently secure the magnets, a design using a ferro-magnetic backing with a stainless steel (SS) pocket was designed as shown in Figure A.2. The SS pocket and the ferro-magnetic backing material will be fastened together using 0.25 in screws. Finite element analysis (FEA) was done on the disc to simulate the forces and stresses on the disk as a result of the high rotation speed. Autodesk Inventor was used in the design and FEA analysis. The design is sufficient to withstand all applied forces.

A.3 Prototype 1

The molten salt loop is made of 0.5 inch stainless steel tubing, connected with Swagelok fittings, and has a total volume of approximately 100 mL. This volume corresponds to roughly 140 g of the LiCl-KCl salt at 500°C. Since the salt is solid at room temperature, a method is needed to add the solid salt into the loop before melting. To accomplish this, a
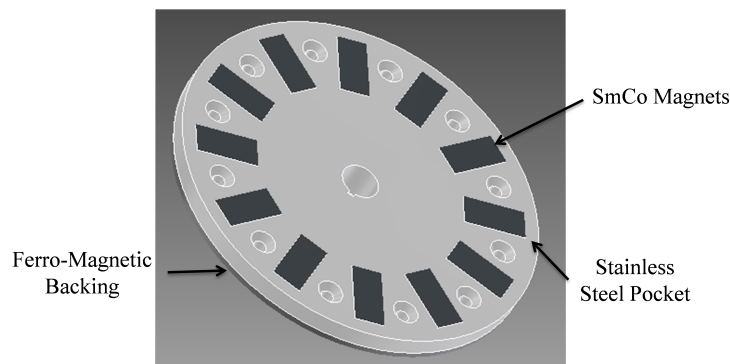
Figure A.2: 3D rendering of the disc with magnets.

stainless steel funnel was purchased and fitted into the loop via a 90° elbow. The funnel will hold approximately 80 mL, therefore, the salt will need to be added in two melting stages.

In the original design, the drain port was located directly underneath the fill port, however, this was changed to a point on the extreme edge of the loop. This change will allow for easier drainage of the loop by tipping it such that the drain port will be at the lowest point in the loop. This prevents potential pooling of the liquid within the loop. The drain port is a 0.25" tubing adaptor that has been welded into the main loop to create a "T". A Swagelok 0.25" needle valve has been positioned on the tubing adaptor and will be used to control drain flow.

Another addition to the loop is pressure ports just before and after the loop passes through the pump region. These ports are 0.125" tube adaptors that have been welded into the main loop. From these ports, Swagelok union fittings will be used to connect a Dwyer Series 2000-250PA differential pressure gauge. This feature will be used to measure the pressure head generated by the pump as well as provide information on the flow rates of the molten salt.

Due to the unique shape and design of the molten salt loop and electromagnet pump, it was not feasible to use a traditional induction type tube or box furnace. As a result, heating tape and temperature controller made by BriskHeat were employed. The heating tape that will be used is 1" wide by 48" long with a 13.1 W/in^2 heating capacity and is capable of

117

temperatures up to 600°C. At 627 total Watts generated by the tape, the salt within the loop should easily be melted and maintained at 500°C. The temperature controller is digital and can be programmed with set points and safety shutoff temperatures in an over-temperature scenario. To prevent burns and excessive heat loss from the molten salt loop and pump, 3" aluminosilicate insulation board was shaped around all heated features.

A motor was selected to meet acceleration and load requirements for the rotating discs and pump. Based on the pump design equations outlined in a previous report, the amount of power required to pump the salt was calculated to be approximately 1 W. This is rather small, as a result, the load required to accelerate the disc and to maintain angular momentum was the basis for motor selection. The disc have a moment of inertia (J) of approximately 330 kg/cm^2. With an acceleration of the disc form zero RPMs up to 5,000 RPMs in a reasonable amount of time equates to a torque of 1.1 N m. In addition, the power supply available in the lab is only 120 V at 20 A. Based on the torque and power criteria, a motor made by Teknic was selected. It is a M-3421 motor with a continuous torque rating of 2 N m. This motor comes complete with an encoder, power source, and operating software.

In addition to the motor, bearings to support the shaft and discs of the pump were needed. The radial load on the bearings iwas small due to the vertical configuration used. The axial load on the bearing was also small due to the relative mass of the components involved. The real challenge involved in selecting a bearing was the high temperatures involved. Special materials are required for bearings operating at 500°C, however, these materials wear quickly (graphite), or are ceramic and are prone to impact failure. Eventually, a bearing was selected from A.M.I. Bearing that is stainless steel and capable of handling temperatures up to 240°C. This selection allowed for a strong impact resistant bearing (safe), however, it may require additional cooling be provided to the shaft between the heating zone and the bearing. If needed, cooling will be provide by way of forced convection over the shaft via compressed argon. Provision for this cooling mechanism was built into the pump housing via stainless steel tubing.
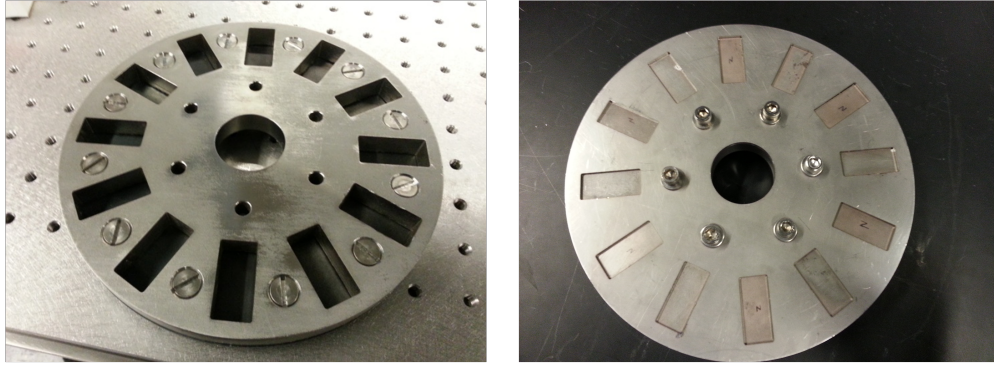
Figure A.3: (a) Photo of the support plate with attached backing. (b) Photo of the completed disc with magnets.

The disc used to house the rare earth magnets are composed of three layers. The first layer is a mild steel backing which allows for a surface for the magnets to adhere. The second layer is a 0.5" stainless steel (non-magnetic) plate with pockets cut to hold the magnets in place. The last layer is a stainless steel plate that is 0.06" thick. The disc are shown in Figure A.3 This plate also has notches, or openings that are smaller than the magnets themselves. This prevents the magnets from being thrown from the disc without covering and shielding them. The magnets shown in the disc were placed with alternating polarity.

Following the assembly of the discs, the disc were positioned on the shaft and installed in the pump housing as shown in Figure A.4. Here, the molten salt loop channel has been positioned such that it is equidistant from the disc surfaces so that no portion is in contact with the disc.

The finished EM pump is shown in Figure A.5. Initial testing of the loop with a molten salt showed a major weakness to the design. Due to the horizontal nature of the design the loop could not easily be filled or drained. As a result, the capability of the pump was not verified.
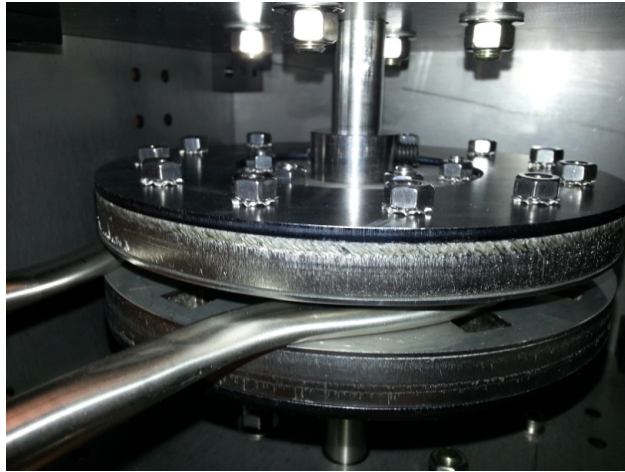
Figure A.4: Close up of the disc positioned around the molten salt loop channel.
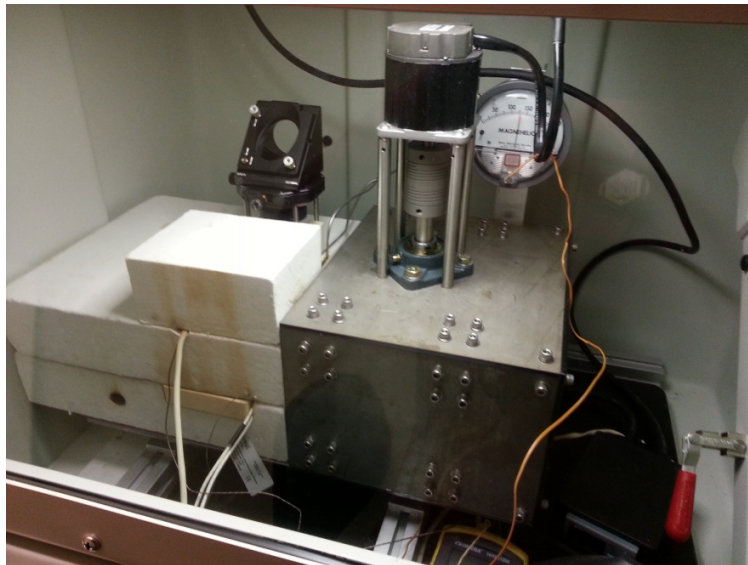

Figure A.5: Experimental apparatus complete with insulation.

A.4 Prototype 2

From the shakedown tests conducted to date using prototype 1, it was apparent that certain modifications were necessary to provide a better operating EM pump. Therefore, a second prototype (P2) molten salt loop was designed to aid in: (1) filling and draining the loop, (2) melting the salt, and (3) sealing the loop to force closed loop operation. The new loop was oriented vertically allowing gravity to aid in filling and draining the loop. Here, the fill port at the top of the loop can be sealed during operation using a Swagelok end cap. The drain valve is located at the lowest point in the loop, this allows for easy drainage of the loop. Another feature is the pressure measuring ports. The location of the ports is the same in P2 as in the previous design; however, now the ports have 1/4 tubing risers to prevent potential leakage close to the heating tape. The 1/4 inch risers are connected to 1/8 inch tubing which leads to the differential pressure gauge. This design also allows for a greater volume of gas to exist in the lines, while reducing the likeliness of capillary forces drawing salt far up the tubing. The risers as well as the 1/4 inch tubing connecting the drain valve have been welded into the main loop. The remaining fittings are Swagelok type compression fittings.

Several water tests were done to verify filling and draining procedures as well as to quantify the loop volume. For this, 100 ml of water was measured out and then a portion was used to fill the loop to capacity, the remaining water was measured to quantify the amount in the loop. For the first test 86 mL of water was used to fill the loop. Next, the drain capability was tested. The drain valve was opened and greater than 85 ml of the water was recovered. Several tests were run in this way and an average of 86 mL filled the loop. The density of the LiCl-KCl salt at 500°C is 1.62 g/cm^2; therefore, 139.3 grams of salt are needed to fill the loop.

With this design, additional heating was provided in the lower pump region. Here, the 3 inch insulation has been added to the apparatus along with a 6 ft by 1 inch heating tape made by Briskheat. This heating tape delivers up to 615 W of energy. The heating tape was

positioned around the loop such that approximately 4 ft of the loop was coiled around the EM pump disc to provide heating to the lower region of the loop, which had previously been a cold spot. The remaining 2 ft heat tape was wrapped around the upper portion of the molten salt loop. A test was done in the fume hood to test the heating capabilities of the new furnace design as well as to bake out the new insulation used in the design. During the test, the furnace was slowly ramped up to 500°C. Temperatures at the top of the loop, bottom of the loop, and at the shaft bearing interface were measured and recorded. Maximum observed temperatures were 535°C, 470°C, and 105°C for the upper portion, lower portion, and shaft bearing, respectively. The large temperature gradient between the top and bottom portion of the loops can be contributed to point of contact of the thermocouple. For the upper portion measurement, the thermocouple was in direct contact with the stainless steel loop. For the lower portion measurement, the thermocouple was positioned in air between the discs, close to the loop.

In the next phase, the apparatus was installed into the glove box as shown in Figure A.6. As previously mentioned, the apparatus was mounted vertically. The first test involving actual salt was conducted. Here, the salt beads were added prior to heating as before. However, only about half the beads could be added in this way due to geometric and physical constraints (this was expected). The furnace was then allowed to heat up slowly (approximately 4 hours) to prevent large thermal gradients within the furnace. During this time, the glovebox was continually being purged to remove any oxygen that may be released from the insulation during heating. Once the furnace was set to 500°C, the remainder of the salt was added via a funnel and stainless steel scoop. This procedure proved very effective and all 139.3 grams of salt were added. Once the salt was added, the system was left for 2 hours to come to a steady state temperature. Again, temperatures in/around the loop were 530°C, 480°C, and 140°C for the upper loop portion, lower loop section, and 2" above the furnace near the fill port, respectively.

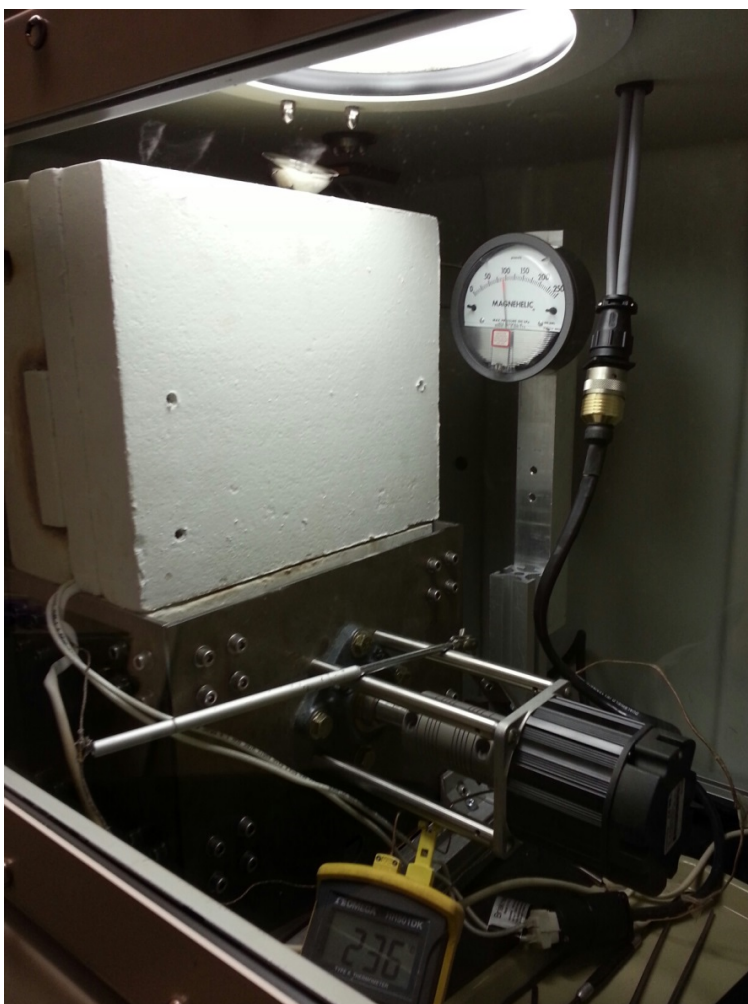With the furnace operating at 500°C and the loop filled completely with salt, it was

Figure A.6: Pump apparatus installed in the inert atmosphere glove box.

possible to test the EM pump capabilities. With the disc RPM set to zero, the differential pressure gauge was zeroed. The RPM was then set at 500 RPM and no change was observed in the pressure. The same result was observed for the 1,000 RPM, 1,500 RPM, 2,000 RPM, 2,500 RPM, and 3,000 RPM. Several potential reasons exist for this observed result. First, the magnets were de-magnetized due to temperature. This is highly unlikely due to their extremely high curie temperature at 500°C. Upon system cooling the magnetic strength of the magnets was verified using a Guassmeter, the magnets maintained their full original strength. Second, a failure in the measuring technique prevented an accurate reading of the flow within the loop. After system cool down a small amount of salt residue was discovered around the 1/8 inch Swagelok fitting on both pressure risers. This means that gas and salt escaped through at least these fittings, this could potentially skew results. This alone should not account for a zero response at the pressure gauge; however, being that salt was present this high up the riser suggest that salt rose as a result of compression of the gases in the lines and potential leaking of the risers. If allowed to rise sufficiently high to leave the heated area, it could reach the melting temperature and plug the tubing. If this occurred, regardless of the pressure differential and flow in the loop nothing would register at the gauge. Lastly, the magnetic flux or electrical conductivity of the salt is not sufficient to provide a strong enough Lorentz force for pumping to occur.

A.4.1 Molten Salt Flow —Problems and Solutions

It was thought that the molten salt shakedown experiment failed for what appeared to be capillary action and/or freezing in the pressure measurement risers coming from the main salt loop. For the next shakedown test, the 0.125 inch lines were replaced with larger 0.25 inch lines to mitigate this issue.

The first experiment conducted using the new EM pump riser design was done using pure LiCl-KCl eutectic salt. As before, the salt beads were loaded into the top portion of the furnace at temperature until the loop was full—requiring approximately 139 g of salt at

500°C. With the loop fully loaded, and the furnace up to temperature, the EM pump capabilities were tested. At 200 RPM, there was no observed change in the pressure differential, indicating no flow or pressure gradient of any kind. The same result was observed for speeds all up to 3,000 RPM. Following the experiment, no observations were made indicating failure due to the risers.

Several possible theories exist for pump failure: (1) the pressure measuring system is not functioning correctly, (2) the electrical conductivity of the salt is too low, or (3) the Lorentz force acting on the positive ions (Li^+ and K^+) is being canceled by the forces acting on the negative ions (Cl^-). The last theory was the easiest to test. For the next experiment, a LiCl-KCl-CeCl$_3$ (10wt% CeCl$_3$) salt was used. The Ce^{+3} ion has a greater charge and would therefore, be more strongly influenced by the Lorenz force than the Cl$^-$ ion. The experiment was prepared and conducted with similar results observed as before; that is, there was no pressure gradient generated in the molten ternary salt mixture.

A.5   Molten Tin Test

To test the other two EM pump failure theories, an additional material must be used to test the pump. Molten metals have been shown to have sufficient electrical conductivities to be pumped using design configurations similar to the one used in this study[46]. Here the objective was to test the EM pump using molten tin to verify the EM pump and pressure measuring system. Tin was selected due to its low melting point (231.9 °C), low toxicity, and high electrical conductivity.

To ensure complete melting of the tin, a temperature of 400°C was selected as the operating temperature for these experiments. At 400°C, the density (ρ), viscosity (ν), and electrical conductivity (σ) are 6.834×10^3 kg/m^3, 1.3×10^{-3} kg m/s, and 1.945×10^4 ohm^{-1} cm^{-1}, respectively. (Note: σ for molten LiCl-KCl at 500°C is 1.854 ohm^{-1} cm^{-1}). Based on previous experiments, 86 mL of material is needed to fill the loop, thus 587.7 g of tin were
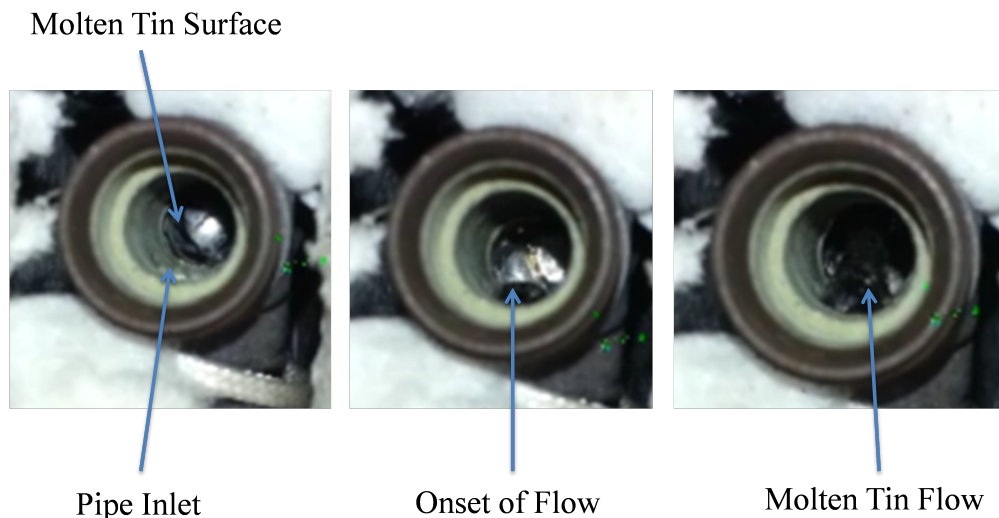
Figure A.7: Photos extracted from a video taken at the onset of molten metal flow in the electromagnetic pump.

required.

A.5.1 Experiment 1

The EM pump was positioned in the fume hood in the Radiochemistry Laboratory in the VCU West Hall. Here, the loop was loaded with tin as done previously. The temperature was ramped to 400°C, at this point; the surface of the molten tin could be seen near the top of the fill port. However, the liquid level was low and the system had not yet closed, in other words, the upper portion of the loop was still dry. When the pump motor was engaged slightly, the liquid level on the high pressure side of the loop was observed to increase. As the motor speeds (in RPM) were increased, the liquid level continued to increase until it reached the top of the loop and spilled over into the low pressure portion of the loop. Photos extracted from a video of the observed flow are shown in Figure A.7. At this point, an additional 6 g of tin were added to ensure the loop was properly filled. By observation, it is clear that flow is occurring within the loop, such flow was never observed for the molten salt system.

In addition to the observed flow, pressure readings were measured as a function of the

motor RPM. Here, motor RPM was rapidly taken from zero to the end RPM in a single step. A pressure data collected from the first experimental run is shown in Figure A.8. It can be seen that as the motor RPM increased, the measured pressure differential also increased. From the pressure differential, the average velocity (v), flow rate (Q), and Reynolds (Re) number can be calculated using the following equations:

$$v = \frac{\Delta p D^2}{32 \mu l} \tag{A.7}$$

$$Q = \frac{\pi D^4 \Delta p}{128 \mu l} \tag{A.8}$$

$$Re = \frac{\rho v D}{\mu} \tag{A.9}$$

where Δp, D, and l are the differential pressure, tube diameter, and tube length, respectively. Eqns. A.7 and A.8 are derived under the assumption that the flow is fully laminar. Calculated values for the velocity, flow rate and Reynolds numbers are shown in Table A.2. Interestingly, values of the Re number indicate that much of the flow is not in the laminar flow regime ($Re \leq 2100$), but in the transitional regime ($2100 < Re < 4000$) and turbulent regime ($Re \geq 4000$). As a result, Eqns. A.7 and A.8 can only be used as an approximation of the flow characteristics of the metal within the loop.

When attempting to operate at the motor at 1035 RPM during this first experiment, a large noise was observed and the pressure spiked up to 150 Pa and then slowly and continuously climbed. At zero RPM the pressure did not return to zero but remained at approximately 65 Pa. The fill port cap was removed and it was observed that the liquid level in the loop had dropped approximately 2 cm, suggesting that molten metal had been forced up the pressure risers. The pressure still responded, albeit, slower, so the assumption was made that the risers were not blocked.

To account for the drop in material, 41.5 g of tin were added to the loop to ensure the loop was completely filled. Several pumping runs were conducted but the data was not consistent
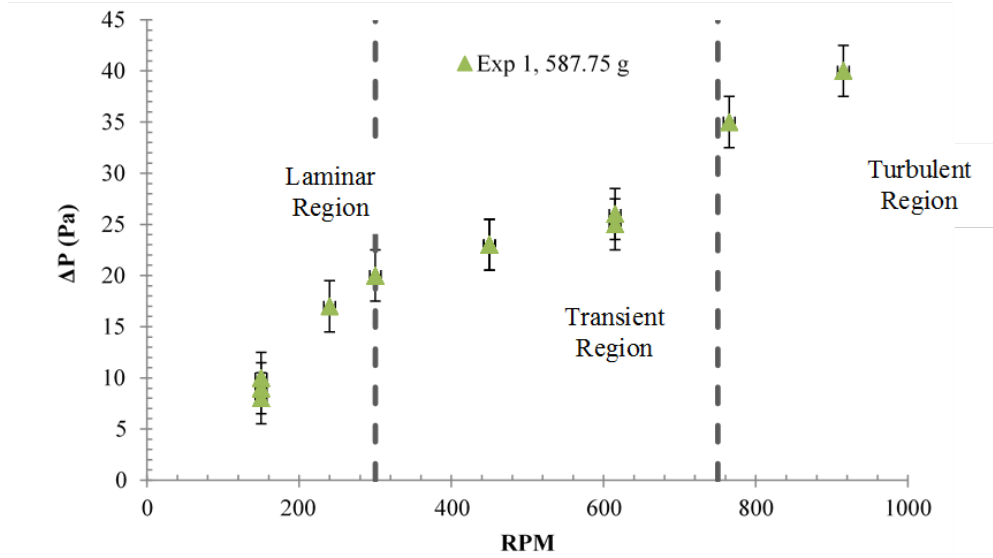
Figure A.8: Pressure curve for experiment 1. For motor speeds up to approximately 300 RPM the flow in the loop is laminar. Between 300 and 750 RPM the flow is in the transitional regime. For motor speeds the above 750 RPM the flow is within the turbulent regime.

Table A.2: Calculated values of the velocity, flow rate, and Reynolds number for Exp. 1.

RPM	ΔP (Pa)	v (cm/s)	Q (cm^3/s)	Re
150	8	1.67	1.56	902
150	9	1.88	1.76	1015
150	10	2.08	1.95	1127
240	17	3.54	3.32	1916
300	20	4.17	3.90	2255
450	23	4.79	4.49	2593
450	23	4.79	4.49	2593
450	23	4.79	4.49	2593
615	25	5.21	4.88	2818
615	26	5.42	5.08	2931
765	35	7.30	6.83	3945
915	40	8.34	7.81	4509

and the response time was quite slow. At this point, the pressure gauge was removed from the risers and solid tin was observed in the fitting leading into the pressure gauge as well as within the gauge itself. During the first experiment, when attempting to reach 1035 RPM material must have been thrown up into the risers due to a large impulse in the fluid created by the rapid acceleration of the motor.

The observed material was easily removed from the fitting and gauge; however, the riser tube itself was blocked with an unknown amount of material. Since material had been added to the main loop, there would not be room for the metal volume in the risers to drain properly; therefore, 105.5 g of tin were drained from the main loop via the drain port. The risers were drained by tipping the furnace (now at room temp) on its side and heating the risers using a heating tape on hand. The heat tape was operated at 400°C for 20 minutes. Once the riser had cooled, a thermocouple was inserted into the riser down into the loop region, verifying that the blockage had been removed. At this point, approximately 525 g of tin was in the loop.

A.5.2   Experiment 2

For this experiment, no new metal was added into the loop. The goal was to measure the pressure gradient induced by the pump under no flow conditions. Motor control for this experiment was done using Quickset software via a %offset function. To prevent an impulse as described previously, motor RPM was ramped in 1 %offset intervals (30 RPM). Data collected in this experiment is shown in Figure A.9. Here, as the RPM increased, the liquid level in the high pressure side increased with pressure. However, for the data greater than 210 RPM, the liquid level had risen far enough that it was spilling over into the low pressure side of the loop. When speed were greater than 270 RPM, air was being introduced into the loop creating a sucking sound due to the low liquid level. As a result, no data was collected at speeds greater than 270 due to inconsistencies introduced by air introduction to the pumping region causing a two-phase flow.
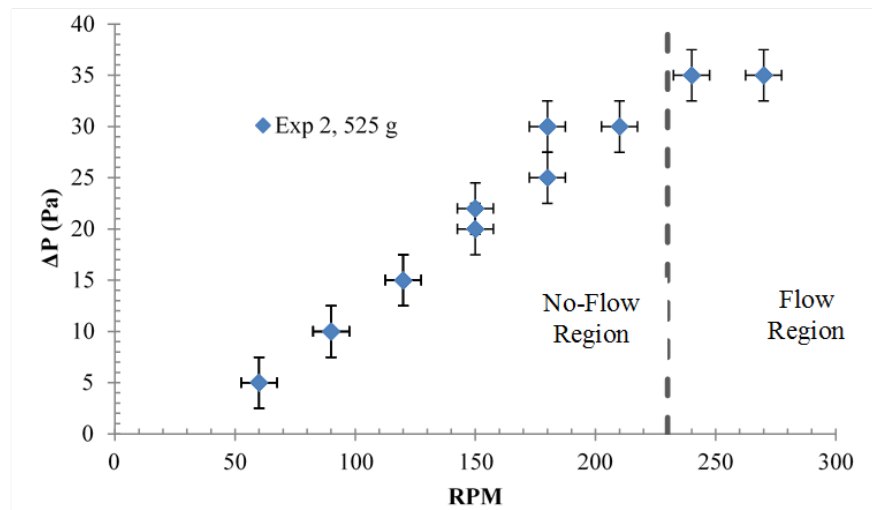
Figure A.9: Pressure curve for experiment 2. In the initial linear portion no flow occurred; however, liquid metal levels were high enough in the last two points for material to spill over into the low pressure side.

No additional molten metal experiments have been conducted to date; however, these experiments clearly demonstrate that the EM pump does work and that the pressure measuring system is working. As a result, it can be concluded that a molten salt cannot be pumped via this system due to low electrical conductivity. As a result, additional methods to performs LIBS on a non-static molten salt must be explored.

Appendix B

LIBS in Solid LiCl-KCl Salt

B.1 Research Objective

The purpose of study is to determine the effectiveness of LIBS as a means of measuring the concentration of the rare earth element Gadolinium (Gd) in a mixture of $CeCl_3$ and eutectic LiCl-KCl in solids at different concentration ratios. This is to simulate the nuclear material found in preprocessing, and is accomplished by doing a LIBS analysis of solid salt samples sealed in a glass vial with an argon atmosphere. All 36 samples shown in Table B.1 have been analyzed.

B.2 Experimental Setup

Salt samples were prepared in an inert atmosphere (argon gas) glove box. The base salt was formed by mixing LiCl and KCl (Alfa Aesar) to form a eutectic salt (44 wt% LiCl and 56 wt% KCl). Appropriate amounts of $GdCl_3$ and $CeCl_3$ salts were then added to the base salt and melting in an alumina crucible at 500°C for at least 4 hours. Once the salt was completely melted, a 4 mm inside diameter Pyrex glass tube was then used to extract the salt sample via a syringe. The salt drawn into the Pyrex tube solidified and was removed as thin cylindrical salt rods with a diameter of approximately 4 mm. The cylindrical salt

Table B.1: Composition of the Ce and Gd samples to be analyzed.

Standard	wt% GdCl$_3$	wt% CeCl$_3$	Standard	wt% GdCl$_3$	wt% CeCl$_3$
1	0.5	0.5	19	3.0	0.5
2	0.5	1.0	20	3.0	1.0
3	0.5	2.0	21	3.0	2.0
4	0.5	3.0	22	3.0	3.0
5	0.5	4.0	23	3.0	4.0
6	0.5	5.0	24	3.0	5.0
7	1.0	0.5	25	4.0	0.5
8	1.0	1.0	26	4.0	1.0
9	1.0	2.0	27	4.0	2.0
10	1.0	3.0	28	4.0	3.0
11	1.0	4.0	29	4.0	4.0
12	1.0	5.0	30	5.0	5.0
13	2.0	0.5	31	5.0	0.5
14	2.0	1.0	32	5.0	1.0
15	2.0	2.0	33	5.0	2.0
16	2.0	3.0	34	5.0	3.0
17	2.0	4.0	35	5.0	4.0
18	2.0	5.0	36	5.0	5.0

samples were positioned in the center of a 1" diameter glass vial as shown in Figure B.1 The sample was secured in the vial using a vacuum suction cup attached to the base of the glass vial; there is a small slot to fit a cylindrical piece of salt. The vial containing the salt sample was backfilled with argon gas and sealed.

The experimental setup is shown in Figure B.2. The vial containing the sample was placed horizontally on a stable surface where is moved in a horizontal motion so that each
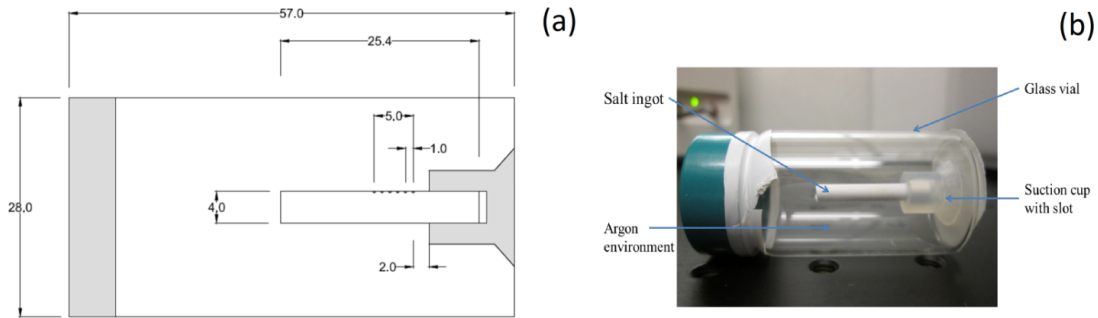

Figure B.1: (a) Schematic of glass vial containing salt sample, dimensions in mm. (b) Close up picture of glass vial containing the sample.
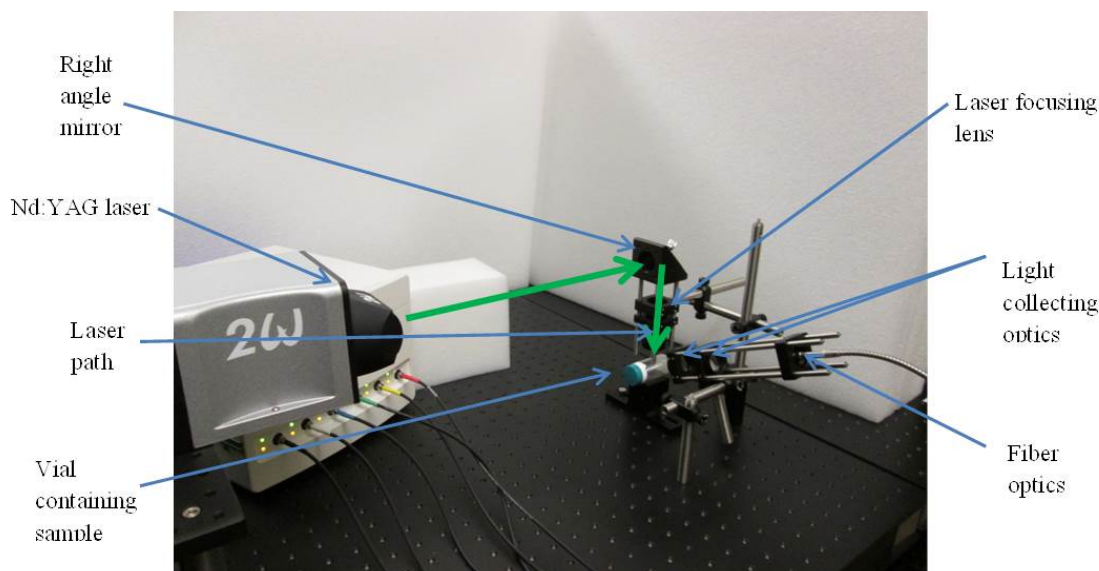
Figure B.2: Picture of laser line and focusing optics.

of the six 100 shot replicates were performed on spots that were approximately 2 mm apart. Sampling vials were reused and the vial orientation was consistent to reduce changes in focal length from sample to sample. Light from the laser was directed downwards via a mirror and through a 50 mm focal lens and the glass vial wall onto the sample. Light from the plasma was then collected via 35 mm focal length lens and then focused onto the fiber optic cable via a 100 mm focal length lens.

The laser used in this experiment was the Q-Smart 450 from Quantel USA. This laser was coupled with the Aurora LIBS Spectrometer from Applied Spectra Inc. to carry out the LIBS experiment. For all the samples tested a constant repletion rate of 1 Hz was used after varying parameters and optimizing the system, a 30 mJ laser pulse was used for all of the LIBS experiments. For the spectrometer, a gate delay of 6 μs and a gate width of 1.05 s were used when collecting spectra. A total of six replicates were collected for each sample. Spectra from 100 laser shots were collected and averaged to create each replicate spectrum. Peaks for analysis were determined using the NIST database for atomic spectral lines in the peak identification section of the spectrometer software, the line of that were used were Gd II 335.047 nm, Gd II 336.223 nm and Gd II 342.247 nm which had relative intensities of
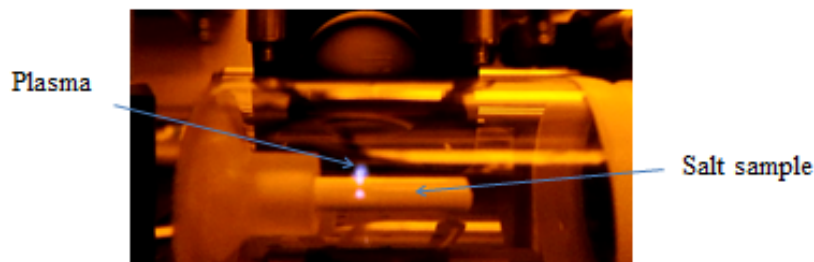
Figure B.3: Picture of plasma formed on the surface of the salt.

5400, 5400 and 6900, respectively. Figure B.3 shows the picture of plasma formed on the surface of the salt ingot.

B.3 Results and Discussion

One of the major problems faced was the dust build up on the inside surface of the vial, so to reduce this lower energy pulses were used which decreased signal intensity. Figures B.4 and B.5 shows the averaged spectrum obtain after 100 shots at approximately 30 mJ and 80 mJ pulse energies. It can be seen that the vial containing the sample that was shot with the 80 mJ pulse is slightly dustier than the other vial, this collection of dust greatly decreases the signal obtained as it decrease the laser energy being focused on the salt while also decreasing the plasma coming from the vial. Therefore, performing the analysis with lower pulse energies seemed to give the best results. There is still some decrease in signal intensity as more repetitions are performed on a sample. Figure B.6 highlights the change in intensity of the signal from the first to the sixth repletion caused by the dust buildup on the vial surface.

Once all the spectra for the data set had been collected, each data run was then normalized relative to the area of the Li I 497.166 nm peak by dividing the areas of each spectra with a value their respective Li I 497.166 nm peak area. This was performed using a written in house MATLAB program. The peak area of each replicate at all three peaks were calculated
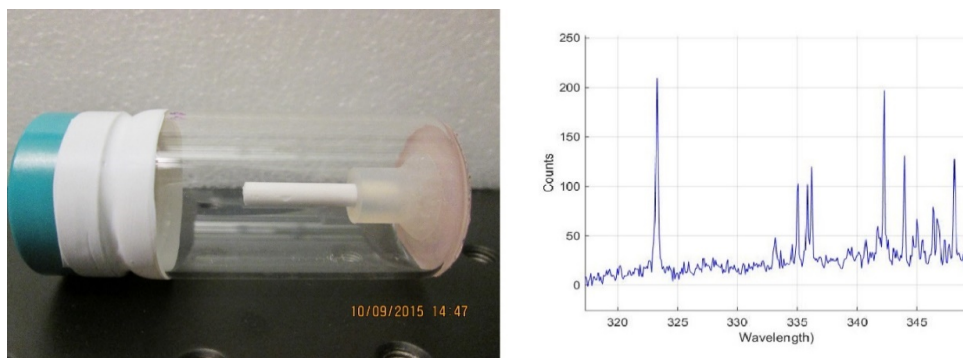
Figure B.4: Picture of glass vial after 100 shots at 30 mJ (left) and averaged spectrum of that 100 shots in the range of 320-345 nm (right).
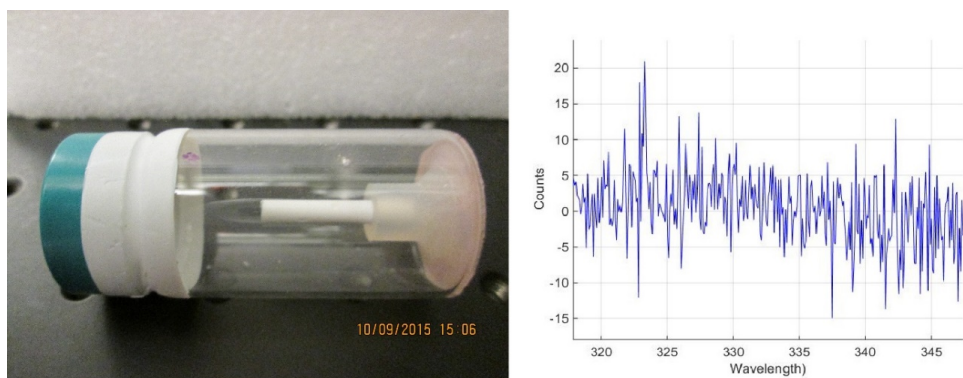

Figure B.5: Picture of glass vial after 100 shots at 80 mJ (left) and averaged spectrum of that 100 shots in the range of 320-345 nm (right).
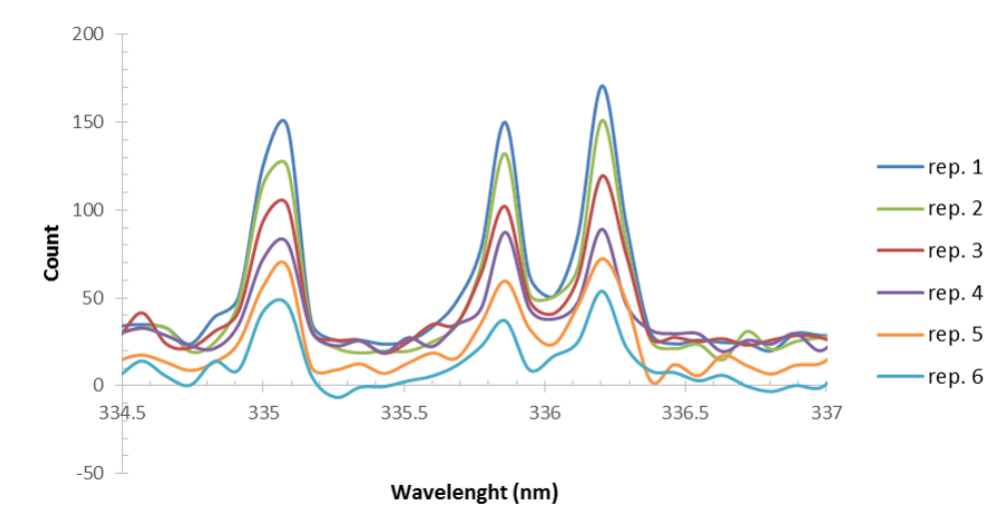

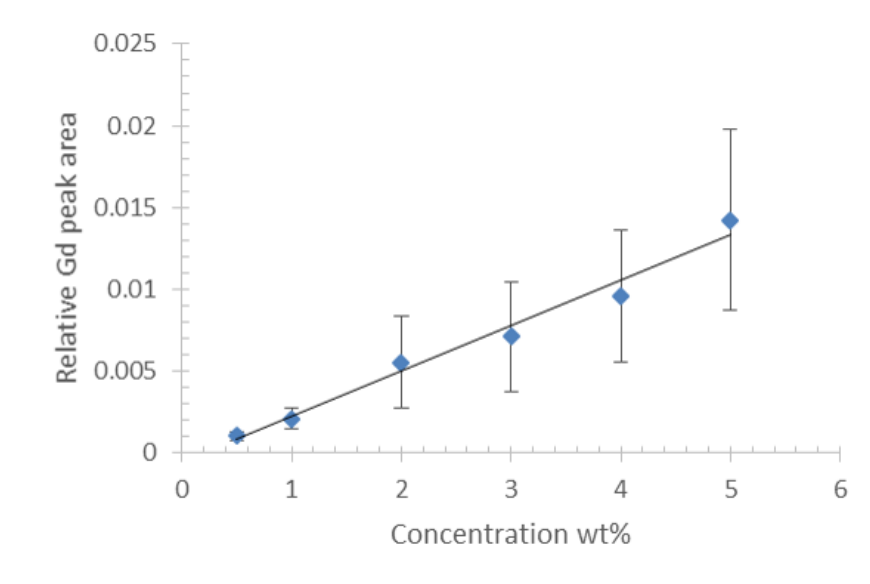Figure B.6: Averaged spectra of each repetition taken for the 5 wt% $CeCl_3$ - 4 wt% $GdCl_3$ sample.

Figure B.7: Gd II 335.047 nm relative peak area as a function of the GdCl$_3$ concentration. The linear fit has slope m = 0.0028, intercept b = -0.0006 and R^2 = 0.9790.

and averaged to attain one data point for each of the peaks, these peak areas were also used to calculate the standard deviation of each averaged peak area value. The calibration curves for Gd II 335.047 nm, Gd II 336.223 nm, and Gd II 342.247 nm for the 0.5 wt% CeCl$_3$ data set are shown in Figures B.7, B.8 and B.9, respectively, as illustrations. Similar trends can be observed for other concentrations of CeCl$_3$. While Table B.10 list the rest of the results from the calibration curves and the limits of detection (LOD).

As seen in Figures B.7 – B.9, the error bars on most of the data points are quite large, which is due to the relatively large change in signal intensity as seen in Figure B.6; this is one of main reasons why normalization was performed.

After comparing all the results from Table B.10, the 335.047 nm line seems to have the best LODs and is probably the best line out of the 3 to use for LIBS analysis; it had the lowest LOD for 4 out of the 6 data set all of which were lower the 0.5 wt%. This is probably due to this peak not having any close overlying peaks along with the large standard deviation cause by the dust buildup on the glass surface. For the 3 wt% Ce data set where the 335.047 nm line had the largest LOD, all three curves had unusually large LODs, which mean there
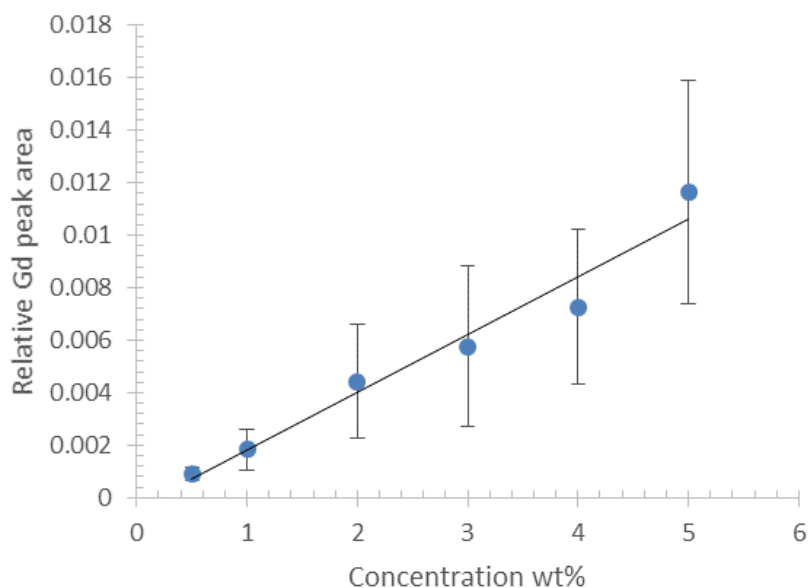
136

Figure B.8: Gd II 336.223 nm relative peak area as a function of the GdCl$_3$ concentration. The linear fit has slope m = 0.0022, intercept b = -0.0004 and R^2 = 0.9631.
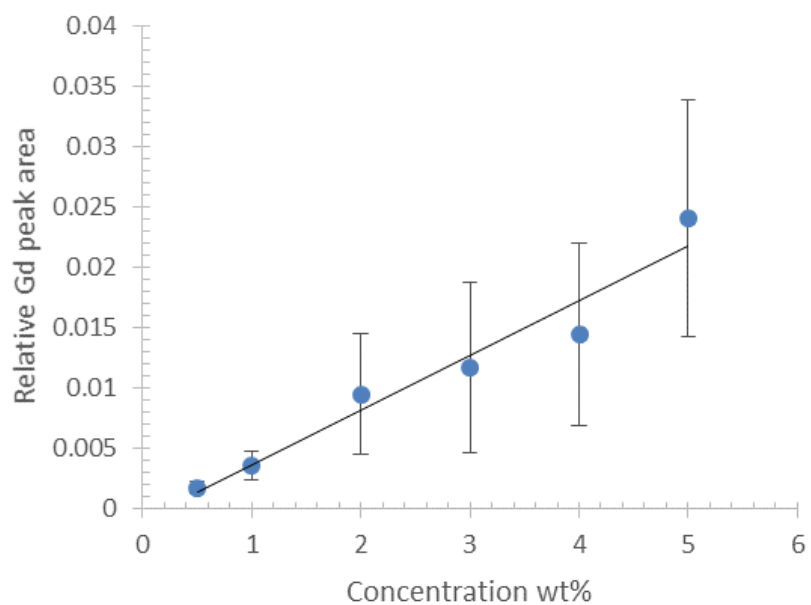

Figure B.9: Gd II 342.247 nm relative peak area as a function of the GdCl$_3$ concentration. The linear fit has slope m = 0.0045, intercept b = - 0.0008 and R2 = 0.9505.

Data Set CeCl$_3$ (wt%)	Gd Lines (nm)	m	b	R^2	LOD (wt%)
0.5	335.047	0.0028	-0.0006	0.9790	0.2963
	336.223	0.0022	-0.0004	0.9631	0.3599
	342.247	0.0045	-0.0008	0.9505	0.3341
1.0	335.047	0.0030	-0.0001	0.9661	0.3786
	336.223	0.0023	-0.0001	0.9664	0.9605
	342.247	0.0051	-0.0004	0.9536	0.7331
2.0	335.047	0.0023	-0.0006	0.9784	0.3109
	336.223	0.0018	-0.0003	0.9906	0.3610
	342.247	0.0040	-0.0006	0.9837	0.4568
3.0	335.047	0.0020	0.0005	0.9930	1.4100
	336.223	0.0017	0.0002	0.9870	0.7425
	342.247	0.0037	0.0006	0.9736	1.1102
4.0	335.047	0.0022	0.0005	0.9725	0.4629
	336.223	0.0018	0.0005	0.9640	0.4931
	342.247	0.0039	0.0016	0.9524	0.8071
5.0	335.047	0.0022	0.0002	0.9799	0.6654
	336.223	0.0018	0.0002	0.9874	0.3507
	342.247	0.0038	0.0008	0.9932	0.7990

Figure B.10: List of linear fit coefficients and limit of detection for the different calibration curves.

was some irregularity which the entire data. This could be improved with more accurate concentration values from an ICP-MS analysis of the samples.

B.4   Summary

For the solid samples, calibration curves for GdCl$_3$ have been generated at 6 different CeCl$_3$ compositions. Results from Table 6.2 indicate that the 335.047 nm line seems to have the best LODs and is probably the best line out of the 3 to use for LIBS analysis. For the 3 wt% Ce data set where the 335.047 nm line had the largest LOD, all three curves had unusually large LODs, which mean there was some irregularity which the entire data. This could be improved with more accurate concentration values from an ICP-MS analysis of the samples.

Accomplishments

Invention Disclosure

Filing on July 28, 2015 to VCU Innovation Gateway:
> Title of Invention: Impurity Detection in High Temperature Liquid Aerosol via Laser-Induced Breakdown Spectroscopy

Publication (the * indicates student co-authors)

1. *Williams AN, <u>Phongikaroon S</u>, "Laser-Induced Breakdown Spectroscopy (LIBS) in a Novel Molten Salt Aerosol System." Accepted to *Applied Spectroscopy* March 1, 2016. DOI: 10.1177/0003702816648965.
2. *Williams AN, and <u>Phongikaroon S</u>, "Elemental Detection of Cerium and Gadolinium in Aqueous Aerosol via Laser-Induced Breakdown Spectroscopy." Accepted to *Applied Spectroscopy* Feb. 3, 2016. DOI: 10.1177/0003702816648327.

Presentation (_____ indicates the presenter)

1. "Assessment of a Laser-Induced Breakdown Spectroscopy (LIBS) Technique in Molten Salt Aerosol," <u>Williams AN</u> and Phongikaroon S. *International Pyroprocessing Research Conference*, JeJu Island, Korea, September 21-23, 2016.
2. "Laser-Induced Breakdown Spectroscopy (LIBS) Measurement of Uranium in Electrorefiner Molten Salt," <u>Williams AN</u> and Phongikaroon S. *International Pyroprocessing Research Conference*, JeJu Island, Korea, September 21-23, 2016.
3. "Laser-Induced Breakdown Spectroscopy (LIBS) Determination of Cerium and Uranium in Molten Salt Aerosol," <u>Williams AN</u> and Phongikaroon S. *Institute of Nuclear Materials Management – Annual Meeting*, Atlanta, GA, July, 2016.
4. "Optimization of Laser-Induced Breakdown Spectroscopy Parameters in a Novel Molten Salt Aerosol System," <u>Williams AN</u> and Phongikaroon S. *24th International Conference on Nuclear Engineering (ASME)*, Charlotte, NC, June, 2016.
5. "LIBS Measurement of Rare-Earth Chlorides ($CeCl_3$ and $GdCl_3$) in LiCl-KCl Solid and Molten Aerosol," <u>Williams AN</u>, Bryce K, Motny R, Phongikaroon S. 2016 MPACT Working Group Meeting, Los Alamos National Laboratory, March 2016.
6. "Laser-Induced Breakdown Spectroscopy (LIBS) Detection of Gadolinium in Solid LiCl-KCl Salt Samples," Bryce K, <u>Williams AN</u>, Phongikaroon S. *American Nuclear Society—Winter Meeting*, Washington, D.C., November, 2015.
7. "Elemental Detection of Cerium and Gadolinium in Aqueous Aerosols via Laser-Induced Breakdown Spectroscopy," <u>Williams AN</u> and Phongikaroon S. *GLOBAL 2015*, Paris, France, September 2015.
8. "Measurement of Cerium in Molten Salt Aerosol via Laser-Induced Breakdown Spectroscopy," <u>Williams AN</u> and Phongikaroon S. *GLOBAL 2015*, Paris, France, September 2015.
9. "LIBS Measurement of Cerium Chloride in a Molten LiCl-KCl Salt—Initial Task Study in Aqueous $CeCl_3$-LiCl-KCl," <u>Williams AN</u>, Yoon D, Phongikaroon S. 2014 MPACT Working Group Meeting, San Diego, CA, March 2014.
10. "Separation of $SrCl_2$ and CsCl from Ternary $SrCl_2$-LiCl-KCl and Quaternary $SrCl_2$-CsCl-LiCl-KCl Molten Salts via Melt Crystallization," <u>Williams AN</u>, Pack M, Phongikaroon S. *American Nuclear Society—Winter Meeting*, Anaheim, CA, November 2013.
11. "Chemical Detection in Flowing Molten LiCl-KCl salt via Laser-Induced Breakdown Spectroscopy," <u>Williams AN</u>, Phongikaroon S. *American Nuclear Society—Winter Meeting*, Washington, D.C., November 2013.